MULTIFUNCTIONAL FIBER DEVICES ENABLED BY METASURFACE AND GRAPHENE

WANG YUE

PhD

THE HONG KONG POLYTECHNIC UNIVERSITY

2025

The Hong Kong Polytechnic University

Department of Electrical and Electronic Engineering

Multifunctional Fiber Devices Enabled by Metasurface and Graphene

Wang Yue

A thesis submitted in partial fulfilment of the requirements for the degree of Doctor of Philosophy

May 2025

CERTIFICATE OF ORIGINALITY

I hereby declare that this thesis is my own work and that, to the best of my knowledge and belief, it reproduces no material previously published or written, nor material that has been accepted for the award of any other degree or diploma, except where due acknowledgement has been made in the text.

_____ (Signed)

Wang Yue (Name of student)

Abstract

Multifunctional Fiber Devices Enabled by Metasurface and Graphene
by Yue Wang
For the degree of Doctor of Philosophy
At the Hong Kong Polytechnic University in May 2025
Supervised by Professor Changyuan Yu

Optical fibers, serving as the backbone of modern telecommunication and sensing systems, have long been constrained by their intrinsic functional limitations. Conventional optical fibers relying on total internal reflection mechanisms fundamentally lack dynamic light-field manipulation capabilities at subwavelength scales, restricting their applications to passive light-guiding roles. This functional limitation seriously contrasts with the growing demand for integrated optical systems in emerging fields such as smart optical networks, miniaturized biosensors, and quantum photonic circuits. Emerging nanophotonic platforms, particularly metasurface and two-dimensional (2D) materials, offer transformative solutions to these challenges. Metasurface, comprising subwavelength nanostructured arrays, enable unprecedented control over electromagnetic wavefronts through localized phase engineering. Meanwhile, 2D materials like graphene exhibit exceptional optoelectronic tunability from strong light-matter interactions and gate-voltage-dependent optical responses. By synergistically integrating these nanotechnologies with optical fibers, we propose a new meta-fiber platform toward multifunctional fiber devices for compact and active communication and sensing systems.

This dissertation establishes the feasibility of the meta-fiber platform through the development of three functional fiber devices: two fiber-tip-integrated metasurface

devices and one tunable D-shaped fiber polarizer exploiting graphene-light interactions. Chapter 3 introduces a complete fabrication framework for metasurface integration on optical fiber tips, demonstrating a flat-band plasmonic quasi-BIC metasurface that couples efficiently with fiber propagation modes. By precisely controlling symmetry-breaking parameters, we achieve a high-Q and ultra-sensitive fiber sensor with real-time refractive index resolution of 1.7×10^{-4} RIU. Chapter 4 implements the established framework to fabricate a fiber-integrated metalens exhibiting exceptional circular dichroism, experimentally enabling polarization-modulated all-optical switching in 2 Gbps PAM4 systems with >20 dB extinction ratio. Chapter 5 is a proof-of-concept electro-optically tunable D-shaped fiber polarization filter exploiting hybrid graphene-gold plasmonic interactions. The phase-matching condition between the fiber's fundamental mode and gold grating-induced surface plasmon resonance (SPR) can be tuned via graphene chemical potential modulation, achieving continuous spectral tuning across C-band (1530-1565 nm) and O-band (1260-1360 nm) with ~30 dB extinction. Collectively, these advances bridge nanophotonic functionalities with fiber-optic architectures, presenting their scalable applications in optical sensing, high-speed communications, and tunable optical systems.

Publications

There are publications during my Ph.D. period and most of which contribute to this thesis.

Journal papers

[1]. **Y. Wang**, Z. Wang, J. Qu, Z. Cheng, D. Huang and C. Y. Yu, “Tunable all-fiber polarization filter based on graphene-assisted metal gratings for the O-and C-bands,” ***JOSA B,*** vol. 40, pp. 2868-2874 (2023).

[2]. **Y. Wang**, Z. Wang, Y. D. Deng, L. Wang, P. Xu, J. X. Cui, C. Y. Leong, C-W. Qiu, C.Y. Yu, “Plasmonic Flat-Band Quasi-Bound States in the Continuum for Ultrasensitive Fiber-Tip Sensing,” (***Laser & Photonics Reviews*** invited paper under revision).

[3]. L. Wang, **Y. Wang,** Z. Lin, Z. Yu, Y. Li, C. Lu, C. Y. Yu and M. Tang. Endogenous integration of communication and interference fading-free sensing using telecom pilots via joint polarization-fraction domain multiplexing. ***Optics Express*** (co-first author, accepted)

[4]. Z. Wang, **Y. Wang**, Z. Cheng, J. Q Qu, M. J Cui, D. M Huang, and C. Y. Yu, "Tunable flat-band plasmonic quasi-bound states in the continuum based on graphene-assisted metasurfaces," ***Applied Physics Letters***, vol. 123, no. 12, pp. 121703 (2023).

[5]. L. Wang, **Y. Wang**, J. Wang, H. He, L. Lu, C.Y. Yu, and Ming Tang, "Ultra-fast SOP rotation tracking and its enabled feedforward adaptive equalization based on superimposed chirp pilot," ***Optics Express***, vol. 33, pp. 7110-7125 (2025)

[6]. X. T Lou, **Y. Wang**, N Xu, and Y. K Dong, “Laser spectroscopic gas sensing with 7-decade dynamic range by simultaneous measurement of absorption and dispersion,” ***Photonics Research,*** vol. 11, no. 10, pp. 1687-1693 (2023).

[7]. J. Qu, Z. Wang, Z. Cheng, **Y. Wang**, and C. Yu, “Full-Stokes parameters detection enabled by a non-interleaved fiber-compatible metasurface,” ***Optics Express***, vol. 31, no. 13, pp. 20836-20849 (2023).

Conference papers

[1]. **Y. Wang**, J. Qu, L. Wang, C-W. Qiu, C.Y. Yu, "Photonic Crystal Fiber Metalens with Planar Chiral Units for Arbitrary Polarization Focusing", ***2025 Optical Fiber Communications Conference and Exhibition (OFC)***, Paper W2A. 10, pp. 1 – 3, San Francisco, CA, USA, March 30 - April 3, 2025.

[2]. **Y. Wang**, Z. Wang, Y. Deng, L. Wang, and C. Y. Yu, "Meta-fiber sensor based on structural-asymmetry-induced quasi bound states in the continuum," ***2024 Conference on Lasers and Electro-Optics Pacific Rim (CLEO-PR)***, pp. 1-2, Incheon, Korea, Republic of, August 04 - 09, 2024.

[3]. **Y. Wang**, L. Wang, Z. H, Lin, C. Lu, M. Tang, C. Y. Yu, "Endogenous ISAC Enabled Interference Fading Free Sensing via Telecom Training Sequence," ***30th OptoElectronics and Communications Conference/International Conference on Photonics in Switching and Computing 2025 (OECC/IPC 2025)***, Sapporo, Japan, June 29 - July 3, 2025.

[4]. J. Qu, **Y. Wang,** Z. Wang, Z. Cheng, and C. Yu, "Fiber-tip tri-foci metalens," ***2023 Photonics Global Conference (PGC)***, pp. 61-63, Stockholm, Sweden, August 21-23, 2023.

Acknowledgements

I wish to extend my sincere gratitude to my doctoral supervisor, Prof. Changyuan Yu, whose unwavering support and guidance have been instrumental in shaping this research journey at Hong Kong Polytechnic University. Professor YU's approachable demeanor and exceptional patience created an encouraging environment for academic exploration, particularly evident from my very first days in the research group. I will always remember how he generously treated me to a welcoming lunch and personally guided me through the laboratory tour, which laid a solid foundation for my subsequent research endeavors. His insightful suggestions during our regular academic discussions and meticulous revisions of my work have significantly elevated the quality of this dissertation. I am also profoundly indebted to Professor Yongkang DONG, supervisor of my master's degree, whose mentorship continues to inspire my academic pursuits. His patient guidance in experimental design and paper writing during my formative years as a researcher established essential methodologies that I continue to apply in my current work.

A special “thank-you” goes to Prof. Chengwei QIU at the National University of Singapore (NUS). I started my transition journey as a PhD student in Electrical and Computer Engineering at NUS. His profound expertise in nanophotonics provided me with an exemplary model of frontier scientific exploration. In addition, I extend sincere gratitude to the research team at NUS for their unwavering support.

I am deeply grateful for the opportunity to collaborate with numerous exceptional researchers within our extended research team. I extend my sincere gratitude to Dr. Li Wang for his intellectual generosity and steadfast encouragement. Our scholarly discussions on technical challenges and recreational badminton sessions have been both

intellectually stimulating and personally enriching. Special thanks are due to Dr. Zhuo Wang for his rigorous engagement in theoretical analyses of numerical simulations and physical mechanisms. I am particularly indebted to Dr. Yadong Deng, whose expertise in metasurface design and patient mentorship have been instrumental in advancing this work. I wish to acknowledge the invaluable contributions of our distinguished collaborators, Professor Chao Lu and Professor Alan Pak-Tao Lau, whose visionary insights shaped the research trajectory. Additionally, I recognize the critical support provided by: Dr. Jiaqi QU, Dr. Huaijian LUO, Dr. Shuyang CHEN, Dr. Yujian LEE, Dr. Weiming LYU, Mr. Jing ZHOU, Mr. Liwang LU, Mr. Qing Wang, Mr. Pin XU, Dr. Haoze YU and Mr. Jingming ZHANG.

Most importantly, I could never have completed this dissertation without my family's constant support. To those who always stood by me and helped me chase my academic goals, I want to say that words are not enough to show how thankful I am. "Thank you" feels too small compared to everything you've done for me, but I want you to know this work is a symbol of your strength. Because of your sacrifices, I was able to finish this journey. This thesis properly belongs to my family.

May 2025

Table of Contents

pages

List of aberrations

2D---------- two-dimensional

3D ---------- three-dimensional

B

BIC ---------- bound states in the continuum

F

FDTD---------- Finite-difference time-domain

FIB ---------- focused ion beam

FWHM ---------- full width at half maximum

L

LCP ---------- left-handed circularly polarized

LMA-PCF ---------- large-mode-area photonic crystal fiber

LP ---------- linear polarized

LSPR ---------- localized surface plasmon resonance

M

meta-fiber ---------- fiber-integrated metasurface

MFD ---------- mode field diameter

MMF ---------- multi-mode fiber

N

NA ---------- Numerical aperture

NIR ---------- Near-infrared

P

PAM4---------- 4-Level Pulse Amplitude Modulation

PB phase ---------- Pancharatnam-Berry phase

PML ---------- perfectly matched layer

Q

Q-factor ---------- quality-factor

R

RI ---------- refractive index

RCP ---------- right-handed circularly polarized

S

SMF ---------- single-mode fiber

SPR ---------- surface plasmon resonance

T

TIR---------- total internal reflection

X

XP ---------- *x*-polarized

Y

YP ---------- *y*-polarized light

List of tables

List of figures

Chapter 1 Introduction

The relentless pursuit of miniaturized, high-performance optical systems has catalyzed the emergence of meta-fiber devices, which integrate metasurfaces or graphene onto optical fibers to overcome inherent limitations of conventional free-space configurations. This chapter introduces the motivation and conceptual framework for meta-fiber technologies while addressing critical challenges in fabrication precision, mode confinement, and modal mismatch. Strategies to integrate planar nanophotonics with fiber-optic platforms are outlined, enabling compact, alignment-free devices for applications such as sensing, communication, and signal processing. Subsequent sections systematically analyze these challenges, present innovative solutions, and demonstrate experimental validations that seamlessly integrate metasurface functionalities with fiber-optic architectures, thereby laying the groundwork for next-generation integrated optical systems.

1.1 Meta-fiber devices: motivation and concept

The advancement of nanofabrication technologies has catalyzed an exponential surge in demand for optical devices that simultaneously deliver high performance and miniaturized configurations [*1-3*]. While conventional optical systems face inherent limitations in volume reduction, weight minimization, and functional integration, emerging applications, including spanning high-speed optical interconnects [*4*] and minimally invasive biomedical diagnostics [*5*], impose stringent requirements on the revolution of optical devices. Metasurfaces, as artificially engineered arrays of subwavelength meta-atoms, have revolutionized light-matter interactions by enabling unprecedented manipulation of electromagnetic wavefronts through precise control of phase, amplitude, and polarization profiles. Metasurfaces have demonstrated diverse applications ranging from advanced beam shaping [*6-9*], high-capacity optical communications [*10, 11*] to quantum computing architectures [*12, 13*].

Despite these significant advances, current metasurface implementations predominantly rely on free-space optical configurations requiring stringent alignment tolerances and complex, precise optical systems. These inherent limitations pose challenges for practical system integration and application. To address these challenges, we propose meta-fiber devices that epitomize the emerging "lab-on-fiber" paradigm [*14*] through integrating metasurfaces or two-dimensional materials (*e.g.*, graphene) on optical fiber platforms. The meta-fiber devices [*15*] synergistically combine the unique advantages of optical fibers, including inherent mechanical flexibility, telecom-standard compatibility, and plug-and-play connectivity, with the unprecedented light manipulation capabilities of metasurfaces and the exceptional optoelectronic properties of graphene. The proposed meta-fiber devices enable transforming conventional

passive devices into multifunctional active systems capable of on-fiber sensing, integrated signal processing, and multifunctional light manipulation.

Recent pioneering studies have preliminarily validated the concept through fiber-integrated devices performing beam steering, all-optical signal modulation, ultra-compact endoscopy, and broadband fiber polarizer, as systematically illustrated in Figure 1-1. These breakthroughs establish meta-fiber hybrid systems as pivotal components in advancing next-generation integrated optical systems, addressing the critical demand for monolithic compatibility between nanophotonic planar optics and fiber-based waveguide architectures.

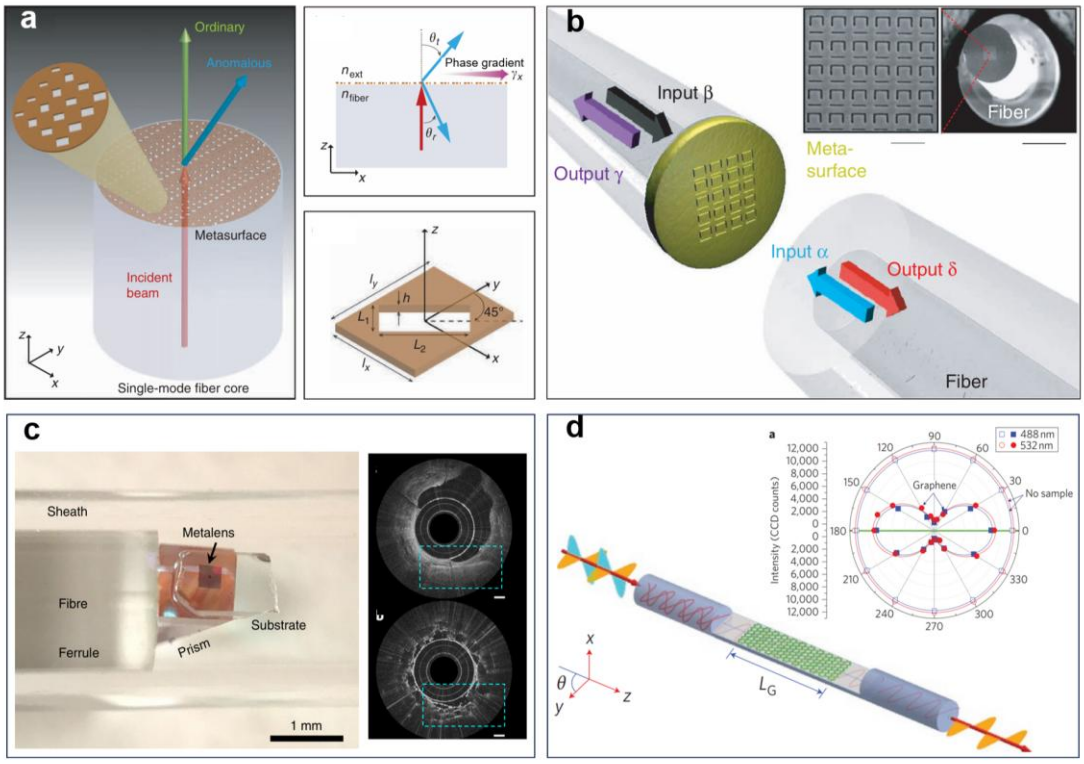

Figure 1-1 Fiber-integrated metasurface devices. (a) A single-mode fiber-integrated metasurface for beam steering and coupling[*16*]. **(b)** Schematic of a fiber-tip metasurface for all-optical signal modulation based on coherent absorption[*17*]. **(c)** Schematic and photographic image of the nano-optic endoscope and endoscopic imaging of ex vivo human lung resections[*18*]. **(d)** A broadband graphene polarizer based on D-shaped single-mode fiber[*19*].

However, the advancement of meta-fiber devices faces significant challenges that hinder their progress. The first obstacle arises from fabrication complexities associated with the unconventional geometry of optical fibers. Their submillimeter-scale diameter and high aspect ratios fundamentally conflict with standard planar nanofabrication protocols optimized for wafer-scale substrates. Thus, a precise fabrication flow for meta-fiber devices is necessary. A recent review[*20*] systematically categorizes current approaches into three paradigms: Top-down methods (*e.g.*, Focused ion beam (FIB) milling, chemical etching, etc.), Bottom-up techniques (*e.g.*, 3D direct laser writing), and material transfer. While these established methods enable the realization of multifunctional passive and active fiber-integrated devices, most of them inherently impose significant process complexity characterized by multistep fabrication sequences and stringent alignment requirements.

The second fundamental constraint arises from the limited mode confinement in optical fibers. Single-mode fibers (SMFs) demonstrate a characteristic mode field diameter (MFD) of ~10 μm at 1550 nm wavelength, imposing severe restrictions on their potential for multifunctional metasurface integration. This limitation originates from the requirement of numerous individual meta-atoms to construct intricate phase profiles. To overcome this spatial limitation, recent studies have adopted techniques such as 3D direct laser writing for fabricating a hollow tower (height ~50 μm) on fiber facets to enable beam expansion[*21, 22*], along with thermal fusion processing to insert multimode fiber (MMF) segments between SMFs and metasurfaces for equivalent beam expansion purposes [*23*]. Although these approaches demonstrate functional efficacy, they simultaneously introduce non-trivial fabrication complexities, particularly regarding sub-micron alignment precision and thermal deformation control during MMF-SMF splicing.

The third critical challenge originates from the inherent mode-mismatch between SMF fundamental modes and metasurface resonant modes. Guided modes in SMFs exhibit Gaussian-like intensity profiles with finite angular spectra (typical divergence angle $\theta \approx$ 5-8° at 1550 nm wavelength), fundamentally differing from the plane-wave excitation conditions required for angle-sensitive metasurface resonances. This fundamental limitation leads to significant performance degradation in meta-fiber devices, particularly for fiber-tip sensors demanding high-quality (Q) resonances, where mode mismatch induces linewidth broadening that compromises detection accuracy.

This thesis systematically addresses the aforementioned challenges with the concept and objectives shown in Figure 1-2. The light-matter interaction mechanisms in fiber-integrated metasurfaces or graphene are investigated via two integration strategies. For fiber-tip integration, a standardized FIB lithography process was developed to directly fabricate subwavelength metasurfaces on optical fiber substrates, achieving <10 nm structural precision while eliminating alignment errors and multi-step fabrication complexities inherent to conventional methods. Utilizing this platform, two functional devices were realized. The first is an ultrasensitive quasi-bound states in the continuum (BIC) metasurface fiber sensor. The proposed flat-band quasi-BIC resonance mechanism enables efficient coupling with the fundamental fiber mode, thereby addressing the spectral broadening issue caused by wavevector divergence angles. Experimental characterization confirms that the optimized flat-band quasi-BIC fiber sensor achieves both high Q-factor performance and ultrahigh sensitivity. The second device comprises a chiral metalens directly integrated onto a large-mode-area photonic crystal fiber (LMA-PCF) specifically selected for its 25 μm mode field diameter. Optical characterization reveals a focused beam diameter of 2.65 μm with exceptional

polarization selectivity, demonstrating an LCP to RCP extinction ratio exceeding 20 dB. The fabricated fiber chiral metalens is connected with a high-speed 4-level pulse amplitude modulation (PAM4) communication system for a polarization-modulated optical switch. For fiber-side integration, we developed a tunable D-shaped fiber polarizer incorporating hybrid gold-grating/graphene nanostructures. Systematic investigations of the mode-coupling mechanism between surface plasmon resonance (SPR) modes excited by the gold grating and SMF fundamental modes were conducted. This fiber-side integration platform demonstrates exceptional potential for achieving extended light-matter interaction lengths critical for high-performance optical devices.

These meta-fiber devices preserve the intrinsic advantages of mechanical flexibility, low transmission loss, and alignment-free operation in optical fibers, while unlocking advanced functionalities previously unattainable in conventional fiber-optic systems. Our work establishes a foundational framework for transitioning metasurface technologies from laboratory-scale demonstrations to integrated optical applications.

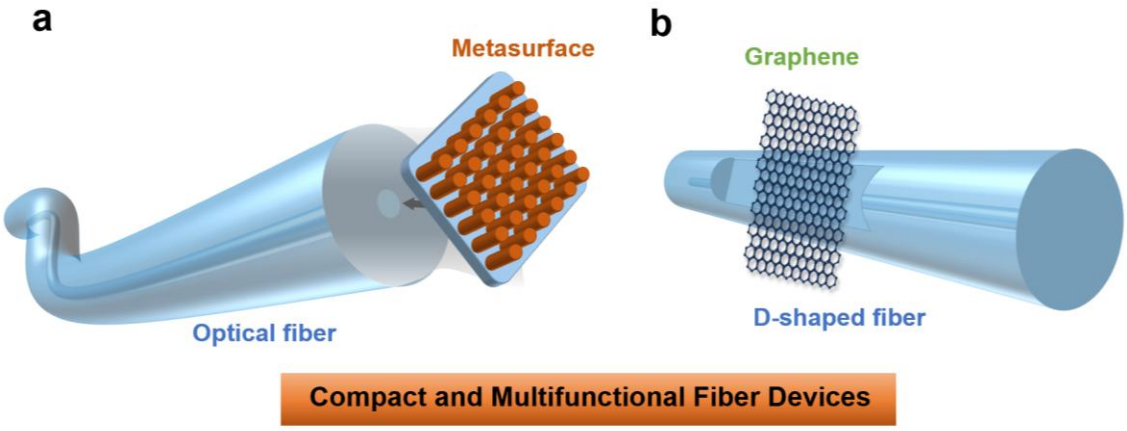

Figure 1-2 The thesis aims to study the light-matter interaction of the fiber-integrated platform combining multifunctional metasurface or graphene to realize compact and active optical devices. **(a)** fiber-tip integrated metasurface and **(b)** fiber-side integrated graphene illustrate two main integrated methods.

1.2 Thesis outline

The integration of optical fibers with metasurfaces creates a synergistic platform that combines the unparalleled wavefront manipulation capabilities of metasurfaces with the inherent advantages of optical fibers, including compact footprint and alignment-free operation. This thesis systematically investigates light-matter interaction mechanisms of the meta-fiber platform and experimentally demonstrates three advanced meta-fiber devices targeting distinct functionalities.

Chapter 1 establishes the research framework by methodically presenting the motivation, technical challenges, and specific objectives. Three fundamental limitations constraining the advancement of meta-fiber devices are rigorously characterized, with corresponding solutions systematically engineered and validated in subsequent chapters.

Chapter 2 states metasurface modulation principles and their practical applications. A focused technical review is conducted on emerging meta-fiber integration architectures and graphene-empowered tunable fiber devices, thereby laying the theoretical foundation for the device innovations systematically demonstrated in Chapters 3–5.

Chapter 3 systematically demonstrates the fiber-tip metasurface fabrication process, incorporating optimized FIB etching parameters. By leveraging this advanced fabrication protocol, we demonstrate a meta-fiber sensor employing symmetry-protected BIC to achieve high-Q-factor resonances for refractive index sensing applications. The designed metasurface enables ultrasensitive refractive index detection (529.1 nm/RIU) while retaining the intrinsic advantages of optical fibers: low-loss signal transmission and plug-and-play compatibility with optical systems.

Chapter 4 presents a fiber-integrated metalens fabricated through the established fiber-tip metasurface fabrication flow. Leveraging planar chiral meta-atoms, the device achieves exceptional circular dichroism, exhibiting a high LCP to RCP light intensity ratio across the C-communication band. The chiral metalens enables experimental demonstration of a polarization-modulated all-optical switch system. System-level characterization in a 2 Gbps PAM4 optical communication testbed reveals a switching response time of ~500 μs and polarization extinction ratio exceeding 20 dB.

Chapter 5 is a proof-of-concept of the dynamic tunability of fiber-optic devices through the integration of graphene and gold grating structures. We propose a tunable D-shaped fiber polarizer where the strong coupling between the fiber fundamental mode and SPR is actively modulated via graphene's chemical potential. This tunable interaction enables continuous wavelength-selective filtering, with the device's optimal operational wavelength dynamically spanning the entire C-communication and O-communication band. This work establishes a robust platform for on-chip tunable optical devices.

Chapter 6 synthesizes the dissertation's contributions while critically evaluating persistent challenges and emerging opportunities in fiber-integrated metasurfaces.

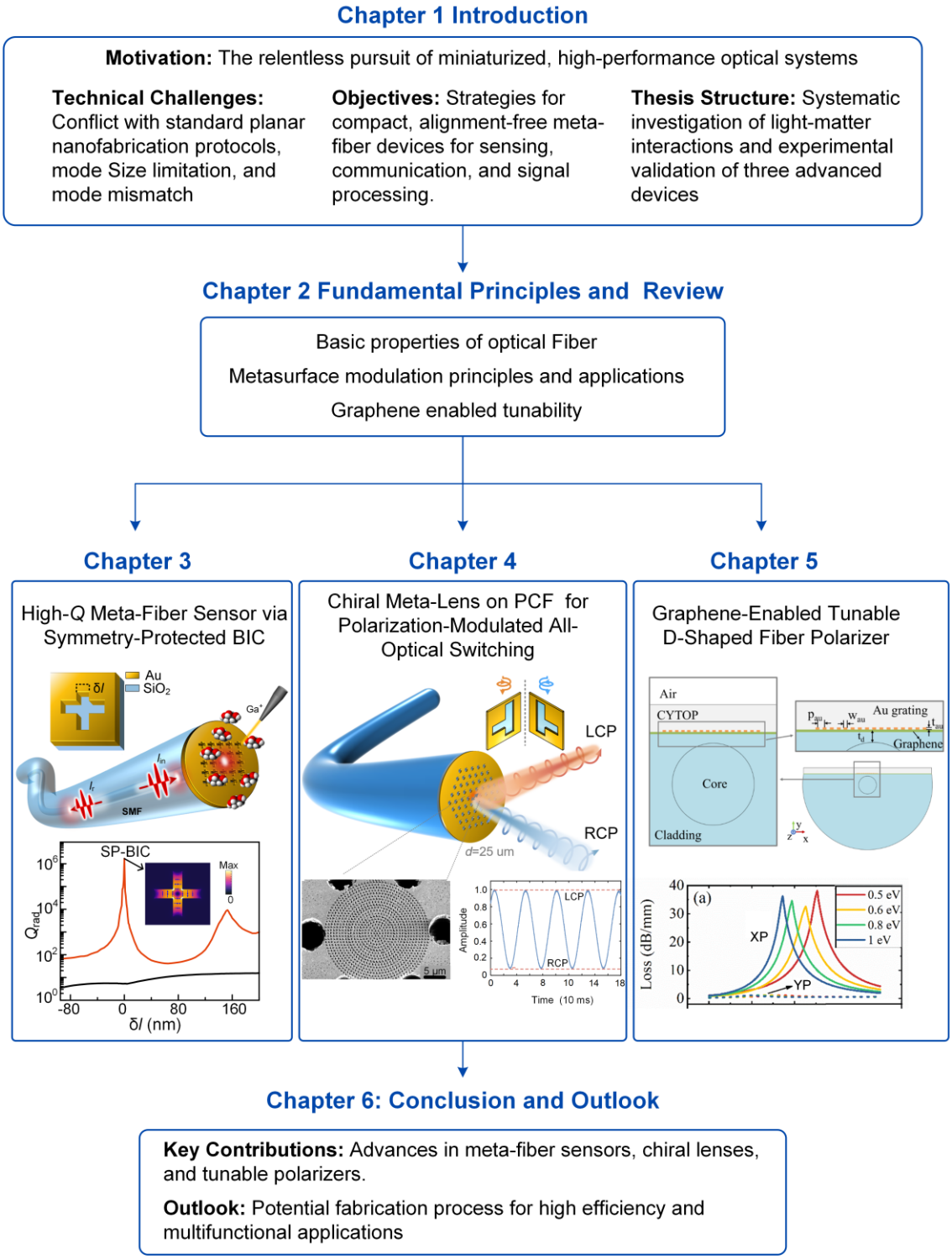

Figure 1-3 Schematic overview of the thesis outline.

Chapter 2 Fundamental Principles and Review

This chapter systematically examines the foundational principles underlying optical fibers, metasurface, and graphene-enabled tunability. The analysis begins with the essential characteristics of optical fibers, focusing on Gaussian beam output profiles, mode field diameter quantification, and guided-mode propagation mechanics. Then, we subsequently investigate metasurface modulation strategies, particularly phase-engineered wavefront manipulation and bound states in the continuum (BIC) enhanced meta-devices, emphasizing their transformative applications in high-performance devices and systems. The discussion further extends to emerging hybrid systems integrating low-dimensional materials with fiber platforms. Special attention is given to graphene-enabled dynamic tunability mechanisms, where chemical potential modulation via electrostatic gating enables real-time reconfiguration of light-matter interactions. Collectively, these theoretical foundations and practical applications provide a rigorous foundation for subsequent chapters, establishing both the physical principles and technological viability of next-generation integrated optical systems.

2.1 Basic Properties of Optical Fiber

Optical fibers, functioning as the backbone of modern telecommunication and sensing systems, have undergone revolutionary development since Kao's seminal discovery that ultrapure silica purification enables unprecedented attenuation reduction in optical waveguides [*24*]. This breakthrough achieved fiber losses below 0.3 dB/km, meeting the critical threshold for practical long-distance photonic networks. Conventional fibers relying on total internal reflection (TIR) mechanisms intrinsically lack dynamic light-field manipulation capabilities at subwavelength scales, restricting their functionality to passive light-guiding roles. Nevertheless, their unique advantages, including exceptional mechanical flexibility, enhanced light confinement through refractive index contrast (Δn), and low-loss long-haul transmission capabilities, remain indispensable for foundational optical architectures. As schematically depicted in Figure 2-1, a standard SMF comprises three stratified layers: a germanium-doped silica core exhibiting a higher refractive index (n_1) than the pure silica cladding (n_2), satisfying the TIR condition $\Delta n = n_1 - n_2 > 0$, a cladding layer defining the waveguide geometry; and a protective polymer coating protecting the fragile internal fiber and minimizing external perturbations.

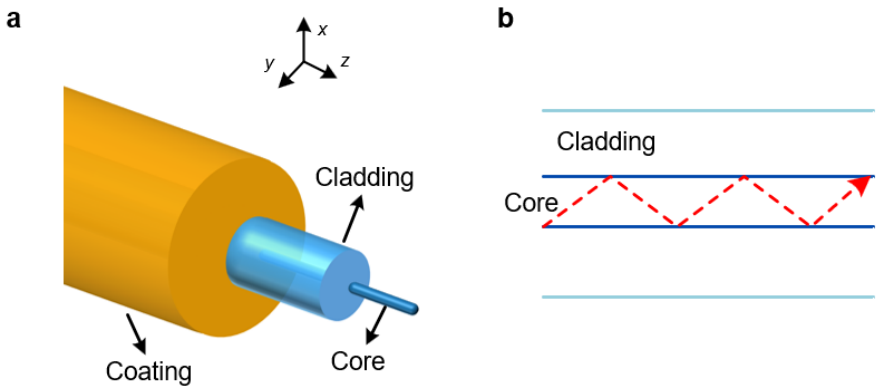

Figure 2-1 Schematic of standard SMF.

The commercial standard optical fiber (*e.g.*, step-index fiber) is typically composed of fused silica due to its extremely low optical attenuation in the visible and near-infrared bands. The fiber core consists of GeO_2-doped silica with 4% weight concentration, designed to achieve a higher RI than the surrounding cladding for TIR-based light transmission. In linear optics, isotropic silica exhibits a nominal refractive index RI (n) of approximately 1.45, and its dispersion properties can be effectively described by the Sellmeier formula, a widely adopted model for characterizing fused silica [*25*]. For nonlinear optical phenomena, the dominant nonlinear response in isotropic silica arises from the third-order nonlinear susceptibility. Consequently, the wavelength-dependent material refractive index $n(\lambda)$ of silica (for both the doped core and cladding regions) can be modeled as follows:

$$n(\lambda) = \sqrt{1 + \frac{A_1\lambda^2}{\lambda^2 - B_1^2} + \frac{A_2\lambda^2}{\lambda^2 - B_2^2} + \frac{A_3\lambda^2}{\lambda^2 - B_3^2}} \tag{2-1}$$

where, A_1= 0.6961663, A_2= 0.4079426, A_3= 0.8974794, B_1= 0.0684043, B_2= 0.1162414, B_3= 9.896161 are coefficients. λ is the wavelength of the propagation light.

2.1.1 Mode analysis

The electromagnetic modes propagating in optical fibers can be rigorously derived by solving Maxwell's equations under the weak-guidance approximation ($\Delta n \ll 1$), which is valid for most commercial fibers with RI index contrasts below 1% [*26*]. The spatial mode distributions and the total number of guided modes are governed by four key parameters: the core radius (a), refractive index (RI) profiles of the core (n_1) and cladding (n_2), and the operating wavelength (λ). These relationships can be quantified through the normalized frequency parameter V, as defined by,

$$V = \frac{2\pi a}{\lambda}\sqrt{n_1^2 - n_2^2} \approx \frac{2\pi a}{\lambda} \bullet NA \tag{2-2}$$

Where, $NA = \sqrt{n_1^2 - n_2^2}$ represents the numerical aperture of an SMF. A higher V-value indicates greater mode-carrying capacity in the optical fiber. When V exceeds the critical value of 2.405, the fiber transitions from single-mode to multimode operation. To illustrate, consider a multimode fiber with core diameter a = 20 μm, operating at λ = 1.55 μm with n_1 = 1.47 and n_2 = 1.45. Calculation using Equation 2-2 yields $V \approx$ 24.5, confirming substantial multimode propagation. Figure 2-2 demonstrates the electric field and phase distributions for the first six guided modes, including the fundamental LP_{01} mode and higher-order modes (LP_{02}, LP_{11}, LP_{21}).

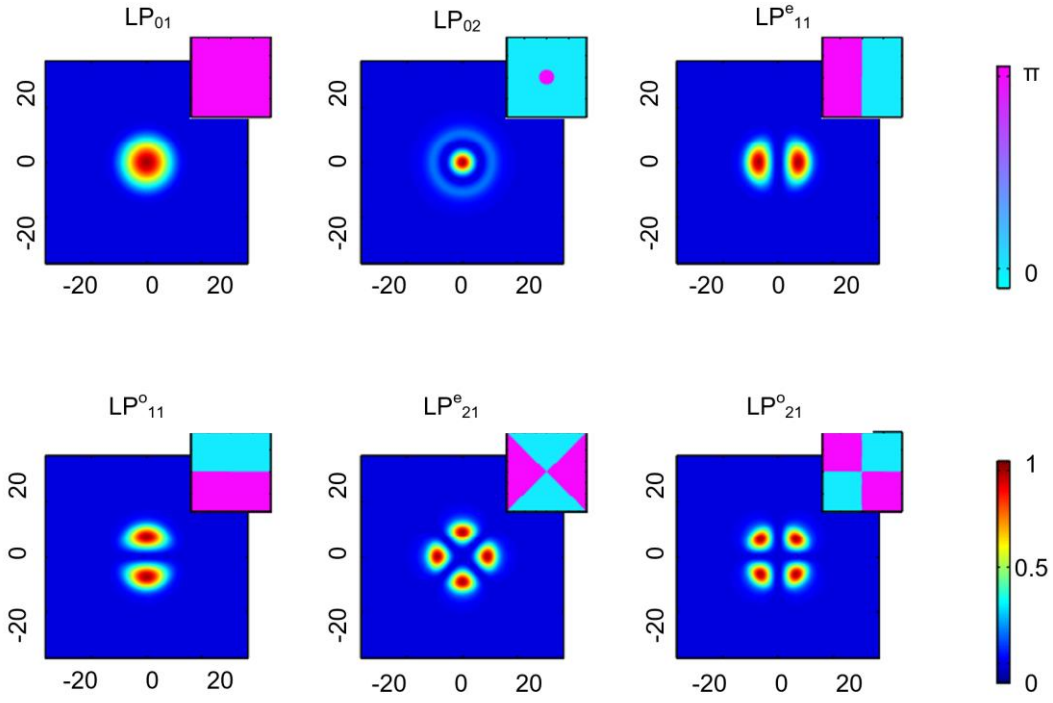

Figure 2-2 Amplitude and phase distributions of six linear polarized (LP) guided modes propagating in a multimode fiber with dimensions in μm [*26*].

In multimode fibers (MMFs), the continuous superposition of these modal field amplitudes and phase distributions creates complex interference patterns that significantly influence metasurface wavefront modulation. While single-mode fibers

(SMFs) eliminate modal interference through fundamental mode operation, their constrained mode field diameter (typically ~10 μm) imposes practical limitations on achieving full 2π phase coverage with metasurfaces. This fundamental trade-off between multimode functionality and single-mode spatial constraints constitutes a critical design consideration when integrating metasurfaces on optical fibers.

2.1.2 Beam divergence

The output from a fiber tip exhibits a Gaussian-like beam profile. Considering an SMF with an 8.2 μm core diameter and 125 μm cladding diameter (SMF-28e specification), the system can be numerically modeled using finite-element methods (FEM). The electromagnetic field distribution within the fiber maintains cylindrical symmetry, as shown in Figure 2-3.

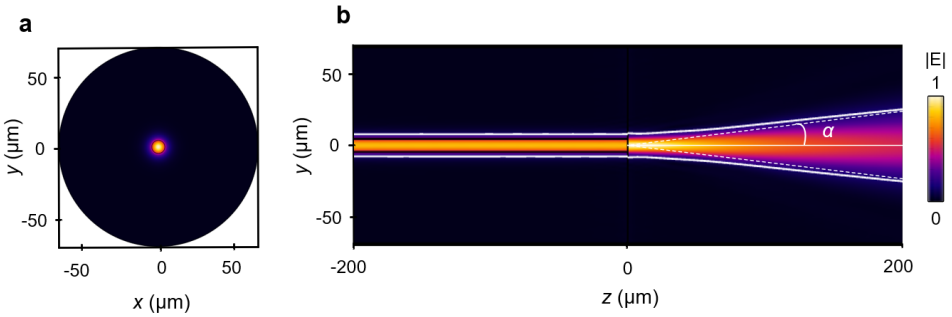

Figure 2-3 Numerical analysis of the Gaussian beam propagation of an SMF tip. (a) Cross-sectional of the output electric field distribution of the fundamental mode. **(b)** side-view profiles of the electric field distribution. The divergent angle (α) is defined at the 1/e amplitude point of the Gaussian beam.

Numerical solutions demonstrate that the fundamental mode presents a Gaussian-like field profile, characterized by transverse electric field distributions around the fiber tip. Figure 2-3b specifically depicts Gaussian beam propagation from the SMF tip, where the beam waist spatially coincides with the fiber termination. The mode field diameter

(MFD), defined as the transverse dimension at the 1/*e* intensity threshold of the electric field profile at the fiber facet, corresponds to twice the beam waist ($2\omega_0$).

The scalar wave equation under paraxial approximation yields the Gaussian beam solution, whose electric field distribution is expressed as,

$$E(r,z)=\frac{E_0}{\omega(z)}\exp(-\frac{r^2}{\omega^2(z)})\exp\left\{-j\left[kz-\tan^{-1}\left(\frac{z}{z_0}\right)+\frac{kr^2}{2R(z)}\right]\right\} \tag{2-3}$$

Where $r=\sqrt{x^2+y^2}$ denotes the radial coordination, $\omega(z)=\omega_0\sqrt{1+\left(z/z_R\right)^2}$ represents the beam radius along the direction *z* axis, $R(z)=z\left(1+\left(z_R/z\right)^2\right)$ is the Wavefront curvature radius, and $z_R=\pi\omega_0^2/\lambda$ defines the Rayleigh range. The first exponential term governs the amplitude distribution, characterizing the transverse beam confinement. The second exponential term describes the phase evolution, comprising a spherical wavefront component ($-j(kr^2/2R(z))$) and the Gouy phase shift ($j\tan^{-1}\left(z/z_0\right)$). In the condition of far field ($z \gg z_R$), the beam radius can be approximately as,

$$\omega(z)\approx\omega_0\frac{z}{z_R} \tag{2-4}$$

The divergence angle α, defined as the asymptotic angular spread of the beam (full width at 1/*e* intensity), is derived from geometric considerations of the beam edge propagation,

$$\alpha=\frac{\omega(z)}{z}\approx\frac{\lambda}{\pi\omega_0} \tag{2-5}$$

Figure 2-4 illustrates the characteristic Gaussian beam propagation profile, highlighting the quantitative relationship between the beam waist ω_0, Rayleigh range z_R, and

divergence angle α. The optical output from the single-mode fiber tip exhibits a quasi-Gaussian beam profile. However, its wavefront curvature and phase distribution deviate significantly from those of an ideal plane wave, necessitating careful consideration of these properties in metasurface modulation design. Importantly, in the near-field regime ($z \ll z_R$), beam divergence becomes negligible, and the Gaussian beam wavefront can be approximated as planar. Under this approximation, the near-field electric field simplifies to,

$$E(r,z) \approx \frac{E_0}{\omega_0}\exp(-\frac{r^2}{\omega_0^2})\exp\left[-j\left(kz-\frac{z}{z_R}\right)\right] \tag{2-6}$$

The resulting phase profile is dominated by a linear propagation term kz with a minor nonlinear correction from the Gouy phase shift ($-z/z_R$). This fundamental relationship implies that metasurfaces fabricated directly on fiber tips may omit explicit consideration of the incident beam's phase profile under near-field conditions. Furthermore, increasing the beam waist ω_0 enhances the similarity between the near-field electric field distribution and that of an ideal planar wave and enhances metasurface operation efficiency.

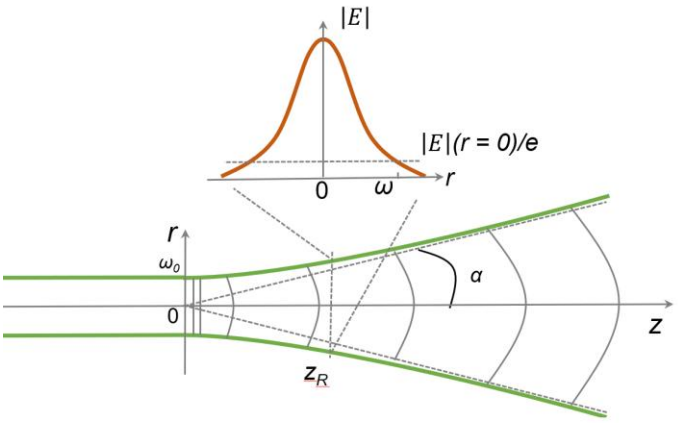

Figure 2-4 Gaussian beam propagation profile of output from an SMF.

While the Gaussian beam waist exhibits a quasi-planar wavefront at the near-field condition, the fiber output inherently contains wavevectors with angular divergence components (Figure 2-5). This divergence critically impacts resonant metasurface performance; even slight angular deviations may substantially degrade the quality factor (Q) of BIC-based metasurfaces. For SMF-28 fiber, the calculated far-field divergence angle is 5.5° across the wavelength range (1.2–1.6 μm), as characterized in Figure 2-5. Both the divergence angle and mode field diameter (10.4 μm at 1550 nm) constitute essential parameters for metasurface fabrication tolerance and optical coupling efficiency optimization, as detailed in subsequent chapters.

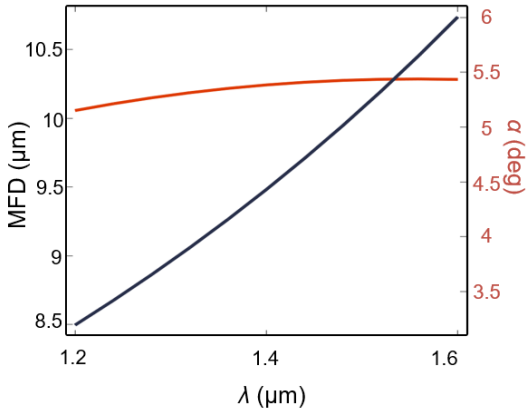

Figure 2-5 MFD calculated at the 1/*e* amplitude of the Gaussian beam and the corresponding far-field divergence angles.

2.1.3 Spectra broadening problem

Numerous studies have reported spectral broadening when fabricating structures on optical fiber tips. For instance, a design featuring a nanoring exhibits a reflectance full-width at half-maximum (FWHM) of ~20 nm under plane wave incidence, yet this broadens to >50 nm when fabricated on an SMF tip [*27*]. Similarly, a fiber-tip SPR sensor—formed by splicing a MMF to a gold-coated SMF—demonstrates two distinct resonance valleys in plane-wave simulations, but experimental results show severe

spectral broadening [*28*]. Another study explored photonic crystal cavities with aperiodic gratings on fiber tips to confine light to the core region; while this approach partially mitigated broadening, the resulting structure was prohibitively large [*29*]. Here, we designed a period-asymmetric grating that achieves a sharp reflectance peak (FWHM ~ 5 nm) under plane-wave incidence at $\lambda \approx 1.6$ μm (Figure 2-6b). However, when simulated in a fiber waveguide model (Figure 2-6a), the reflectance broadened significantly (Figure 2-6b). Consistent with this trend, experimental fabrication of the grating on an SMF tip resulted in severely broadened reflectance spectra, as shown in Figure 2-6d. Thus, the spectra broadening problem is an important issue to be solved when fabricating a resonance metasurface on the fiber tip.

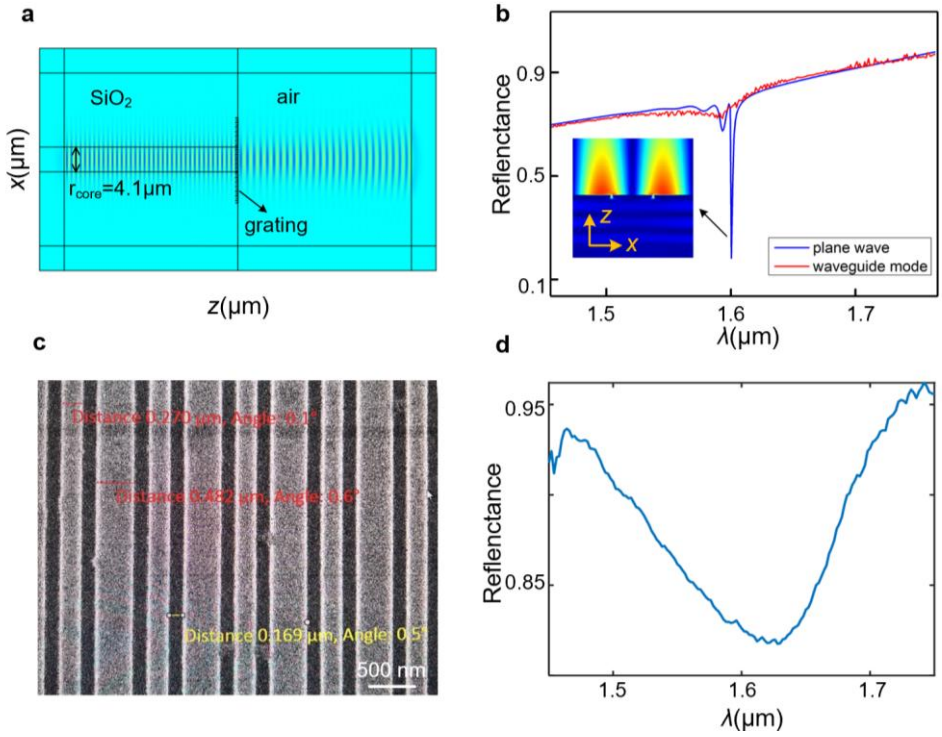

Figure 2-6 Numerical and experimental results of gratings on SMF. (a) Electric field distribution in an SMF model. **(b)** The reflectance under plane wave incidence and under fiber waveguide mode excitation. **(c)** The fabrication result on fiber tip. **(d)** Experimental reflectance of the fabricated fiber device.

2.2 Metasurface: Theory and Applications

Metasurface traces its conceptual origins to metamaterials—artificially structured arrays comprising subwavelength metallic or dielectric resonators that interact with electromagnetic waves through engineered electric and magnetic responses [*30*]. While 3D metamaterials demonstrated extraordinary phenomena such as negative refractive indices, near-zero permittivity, and ultrahigh effective permeability, their practical deployment has been hindered by intrinsic challenges: high ohmic losses in metallic components, pronounced dispersion effects, and nanofabrication complexities associated with 3D architectures [*31*]. As a two-dimensional counterpart, metasurface inherits the wavefront-shaping capabilities of metamaterials while circumventing these limitations through planar geometry. This dimensional reduction enables compatibility with established nanolithography techniques, including electron beam lithography (EBL), FIB milling, and two-photon polymerization (TPP), thereby facilitating scalable manufacturing of high-efficiency devices. By strategically arranging subwavelength meta-atoms, metasurface exerts precise control over electromagnetic wave properties, such as amplitude, phase, polarization, and orbital angular momentum, with ultra-thin interfaces. In the following paragraphs, we explain the metasurface modulation theory and practical applications relative to this thesis.

2.2.1 Gradient metasurface

Gradient metasurfaces, renowned for their exceptional wavefront manipulation capabilities, have emerged as a transformative platform for realizing anomalous optical phenomena such as abnormal reflection/refraction, subwavelength focusing, and vortex beam generation [*32*]. The operational foundation of gradient metasurface resides in

the engineered discontinuity of optical phase profiles of the interface, which a generalized Snell's law can explain. In 2011, a generalized law of refraction and reflection was established [*33*], extending Snell's law to a wider explanation. These laws extend traditional Snell's relations to account for abrupt phase gradients dφ engineered at the metasurface interface. For abnormal refraction, the generalized form can be derived as,

$$\begin{cases} n_t \sin(\theta_t) - n_i \sin(\theta_i) = \dfrac{\lambda}{2\pi} \dfrac{\mathrm{d}\phi}{\mathrm{d}x} \\ \cos(\theta_t)\sin(\varphi_t) = \dfrac{\lambda}{2\pi n_t} \dfrac{\mathrm{d}\phi}{\mathrm{d}y} \end{cases} \tag{2-7}$$

For abnormous reflectance, the generalized form is,

$$\begin{cases} \sin(\theta_r) - \sin(\theta_i) = \dfrac{\lambda}{2\pi n_i} \dfrac{\mathrm{d}\phi}{\mathrm{d}x} \\ \cos(\theta_r)\sin(\varphi_r) = \dfrac{\lambda}{2\pi n_i} \dfrac{\mathrm{d}\phi}{\mathrm{d}y} \end{cases} \tag{2-8}$$

Where, n_t, n_i denote the refractive indices of incident and transmitted media, respectively. θ_i, θ_r, and θ_t denote the corresponding angles to the z axis, and λ is the free-space wavelength (Figure 2-7).

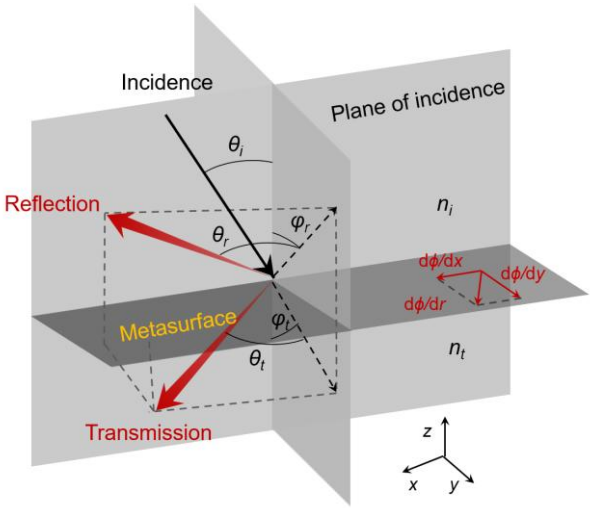

Figure 2-7 Generalized Snell's law of anomalous refraction and reflection induced by discrete phase delays of metasurface [*34*].

A metasurface imposes gradient phase delays $d\phi/dx$ and $d\phi/dy$ along the x- and y-directions, respectively, at the interface. These phase gradients enable anomalous reflection, redirecting incident light to out-of-plane angles θ_r (x-direction) and φ_r (y-direction), while simultaneously achieving anomalous refraction with transmitted angles θ_t (x-direction) and φ_t (y-direction). Through precise design of the interfacial phase profile, both reflected and transmitted beams can be arbitrarily controlled in three-dimensional space. This wavefront manipulation is realized via spatially varying meta-atoms that provide discrete phase shifts ($d\varphi$) at subwavelength resolution. By engineering the geometric parameters of these meta-atoms, the metasurface can achieve anomalous beam steering, focusing, and optical vortex generation.

There are three dominant strategies have emerged for designing suitable meta-atoms capable of providing full 2π phase coverage, enabling the implementation of phase gradient [*35, 36*],

Resonance Phase. Resonance-based phase control exploits electromagnetic resonant phenomena to manipulate the scattering phase profile of metasurfaces precisely. This fundamental mechanism enables phase modulation through strategic geometric modifications of meta-atoms, thereby tailoring their resonant characteristics. Three distinct metasurface structures exemplify this working principle,

(1) For plasmonic metasurface, taking the V-shaped nanoantenna arrays as an example, the localized surface plasmon resonance (LSPR) condition is controlled by modulating two geometric parameters, the arm length (L) and the opening angle (Δ). The dual-parameter tuning enables simultaneous wavelength-dependent and polarization-dependent phase modulation, critical for broadband dispersion control.

(2) For hybrid MIM metasurface [*37*], the confined electromagnetic resonance modes in the dielectric spacer layers exhibit strong field enhancement. By engineering the

upper metallic nanorods' dimensions, the rod width (w) and length (L) tune Fabry-Perot resonance conditions, π phase delay can be achieved.

(3) For all-dielectric Huygens' metasurface [*38*], high-RI dielectric nano-disks enable spectral overlap of electric and magnetic dipole resonances. The key design principles rely on the disk diameter and the period. The observed effect is polarization-independent, polarization-preserving, and robust, and the operation wavelength can be scaled by the geometrical parameters of the nano-disk metasurface [*39*].

Geometric Phase (PB phase): The Pancharatnam-Berry (PB) phase mechanism represents a fundamental methodology in metasurface design, exploiting polarization-dependent phase accumulation through spatially rotated anisotropic meta-atoms. This geometric phase approach manifests when a birefringent unit cell with orientation angle θ induces polarization conversion, as described by Jones matrix analysis. The cross-polarized transmission component acquires a geometric phase delay $\phi = 2\sigma\theta$, where $\sigma = \pm 1$ corresponds to LCP or RCP incidence,[*34*]

$$\boldsymbol{J} = \boldsymbol{R}(-\theta)\begin{bmatrix} t_{\mathrm{o}} & 0 \\ 0 & t_{\mathrm{e}} \end{bmatrix}\boldsymbol{R}(\theta) \tag{2-9}$$

$$\boldsymbol{E}_{\mathrm{t}}^{\mathrm{R/L}} = \frac{t_o + t_e}{2}\boldsymbol{E}_{\mathrm{i}}^{\mathrm{R/L}} + \frac{t_{\mathrm{o}} - t_{\mathrm{e}}}{2}\exp(2\sigma\theta)\boldsymbol{E}_{\mathrm{i}}^{\mathrm{L/R}} \tag{2-10}$$

Here, $\boldsymbol{E}_{\mathrm{t}}$ and $\boldsymbol{E}_{\mathrm{i}}$ represent the transmitted and incident electric field vectors, t_{o} and t_{e} denote the transmission coefficients along the slow and fast axes of the meta-atom, R and L, the RCP and LCP light, $\boldsymbol{R}$ correspond to the rotation matrix with angle θ,

$$\mathbf{R}(\theta) = \begin{bmatrix} \cos\theta & -\sin\theta \\ \sin\theta & \cos\theta \end{bmatrix} \tag{2-11}$$

The geometric phase mechanism enables polarization-selective wavefront manipulation through spin-orbit interactions, with key applications encompassing

chiral beam steering. As demonstrated in Figure 2-8, the PB phase exhibits inverse correlations between LCP and RCP components, manifesting complementary phase gradients with opposite signs. Meanwhile, the PB phase exhibits negligible wavelength-dependent dispersion over the operational bandwidth.

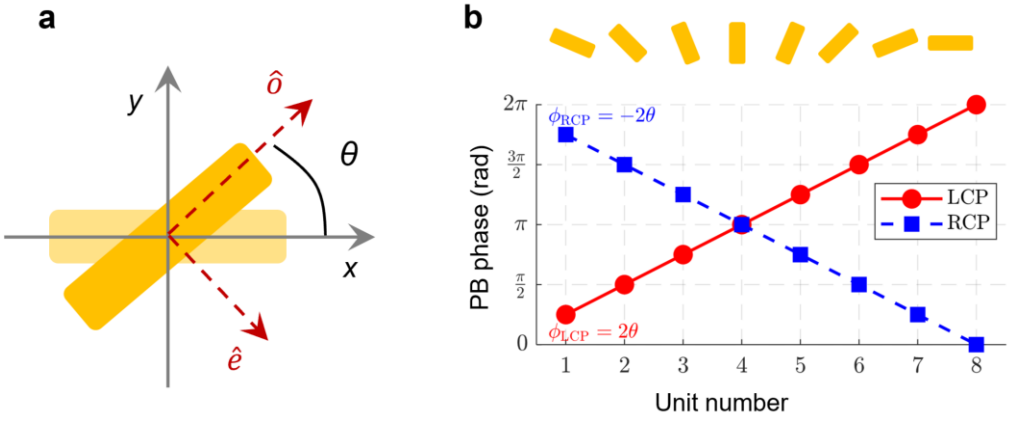

Figure 2-8 Geometric phase. (a) Schematic of a meta-atom with rotation angle θ between its slow axis and the x-axis. **(b)** Eight meta-atoms with rotation angle θ ranging from π/8 to π, generating phase delay of $\phi = +2\theta$ for LCP and $\phi = -2\theta$ for RCP illumination.

Propagation Phase: Propagation phase modulation, predominantly utilized in dielectric metasurfaces, leverages the optical path difference ($n_{\text{eff}} \cdot \Delta L$) accumulated by light propagating through high-aspect-ratio meta-atoms. Here, n_{eff} represents the effective RI determined by the meta-atom material and its cross-sectional geometry. Thus, by independently tailoring the cross-sectional geometry (*e.g.*, nanopillar diameter) and vertical dimensions, these parameters can be synergistically optimized to achieve full $0 - 2\pi$ phase coverage while maintaining high transmission efficiency. Crucially, this mechanism exhibits polarization insensitivity when utilizing rotationally symmetric unit cells (*e.g.*, cylindrical nanopillars), making it ideal for applications requiring operation such as highly efficient metalens. Recently, high-contrast metasurface [*40*] with strong effective RI disparities has emerged to largely enhance

propagation phase modulation efficiency through large light confinement and phase accumulation along the meta-atoms.

Design flow of gradient metasurface. The general design workflow of conventional gradient metasurfaces is illustrated in Figure 2-9. The procedure begins by defining the meta-atom periodicity, material composition, and substrate selection based on the operational wavelength (period $p < \lambda/2$ and high light transmission). Subsequently, the geometric parameters of the meta-atoms (e.g., width and length for propagation-phase-based designs) are systematically varied to compute their electromagnetic responses through numerical solutions of Maxwell's equations (*e.g.* by Finite-Different Time-Domain (FDTD)) at the target wavelength. This process generates a comprehensive library of amplitude and phase profiles corresponding to distinct meta-atom geometries.

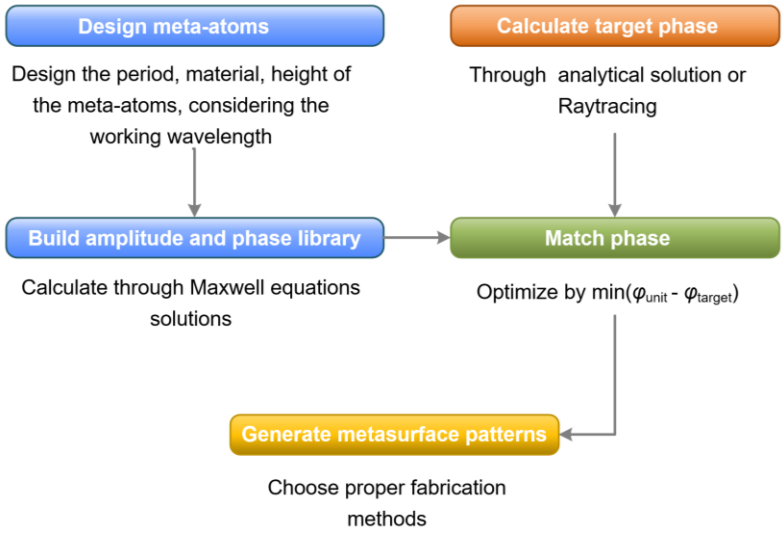

Figure 2-9 Flow of classical gradient metasurface design.

In parallel, the target phase distribution for the metasurface must be derived, either through analytical formulations or computational tools such as ray-tracing software (e.g., Zemax, Code V). For instance, in anomalous reflection applications, the required phase profile is given by $\varphi(x) = 2\pi x \sin(\theta) / \lambda$, where x denotes the lateral position of the meta-atom, θ is the reflection angle, and λ is the operational wavelength. The final

metasurface configuration is synthesized by selecting meta-atoms from the precomputed library that minimize the phase discrepancy between the target profile and the achievable phase response. Fabrication methods are then optimized according to the metasurface's geometric parameters (e.g., metasurface size, meta-atom thickness) and material properties. A detailed application of this design methodology will be provided in Chapter 4.

2.2.2 Resonant metasurface: Bound states in the continuum

The emergence of metasurfaces has revolutionized optical device design, enabling unprecedented optical control at subwavelength scales. While early implementations primarily leveraged gradient-phase manipulation for wavefront shaping (*e.g.*, metalenses with large NA), recent advances have exploited more sophisticated physical mechanisms. Among these, bound states in the continuum (BICs) [*41-43*] have emerged as an exciting physical mechanism for realizing devices with sharp resonances and strong near-field enhancements. Although BICs were first introduced in quantum mechanics [*44*], it is a general wave phenomenon that can be identified in a wide range of optical systems, including optical waveguides [*45*], photonic crystals [*42*], and dielectric gratings [*46*]. In periodic nanostructures, like metasurfaces, a common way to construct BICs is to eliminate the coupling of resonant modes to all radiation channels by adopting structural symmetry [*47*]. Theoretically, ideal BICs have infinite *Q*-factors, which are incompatible with far-field excitation. In practical applications, intentional symmetry breaking is usually introduced to convert ideal BICs into quasi-BICs that retain finite *Q*-factors and become accessible from the far field.

Recent research on BIC metasurfaces has gained significant momentum owing to their unique advantages over conventional resonant systems. BIC properties such as

resonance wavelength and *Q*-factor can be precisely engineered through metasurface geometry. Metasurfaces offer compact form factors compatible with integrated photonic platforms. The engineered platforms enable extreme light confinement with ultrahigh *Q*-factors, demonstrating unprecedented applications in ultrasensitive molecular detection [*48-50*], nonlinear optics [*51*], and low-threshold lasers [*52-54*].

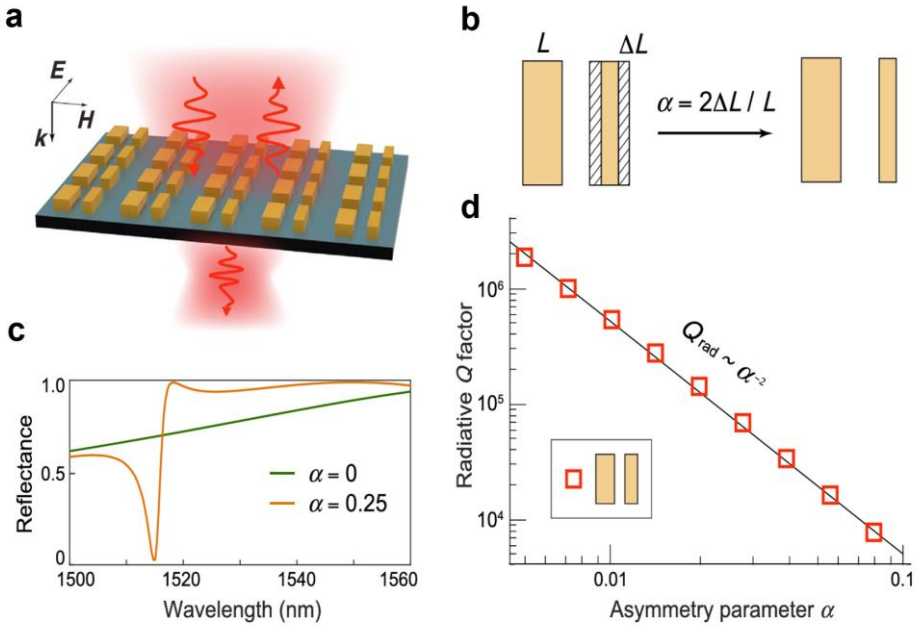

Figure 2-10 Symmetry-broken tuning BIC under vertical incidence. (a) Schematic illustration of light scattering by a metasurface with periodic asymmetric bar pairs, where α represents the asymmetry parameter [*55*]. **(b)** Definition of the asymmetry ratio α and **(c)** wavelength-dependent reflectance spectra for varying α values. **(d)** Inverse proportionality between the radiative quality factor and $\sqrt{\alpha}$.

Generally, there are two classifications of BICs. The first type is the symmetry-protected BIC (SP-BIC), which arises from the perfect destructive interference of symmetrical modes within the same channel. The second type, the Friedrich–Wintgen (FW) BIC, is typically generated through the destructive interference of two or more distinct modes [*56*]. Figure 2-10a illustrates a typical SP-BIC metasurface comprising pairs of bars with width asymmetry. Breaking the structural symmetry transforms the

BIC into a quasi-BIC resonance, exhibiting a sharp Fano-like spectral profile. Notably, the Q-factor exhibits an inverse quadratic dependence on the asymmetry parameter α ($\alpha = \Delta L/L$, where ΔL is the width difference between the two bars) in log-log scale, as demonstrated in Figure 2-10d. This inverse quadratic relationship has been generalized to all SP-BIC metasurfaces under appropriate definitions of α [*57*].

Beyond geometric asymmetry tuning, angular incidence modulation constitutes a well-established methodology for BIC modulation in metasurface. As illustrated in Figure 2-11, periodic nanostructures exhibit destructive interference-induced resonance suppression under vertical incidence. Deviation from normal incidence triggers a phase-matching transition where constructive interference dominates, thereby converting the suppressed BIC into a leaky quasi-BIC mode with exceptional spectral confinement and extreme high Q factors. This angular dependence enables deterministic spectral engineering through θ-modulation, which exhibit narrowband resonances but pronounced sensitivity to incident angle variations [*58*].

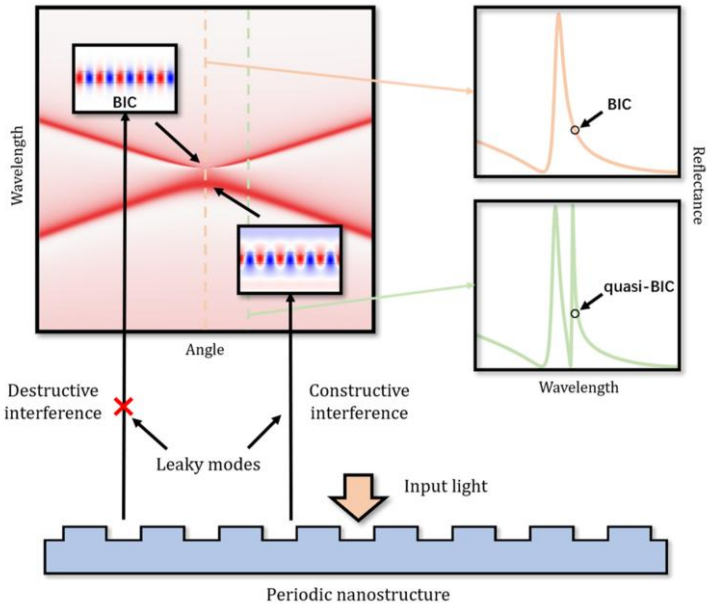

Figure 2-11 Incident-angle-modulated BIC. Physical mechanism of BICs and quasi-BICs in a periodic nanostructure with different angles of excitation [*58*].

Experimental realizations of BIC devices face significant challenges due to their extreme sensitivity to structural perturbations, where sub-degree angular deviations can induce substantial resonant wavelength shifts (>5 nm/°) and Q factor degradation. The translation from theoretical designs to functional devices is fundamentally constrained by three synergistic limitations: the vulnerability of BIC modes to fabrication-induced error, the sub-10 nm precision requirements for sustaining symmetry-breaking meta-atom configurations, and intrinsic material losses that impose fundamental limits on attainable Q factors, particularly in plasmonic metasurfaces. These constraints collectively underscore the need for advanced fabrication techniques and hybrid dielectric-plasmonic designs to realize robust, high-Q BIC metasurfaces.

2.2.3 Applications

Based on the thesis's relevance and the former theory explanation on metasurface theory, we will review some research developments and detailed applications on high-performance metalens, integrated polarization devices, and high-Q BIC metasurface sensors in this section.

Optical metalens. Metalens is a kind of gradient metasurface that collectively focuses light. These devices can replicate traditional optical elements while offering novel functionalities. The emergence of metalens addresses the growing demand for functional and miniaturized optical systems, supported by advancements in standard planar nanofabrication protocols [*59*]. Metalens utilizes 0-2π phase modulation, resulting in multiple Fresnel zones through phase wrapping and producing focal spot distributions which is similar to traditional diffractive lenses. However, the key advantage of metalens over diffractive lenses lies in their potential to achieve

achromatic characterization, multiple foci, and large numerical apertures (NAs). High-efficiency, high-NA metalenses have been demonstrated using high-contrast transmit arrays [*40*], as shown in Figure 2-12a.

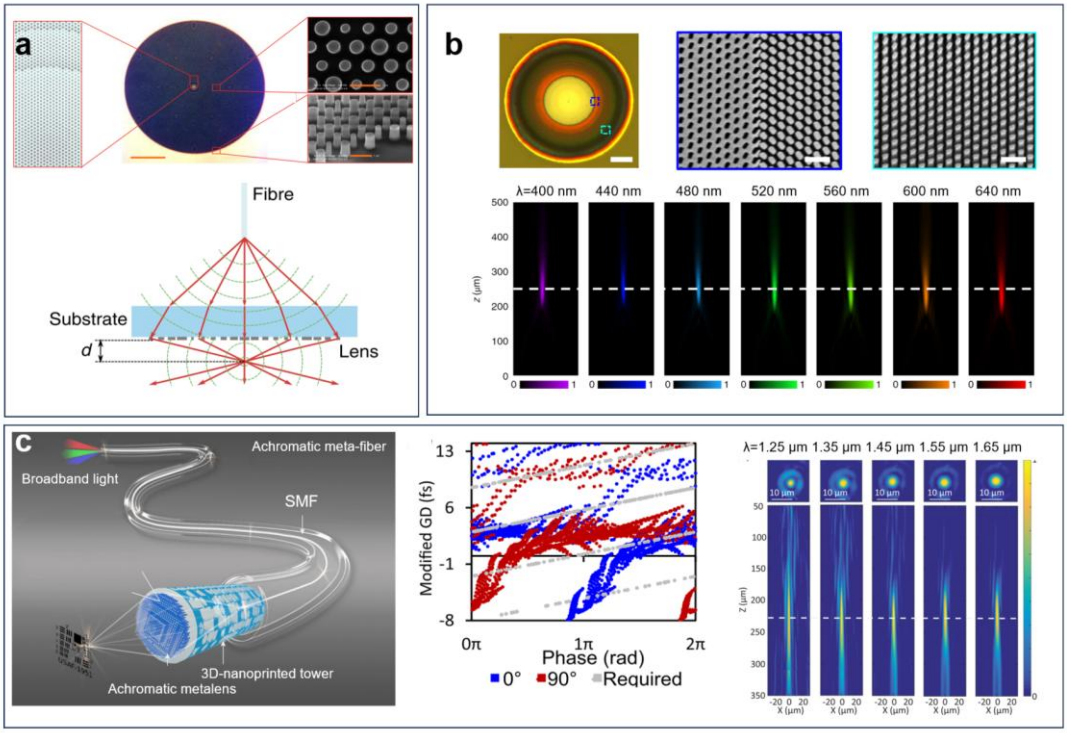

Figure 2-12 Large-NA metalens and achromatic metalens. (a) Efficient high-NA metalens with high height-to-width ratio meta-atoms [*54*]. **(b)** A broadband achromatic metalens in the visible by compensation of phase delays [*60*]. **(c)** An achromatic fiber metalens fabricated by 3D direct laser writing [*21*].

The chromatic aberration inherent in conventional lenses, induced by multi-wavelength optical path differences, can be addressed via metasurfaces through strategically engineered group delays in meta-atoms [*60-63*]. However, a key limitation of this approach lies in the requirement for meta-atoms with large group delay variations and the fabrication challenges associated with high height-to-width ratio nanostructures. Advancements in 3D nano-printing have promoted achromatic fiber-integrated metalenses manufactured via 3D direct writing technology, operating across 1.25–1.65 μm wavelengths [*21*]. Figures 2-12b and c demonstrate an achromatic

metalens in the visible spectrum across 400–640 nm and a fiber-integrated achromatic metalens in the C-band for optical communications.

Metalenses also function as multiplexers for SMF-to-MMF coupling, potentially enabling high-speed communications, as shown in Figure 2-13 [*64*]. Owing to their compact architecture, metalenses enable practical applications such as endoscopic and microscopic systems [*65, 66*].

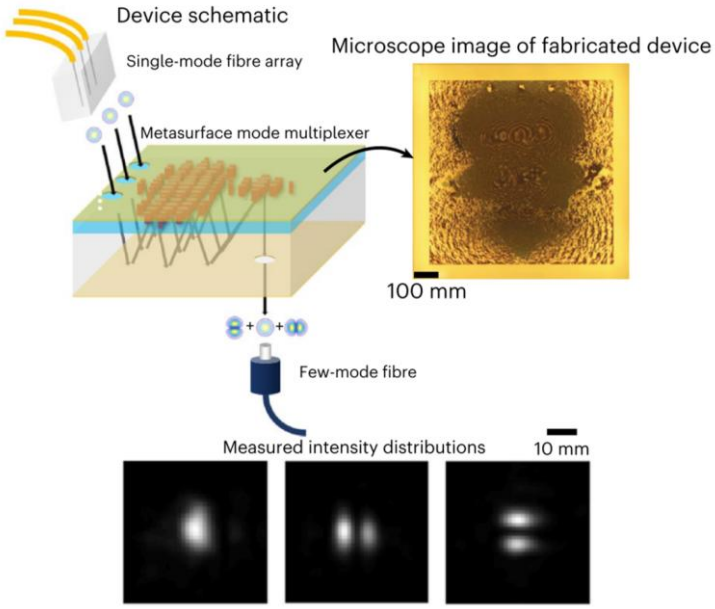

Figure 2-13 Multifunctional applications of metalens. A compact metasurface multiplexer for single-mode fiber to few-mode fiber connection [*64*].

Polarization devices. Metasurfaces exhibit intrinsic polarization modulation capabilities through their phase modulation mechanisms via meta-atoms, as the gradient phase modulation methods detailed in Section 2.2.2. The use of anisotropic meta-atoms (*e.g.*, nano-bricks and nano-ellipsoids) enables expanded phase delay control but introduces inherent polarization selectivity. Conversely, the geometric phase approach achieves full 0–2π phase coverage through meta-atom rotation, yet delivers opposing phase responses for LCP and RCP. Notable applications leveraging these polarization-manipulation properties include chiral imaging [*67*], polarimeter [*68*], full-

Stokes polarization camera [*69, 70*], and related systems. Figure 2-14 demonstrates a novel self-coherent receiver architecture comprising an interleaved metasurface integrated with a photodetector array. The system was engineered to generate six discrete focal points exhibiting distinct polarization states, enabling comprehensive full-Stokes parameter detection. Experimental validation was conducted through 20-GBd 16-ary quadrature amplitude modulation (16-QAM) and 50-GBd quadrature phase-shift keying (QPSK) signal transmission over a 25-km SMF link [*71*].

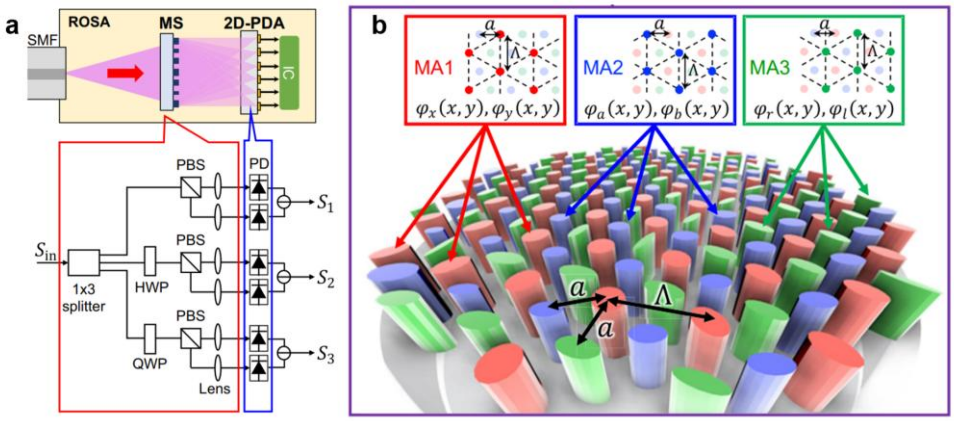

Figure 2-14 Metasurface-based polarization devices. An interleaved multi-foci metalens as a self-coherent receiver for a high-speed all-fiber self-coherent communication system[*71*].

BIC-based sensors. BICs theoretically exhibit infinite *Q*-factors through destructive interference of radiation channels, making them ideal platforms for enhancing light-matter interactions. With its exceptional *Q*-factor and localized field enhancement, the concept of BICs boosts the optical sensing area [*72-75*]. Figure 2-15 demonstrates on BIC metasurface in a microfluidic chamber for a high-*Q* molecules sensor, and a BIC-enhanced fluorescence imager. Early implementations of BICs predominantly relied on plasmonic metasurfaces due to their strong field confinement at subwavelength scales [*76*]. However, the intrinsic ohmic losses of metallic nanostructures severely limit their practical *Q*-factors.

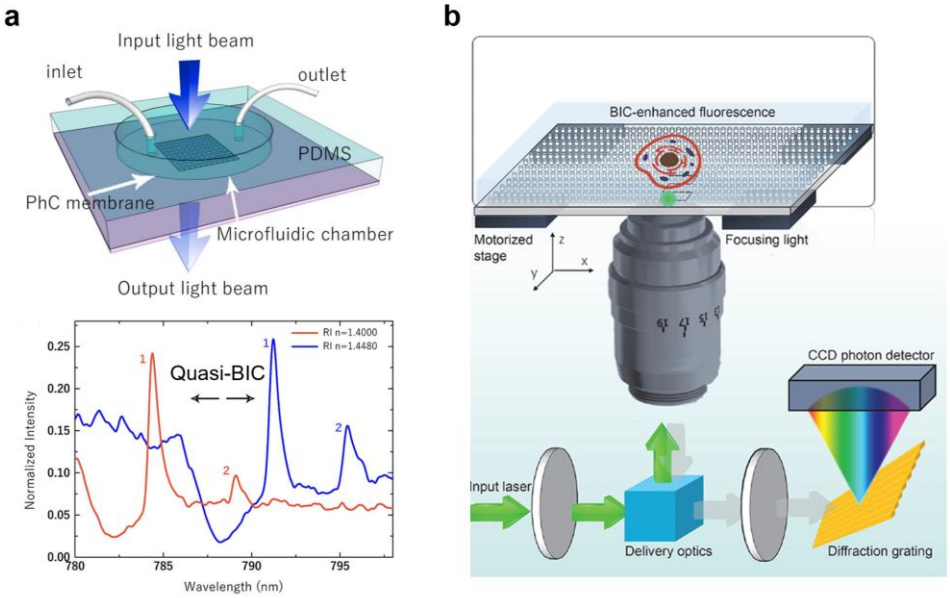

Figure 2-15 BIC-based sensors. (a) A label-free BICs sensor for ultralow-weight molecules. The sensor possesses a *Q*-factor of about 2000 and a figure of merit of 455 [*72*]. **(b)** Cavity-enhanced hyperspectral refractometric imaging using quasi-BIC modes in an all-dielectric photonic crystal slab [*73*]

Recently, most research on BICs relies on dielectric metasurfaces. In a dielectric metasurface, high *Q* is easily attained by tuning the asymmetric ratio [*77*], but the high RI of dielectric materials makes the electric magnetic wave confined inside the meta-atoms, which makes dielectric metasurfaces less sensitive to the outer environment. The hybrid metal-dielectric metasurface has been proven to obtain both high *Q* and high sensitivity [*78, 79*]. Key challenges in BIC metasurfaces include their stringent fabrication precision requirements, where slight deviations in asymmetric ratios can lead to significant reductions in *Q*-factor. Furthermore, most BIC metasurfaces operate only under fixed polarization states or precise incident angles, which limits their adaptability in practical scenarios.

2.3 Graphene: Tunable Mechanism and Applications

2.3.1 Basic properties

Graphene, as a prototypical 2D material with atomic-scale thickness, has revolutionized photonic and optoelectronic device engineering [*80*] through its unique combination of ultra-broadband optical response (spanning visible to terahertz frequencies) and electrically tunable conductivity as shown in Figure 2-16 [*81*]. These exceptional properties originate from graphene's relativistic charge carrier dynamics, where massless Dirac fermions exhibit linear energy-momentum dispersion ($E = \hbar v_F |k|$) with Fermi velocity $v_F \approx 1 \times 10^6$ m/s [*82*]. Unlike conventional semiconductors, graphene's zero bandgap nature enables efficient inter-band transitions across a wide spectral range, facilitating rapid carrier excitation through optical, thermal, or electrical stimuli [*83*]. This distinctive electronic structure provides unparalleled capabilities for dynamically modulating light-matter interactions via external fields, making graphene particularly suitable for high-speed electro-optic modulators, broadband photodetectors, and tunable metasurfaces [*84*]. These attributes position graphene as a cornerstone for next-generation adaptive optics and integrated photonic circuits.

The ambipolar field-effect characteristics, inherent to graphene's Dirac fermion behavior, enable continuous tuning of both carrier polarity (electron/hole) and density, corresponding to Fermi level shifts up to 2 eV [*85*]. This electrical control mechanism allows real-time reconfiguration of optical parameters (phase, amplitude, polarization) in integrated photonic systems, positioning graphene as a critical enabler for adaptive optical components and programmable photonic integrated circuits.

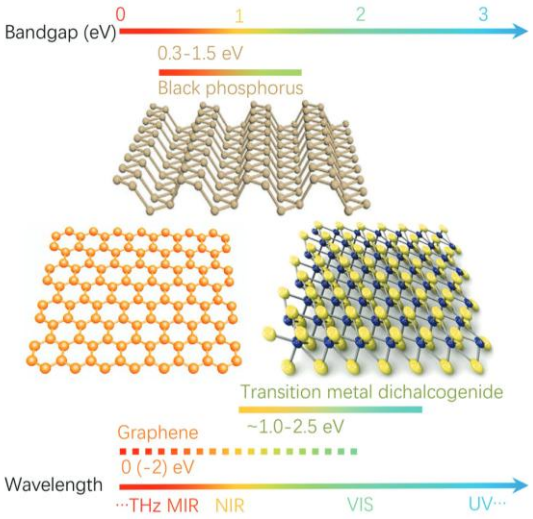

Figure 2-16 Electronic band gaps of typical 2D materials. Single-layer graphene exhibits semi-metallic behavior with a tunable Fermi level ($\Delta E_F \leqslant 2$ eV), enabling optical response modulation from terahertz to visible wavelengths. Transition metal dichalcogenides (TMDCs) demonstrate layer-dependent band gaps (1.0–2.5 eV). Black phosphorus (BP) shows anisotropic layer-tunable band gaps (0.5–1.0 eV) with preserved direct gap characteristics [*81*].

Graphene's atomic-scale confinement and van der Waals integration capability provide fundamental advantages for integrated photonic applications [*86*],

(1) Thickness-engineered band structure. The absence of interlayer coupling in monolayer graphene preserves its linear dispersion, while few-layer configurations enable controlled interlayer screening effects.

(2) Enhanced light-matter interaction. Sub-wavelength optical field confinement at graphene-dielectric interfaces boosts nonlinear optical coefficients and absorption efficiency (2.3% per layer).

(3) Mechanical adaptability. Intrinsic flexibility and self-passivated surfaces permit direct integration with silicon photonics and optical fibers through van der Waals heterostructure.

Furthermore, the synergy between graphene's electronic and optical properties enables multimodal tuning via electrostatic gating, optical pumping, or thermal

excitation. This multi-physical addressability has inspired novel device architectures including non-volatile photonic memories, wavelength-agile meta-lenses, and bio-integrated optoelectronic sensors [*87*]. Figure 2-17 illustrates the three primary modulation approaches for 2D materials categorized by their response time characteristics. The thermal modulation method exhibits the slowest operational speed, typically in the millisecond (ms) to microsecond range (μs). In contrast, electrical modulation demonstrates significantly faster performance with modulation speeds reaching the nanosecond (ns) timescale. The optical modulation approach achieves the ultimate temporal resolution, capable of attaining femtosecond (fs) level modulation rates. Among these techniques, electrical gating-based modulation has attracted the most extensive research attention due to its balanced performance and practical applicability.

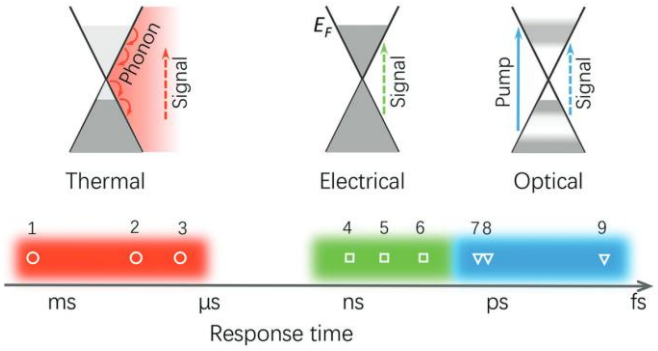

Figure 2-17 Schematic of 2D material inter-band modulation based on thermal, electrical, and optical-pumped methods. The response times of different methods are illustrated with different colors [*81*].

2.3.2 Tunable mechanism of graphene

Monolayer graphene, a quantum material characterized by its unique two-dimensional honeycomb lattice structure, exhibits exceptional optoelectronic tunability owing to its

adjustable electronic band structure and distinctive Dirac cone features. Through external thermal-optic, electric-optic, or optical-pump mechanism, researchers can precisely modulate graphene's Fermi level and carrier density, enabling dynamic control of its optical response. This remarkable adaptability positions graphene as a prime candidate for developing reconfigurable photonic devices and tunable metasurfaces.

The surface optical conductivity serves as the fundamental parameter governing graphene's light-matter interactions, encapsulating both the electromagnetic coupling efficiency and quantum-mechanical anisotropy inherent to this Dirac fermion system. In theoretical frameworks, the atomic-scale thickness of graphene permits its representation as an idealized two-dimensional current sheet, where electromagnetic responses are fully described through surface current density formulations. Specifically, when aligned with the *x*-*z* coordinate system, graphene demonstrates anisotropic current density components along orthogonal directions, expressible as:

$$J_x = \sigma_g E_x, \text{ and } J_z = \sigma_g E_z \tag{2-12}$$

Where, σ_g is the surface conductivity of single-layer graphene, E_x and E_z are the electric field along *x* and *z* directions, respectively. The surface conductivity of graphene can be described by the Kubo Formula, which has a complex value and consists of inter-band and intra-band conductivities[*88*],

$$\sigma_{\text{intra}} = \frac{-ie^2 k_B T}{\pi\hbar^2(\omega - \mathrm{i}\Gamma)}\left[\frac{\mu_c}{k_B T} + 2\ln\left(\exp\left(\frac{-\mu_c}{k_B T}\right)+1\right)\right] \tag{2-13}$$

$$\sigma_{\text{inter}} = \frac{-ie^2(\omega - i\Gamma)}{\pi\hbar^2}\int_0^\infty \frac{f(-\xi) - f(\xi)}{(\omega - i\Gamma)^2 - (4\xi/\hbar)^2} d\xi \tag{2-14}$$

where, $e, \omega, \mu_c, k_B, T, \hbar, \Gamma$, and $f(\xi)$ represent the charge of the electron, angular frequency of light, chemical potential, Boltzmann constant, temperature, reduced Planck's constant, scattering rate, and Fermi-Dirac distribution function $f(\xi) = 1/\{1+\exp[(\xi-\mu_c)/k_BT]\}$, respectively. In the visible and infrared spectra where $\hbar\omega > 2|\mu_c|$, the inter-band transition dominates, and the graphene's optical conductivity approaches $\sigma_0 \approx e^2/4\hbar$, corresponding to a universal optical absorption of approximately 2.3% per monolayer [*89*]. For simulations, the temperature is fixed at T = 300 K, and the scattering parameter is set as $\hbar\Gamma = 5$ meV. The total surface conductivity of graphene is derived from the sum of intra-band and inter-band contributions $\sigma_g = \sigma_{\text{intra}} + \sigma_{\text{inter}}$. As illustrated in Figure 2-18, the surface conductivity of graphene σ_g at $\lambda = 1.33$ μm exhibits a strong dependence on the chemical potential μ_c. This tunability enables electrostatic modulation of graphene's optical properties via an external gate voltage, providing a pathway for designing dynamically reconfigurable optoelectronic devices, such as tunable absorbers, modulators, and metasurfaces.

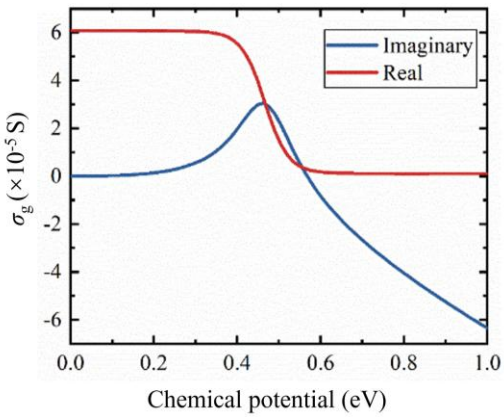

Figure 2-18 Surface conductivity of graphene versus chemical potential at 1.33 μm

2.3.3 Graphene-based fiber devices

This section systematically examines the integration techniques for combining graphene with optical fiber platforms. As previously discussed in Section 2.3.2,

graphene's mechanical robustness makes it particularly compatible with optical fiber substrates. The inherent geometric advantage of optical fibers, their exceptional length-to-radius ratio, provides an extended platform for achieving sufficient light-matter interaction strengths through evanescent field coupling.

While previous studies have explored fiber-tip integration configurations [*90, 91*], this approach suffers from fundamental limitations in light-matter interaction area due to geometric constraints. In contrast, waveguide-based integration strategies enable interaction intensities that scale with the two-dimensional material's propagation length along the waveguide axis, effectively circumventing limitations imposed by its atomic-scale thickness. Three principal waveguide coupling architectures have been demonstrated, as illustrated in Figure 2-19, the D-shaped fiber, the optical micro fiber (MF) directly on and wrapped on graphene substrates [*92*].

The D-shaped fiber configuration (Figure 2-19a) employs side-polishing or chemical etching techniques to expose the fiber core and enhance surface evanescent fields [*19, 93, 94*]. This planarized architecture facilitates superior interfacial contact with transferred two-dimensional materials while maintaining structural integrity. Although currently underexplored, D-shaped fibers functionalized with nanophotonic structures and advanced materials exhibit significant potential for all-fiber optical manipulation systems, combining enhanced performance with mechanical robustness.

Microfiber integration employs two primary configurations: line-contact Microfibers [*95*] (Figure 2-19b), and graphene-wrapped Microfibers [*96, 97*] (Figure 2-19c). Fabricated through thermal tapering or chemical etching of standard optical fibers, MFs typically demonstrate diameter reduction to subwavelength dimensions (hundreds of nanometers to tens of micrometers). While subwavelength MFs enable strong evanescent field interactions with 2D materials, their structural fragility presents

practical challenges. The fabrication and handling of submicron-diameter MFs remain technically demanding due to susceptibility to mechanical failure and environmental contamination.

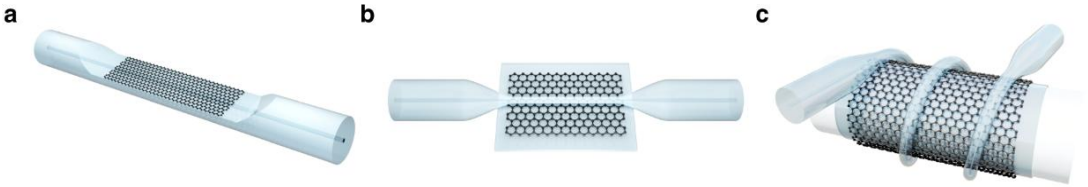

Figure 2-19 Graphene-fiber integration methods. (a) D-shaped fiber with graphene. **(b)** Micro-fiber-graphene structures on graphene-deposited substrate. **(c)** Micro-fiber wrapped on graphene substrate [*92*].

Graphene's exceptional electro-optic properties [*84*] have enabled transformative advances in fiber-integrated photonic devices. When integrated with D-shaped fibers, graphene creates a robust platform for high-efficiency tunable devices. Compared to fiber-tip configurations, D-shaped architectures provide lateral access to evanescent fields, offering dual advantages: enhanced light-matter interaction through increased effective overlap area, and reduced insertion loss through optimized modal matching. This combination of enhanced functionality and structural stability positions D-shaped graphene-fiber hybrids as particularly promising for practical photonic applications requiring both performance reliability and environmental resilience

In 2011, graphene was first used for broadband polarization filtering based on a D-shaped SMF [*19*]. To further improve the light-graphene interaction, a double D-shaped hole optical fiber coated with graphene was proposed [*98*]. By simulation, it was proven to achieve more efficient polarization filtering. Furthermore, different polymer-coated D-shaped-fiber graphene polarizers were proposed to enhance the light-matter interaction and applied to ultrashort pulse lasers and optical modulators [*94, 99*]. Although these filters are effective and have low insertion loss, the graphene-caused

attenuation is limited (< 18 dB/mm), which requires a relatively large light-graphene interaction length for a high extinction ratio. Meanwhile, the design is challenging to fabricate because the performance is closely tied to the core-graphene distances and the thickness of the polymer[*99*]. A recent work combined the polarization-dependent losses introduced by SPR modes with the electrically adjustable properties possessed by graphene to achieve tunable refractive index sensors based on PCFs [*100*]. However, the loss difference between the two orthogonal polarization states is not large enough to achieve a miniaturized and efficient tunable polarization filter.

Chapter 3 Plasmonic BIC Metasurface for Ultrasensitive Fiber Sensor

The physical mechanism of BICs has revolutionized optical sensing by enabling ultrahigh-Q factor resonances. Particularly, quasi-BIC-driven high-Q resonances in plasmonic nanostructures offer both ultra-strong field enhancement effects and exceptional sensitivity to nanoscale environmental perturbations. However, most high-Q quasi-BIC resonances require precise wavevector matching and angular alignment, making them difficult to be effectively excited with waveguide modes, which limits their development as integrated devices. In this work, to the best of our knowledge, we first employ a plasmonic metasurface with cross-shaped slots to construct high-Q flat-band quasi-BICs, which can well couple with the fundamental mode of an SMF. The designed fiber-tip-integrated metasurface demonstrates alignment-free reflective sensing capability. Experimental validation using 1-μL low-molecular-weight analytes reveals real-time RI tracking capability with >50% modulation depth and maximum sensitivity of 529.1 nm/RIU. In this section, we will present a comprehensive fabrication methodology for fiber-tip metasurfaces, including the design principles of flat-band quasi-BIC metasurfaces and their performance evaluation as RI fiber-tip sensors.

3.1 Introduction

Plasmonic nanostructures have enabled a wide range of applications owing to their unique capability to manipulate strong light-matter interactions at subwavelength scales via SPR [*101-103*]. Unlike dielectric resonators that localize fields within high-index nanoparticles [*104, 105*], plasmonic systems concentrate energy at metal-dielectric interfaces, exhibiting extreme sensitivity to local RI variations. These combined characteristics of environmental sensitivity and field enhancement have propelled plasmonic nanostructures, such as metasurfaces [*106*] and single nanoparticles [*107*], into critical roles in single-molecule spectroscopy [*108, 109*], viral detection [*110*], and catalytic reaction monitoring [*111*]. Recent advances based on the "lab-on-fiber" concept [*112*] have further extended their application to fiber-integrated sensors for in *vivo* environmental monitoring [*113*]. However, the *Q* of plasmonic resonances remains fundamentally constrained due to inherent dissipative and radiative losses, limiting progress in advanced plasmonic sensing systems.

The concept of BICs provides new opportunities for engineering ultrahigh-*Q* optical devices by perfect suppression of radiation loss [*42, 56, 76*]. Theoretically, ideal BICs decouple resonances from radiation channels by precise symmetry configurations, manifesting as nonradiative dark modes with infinite *Q* factors. In practical applications, intentional symmetry breaking is normally introduced to convert ideal BICs into quasi-BIC resonances that retain finite *Q* factors and are accessible with the far-field excitation. The quasi-BICs exhibit high *Q* and can be precisely tuned by controlling structural asymmetry. This feature has enabled dielectric quasi-BICs to showcase significant potential for various applications such as low-threshold lasers [*114, 115*], enhanced nonlinear effects [*116*], and high-resolution imaging and sensing [*73*]. For

plasmonic systems, recent studies have demonstrated that the *Q* factor of plasmonic quasi-BICs can reach 3,000 via a local-to-nonlocal transformation mechanism [*117*], wherein plasmon mode field expansion into the air reduces dissipative loss. Notably, achieving high-*Q* performance in most BIC-based devices demands not only nanoscale fabrication precision but also strict alignment requirements. Even minor deviations from optimal incidence conditions can cause significant *Q*-factor degradation [*118-120*]. Consequently, BIC-based devices are predominantly limited to bulky free-space optical systems. Developing compact, integrated platforms remains crucial for advancing practical implementations of BIC-enabled optical devices.

In this work, we demonstrate a fiber-integrated plasmonic cross-shaped slot metasurface (PCSM), supporting high-*Q* quasi-BIC in the NIR band. The engineered quasi-BIC exhibits flat-band angular dispersion characteristics, enabling efficient coupling with the fundamental fiber mode. In sensing demonstrations, the fiber-integrated PCSM demonstrates plug-and-play functionality with dual stable spectral signatures: a sharp quasi-BIC resonance and a broadband LSPR mode exhibiting modulation depth > 85%. The PCSM fiber sensor achieves remarkable RI sensitivity spanning 1-1.4732 RIU using 1-μL analytes, attaining a maximum sensitivity of 529.1 nm/RIU with real-time monitoring capability. Our findings establish a new paradigm for ultra-sensitive fiber sensors via plasmonic quasi-BICs, while providing a compact, fully fiber-integrated platform that bridges the gap between BIC device concepts and practical applications.

3.2 Theory and Numerical Design

Figure 3-1 illustrates the schematic configuration of the fiber-tip-integrated PCSM as a fiber sensor and details of a PCSM meta-atom. The PCSM comprises a periodic array

of asymmetric gold crosses fabricated on a 100-nm-thick gold layer, which is sufficient to ensure strong NIR reflectance. With optimized geometric parameters p = 700 nm (period), l = 500 nm (length), w = 100 nm (width), and t = 100 nm (thickness), the unit achieves controlled structural asymmetry through vertical length shifts δl. A broadband input signal $I_{in}(\lambda)$ coupled into the fiber core, generating environment-dependent reflected signals $I_r(\lambda)$ for label-free sensing. The fiber-integrated platform offers enhanced usability by eliminating the need for precise spatial light alignment, which is enabled by the intrinsic mode coupling between the SMF core and the PCSM. Unlike most previous studies on fiber-tip resonance, which directly transferred nanostructures from planar substrates to fiber tips, resulting in significant spectral broadening [*128*, *131*], our work systematically elucidates the origin of spectral broadening. In the following sections, we present a detailed discussion of the angular spectrum of the SMF, the local-to-nonlocal transition, and the flat-band quasi-BIC design. These analyses elucidate the mechanisms underlying the efficient coupling with the fundamental mode of the SMF and the high-Q realization of plasmonic quasi-BICs.

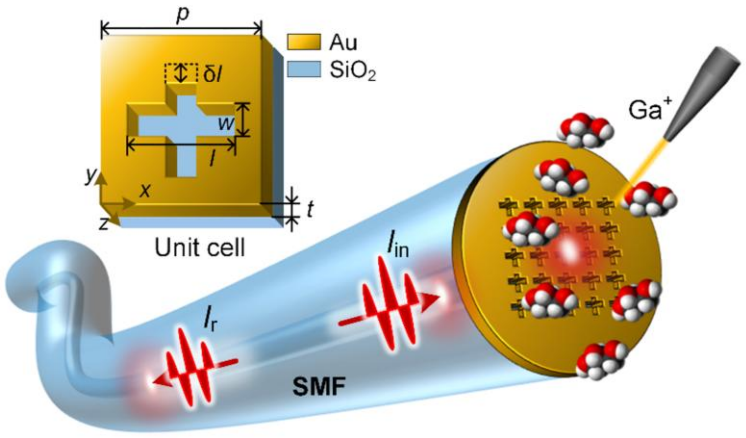

Figure 3-1 Schematic configuration of the fiber-tip integrated PCSM and the geometric details of a PCSM meta-atom.

3.2.1 Angular spectrum analysis of optical fiber

The angular spectrum of the SMF tip output is shown in Figure 3-2, calculated via the Fourier transform of the cross-sectional electric field distribution of the SMF tip (Figure 2-3).

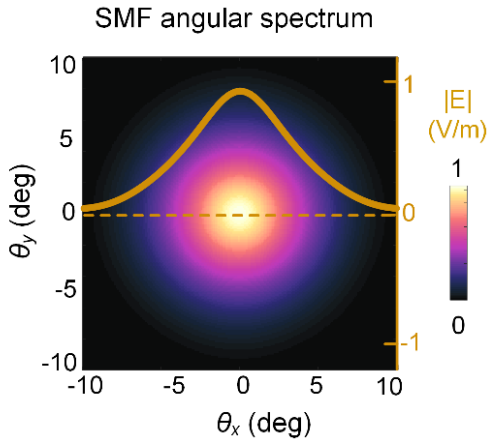

Figure 3-2 Angular spectrum of the SMF tip output light. The cross section at θ_y=0° is illustrated as an amber curve.

As discussed in Section 2.1.1, the output electric field from an SMF is a Gaussian-like beam with spatially varying wave vectors at different angles. To quantify these angular components, the output electric field $E(x,y)$ can be transformed into the spatial frequency domain using a two-dimensional Fast Fourier Transform (FFT) [*121*]. The resulting angular spectrum, shown in Figure 1b of the main text, is derived as:

$$A(f_x, f_y) = \iint_D E(x,y) e^{-i2\pi(f_x x + f_y y)} \mathrm{d}x\mathrm{d}y \tag{3-1}$$

where the integration domain D corresponds to the cladding region with diameter d=125μm. The spatial frequencies f_x and f_y are related to the cladding diameter d by $\Delta f_x = \Delta f_y = 1/d$, where Δf_x and Δf_y represent the frequency resolution. The wave vector components k_x and k_y in the fiber core are related to spatial frequencies by

$k_x = 2\pi f_x n_{\text{core}}$ and $k_y = 2\pi f_y n_{\text{core}}$, where n_{core} is the refractive index of the fiber core. The angles θ_x, θ_y of the wave vectors are determined from the k-space components using $\theta_{x/y} = \arcsin(\frac{k_{x/y}}{k})$, where $k = 2\pi n_{\text{core}} / \lambda$ is the total wave number in the fiber core. The far-field divergence angle is calculated as approximately 5.5° (Section 2.1.1). The wave vectors within a 5.5° angular range encompass the dominant electric field power, as observed in the k-space distribution (Figure 3-2). This analysis characterizes the distribution of wave vectors as a function of divergent angles at the fiber facet, providing a quantitative basis for evaluating the coupling efficiency between the resonator and the fiber's fundamental mode.

3.2.2 BICs mechanism and local-to-nonlocal transition

Simulation model. Figure 3-3a illustrates the model details, where a single meta-atom is simulated on a supporting quartz substrate, with analytes serving as the top dielectric environment. Floquet periodic boundary conditions are applied to the boundaries in the x and y directions. Two PMLs are implemented to absorb boundary effects at the top and bottom of the physical domain. A physics-controlled mesh with an extremely fine resolution was utilized, incorporating free tetrahedral meshes for the physical domain and swept mesh for the PML domain. Additionally, the Finite-Difference Time-Domain (FDTD) method was employed to validate the consistency of all simulations and results. To evaluate the sensor's minimum detectable volume, glycerin (refractive index RI = 1.473) was modeled at heights (h) ranging from 5 nm to 1 μm. As shown in Figure 3-3b, a wavelength shift of 12 nm was observed even at h = 5 nm, with the simulation mesh refined to 1 nm resolution. Taking the MFD of the fiber as reference, the

corresponding minimum detectable volume was estimated to be approximately 4×10^{-16} L for a 12-nm shift.

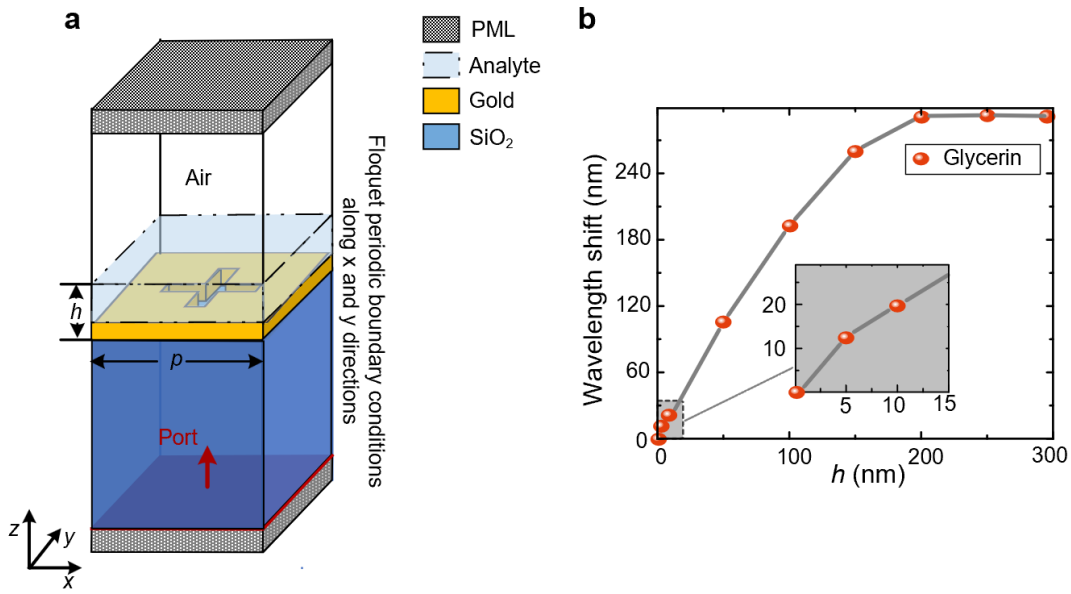

Figure 3-3 (a) Simulation model in COMSOL Multiphysics. **(b)** Wavelength shift of quasi-BIC mode with varying analysis height.

BIC mechanism and local-to-nonlocal transition. The designed PCSM supports two eigenmodes, including an SP-BIC point under normal incidence. Through mode analysis with varying δl, two distinct eigenmodes were identified in Figure 3-4. Notably, mode 1 (M_1) exhibits an infinite-Q BIC and an ultrahigh-Q (~10^4) mode when only considering radiation. In reality, the total Q factor (Q_{tot}) of the quasi-BIC incorporating radiation and dissipation can be defined as,

$$\frac{1}{Q_{tot}} = \frac{1}{Q_{rad}} + \frac{1}{Q_{dis}} \tag{3-2}$$

At asymmetric length δl = 0, the PCSM meta-atom maintains mirror symmetry, resulting in a fully symmetric electric field intensity distribution accompanied by opposite vector distributions (see the inset in Figure 3-4a). The symmetric confines energy within the meta-atom by preventing radiation leakage into the continuum, a

characteristic of SP-BIC. At this point, radiative loss vanishes, leaving Q_{tot} entirely governed by dissipative loss $Q_{tot} = Q_{dis} \approx 42$ (Figure 3-5).

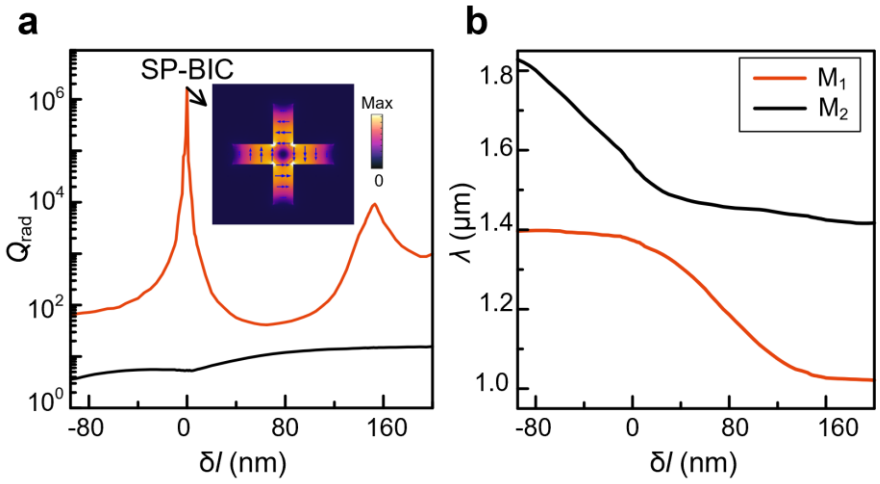

Figure 3-4 Radiative Q and resonant wavelength of the two eigenmodes supported by the PCSM as a function of asymmetric length δl. The insert displays the electric field distribution in the xy-plane (electric vectors indicated by double-headed arrows).

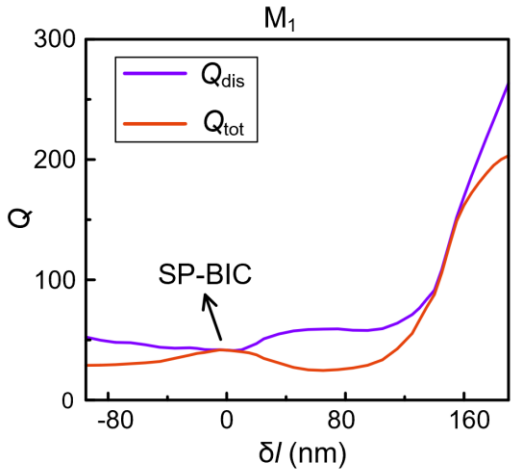

Figure 3-5 Total Q and dissipative Q of M1 versus δl.

Near the SP-BIC position, the increased radiation loss induced by growing δl causes a sharp decrease in Q_{rad}, which reaches its minimum at δl ~ 60 nm. As δl continues to increase, the Q_{rad} of the quasi-BIC begins to rebound and eventually attains a secondary maximum at δl ~ 152 nm. Concurrently, the resonant wavelength of M_1 blueshifts

monotonically with increasing δl (Figure 3-4b), approaching the diffraction order wavelength ($\lambda_D = p \times n_{SiO2} \approx 1.01$ μm, where p is the lattice period). During this process, the quasi-BIC progressively evolves from a local to a nonlocal resonance, which largely restrains the dissipative loss of plasmonic resonance (see Figure 3-5). Such a transition is critical for enhancing Q_{tot}, particularly in plasmonic metasurfaces where dissipative loss dominates.

Figure 3-6 visually demonstrates this transition: as the quasi-BIC approaches the lattice diffraction order, the mode volume expands, eventually forming a confined evanescent wave at the Au/SiO_2 interface. The secondary Q_{rad} maximum at δl ~150 nm arises from radiation suppression via coupling between the quasi-BIC and nonlocal diffraction modes during the local-to-nonlocal transition. It should be emphasized that the resonance at this secondary peak retains its quasi-BIC character of finitely high Q_{rad}, this behavior analogous to the evolution of supercavity mode observed in individual high-refractive-index dielectric particles [*122*].

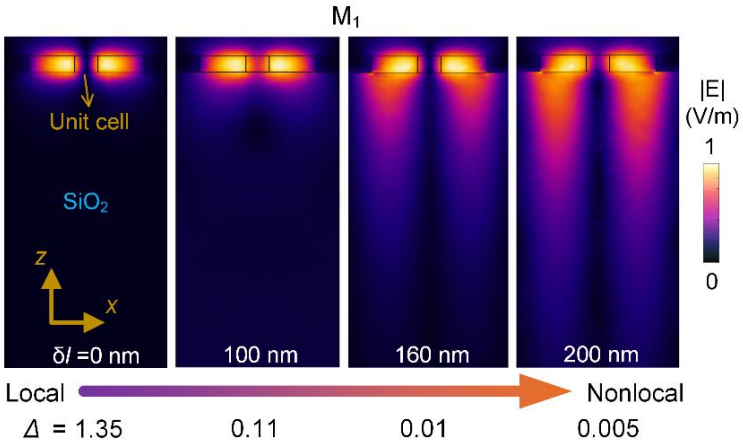

Figure 3-6 Electric field amplitude distribution in *yz*-plane for varying δl and related detuning parameter Δ.

Beyond δl > 60 nm, Q_{tot} increases steadily due to the growing Q_{dis} as the quasi-BIC approaches lattice resonance. To quantify this behavior, the normalized detuning parameter Δ is defined

$$\Delta = \frac{\lambda - \lambda_D}{\lambda_D} \tag{3-3}$$

As Δ decreases to zero, the quasi-BIC transitions fully from localized to nonlocal resonance. The relationship $Q_{dis} \propto 1/\sqrt{\Delta}$ (Figure 3-7) confirms an inverse square-root dependence, enabling quantitative assessment of the transition degree and Q enhancement. At $\Delta \sim 0.01$, the $Q_{tot} \approx Q_{dis} \approx 200$.

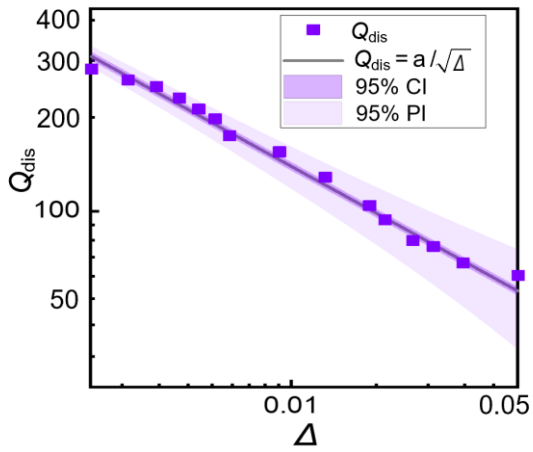

Figure 3-7 Inverse relationship between dissipative Q and the square root of Δ, plotted on a log-log scale with indicated 95% confidence interval (CI) and 95% prediction interval (PI).

Reflectance spectra and field enhancement. Subsequently, considering the dissipative loss, a parameter sweep is conducted for δl varying from -100 nm to 200 nm in increments of 2 nm, to derive the reflectance spectrum under XP light excitation, as depicted in Figure 3-8. The two primary modes identified in the reflectance spectrum exhibit resonant wavelengths that align effectively with the foregoing mode analysis.

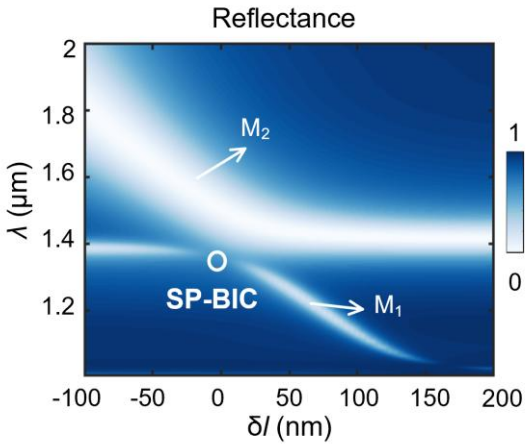

Figure 3-8 Simulated reflectance spectra of different δ*l* under XP incidence. The SP-BIC point is highlighted by a white circle.

Figure 3-9 illustrates the reflection spectra and electric field enhancement when the PCSM with δ*l* = 80 nm, respectively. The field enhancement coefficient is quantified by the expression $|E_{max}|^2 / |E_0|^2$, which is normalized by the incident electric field E_0, and E_{max} is the maximum electric field. It can be found that the field enhancement reaches peaks when the reflectance falls to the valleys. The resonance around λ = 1.18 μm is a quasi-BIC of M_1, and the resonance around λ = 1.42 μm is M_2, which manifests as an LSPR mode.

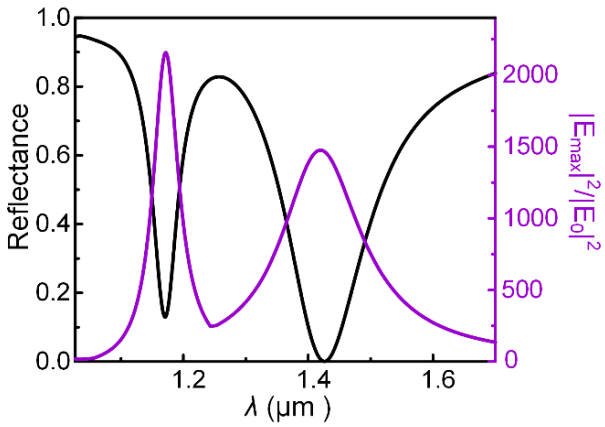

Figure 3-9 Field enhancement and reflectance at δ*l* = 80 nm.

Using the concept of energy density, we estimated the effective mode volume (V_{eff}) at the strongest point of the electric field. Energy density μ_E of electromagnetic can be used to calculate electromagnetic energy stored inside lossy materials [*123*],

$$\mu_E = \frac{\varepsilon_0}{2}(\varepsilon_1 + 2\omega\varepsilon_2\tau)|\mathbf{E}|^2 \tag{3-4}$$

where, ε_0 denotes Vacuum permittivity, $\varepsilon_1 + i\varepsilon_2$ is the complex dielectric function of a Drude model with relaxation time τ (for Au is around 9.3×10^{-15} s [*124*]). ω is the mode frequency. Selecting the point at the maximum electromagnetic field $\mathbf{r}_{\max}$ as the reference, the effective mode volume can be defined as [*125*],

$$V_{\text{eff}} = \frac{\int \mu_E(\mathbf{r})\,\mathrm{d}^3 r}{\mu_E(\mathbf{r}_{\max})} \tag{3-5}$$

The calculated results at M_1 and M_2 are $V_{\text{eff}} \approx 7.3\times10^{-4}\,\lambda^3$ and $5.6\times10^{-4}\,\lambda^3$, respectively, which present the designed meta-atom supports resonance with good mode confinement.

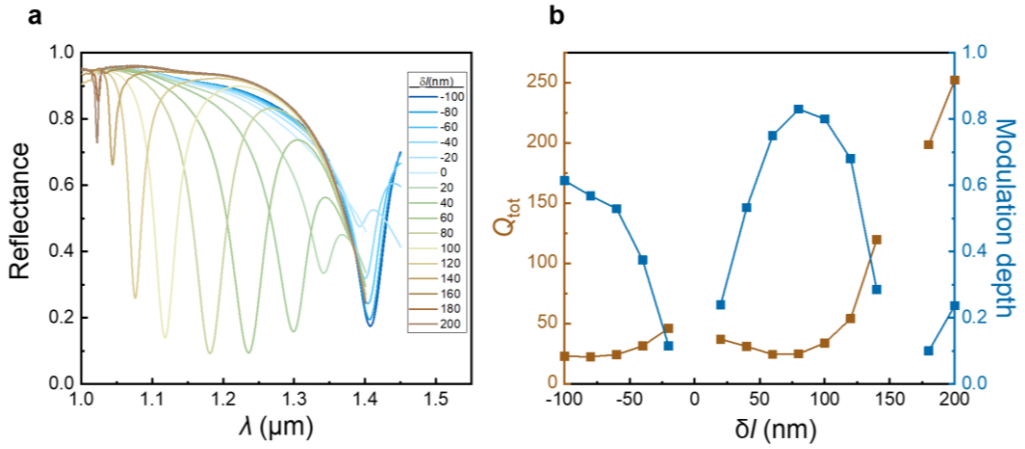

Figure 3-10 (a) Reflection spectra of M_1 for varying δl. **(b)** Extracted Q-factors and modulation depths as functions of δl, obtained from Lorentzian fitting of the spectra in **(a)**.

Tradeoff between *Q* and modulation depth. Figure 3-10(a) shows the reflection spectra of M_1 under XP vertical incidence. Using Lorentzian fitting with a quadratic

baseline, the calculated Q-factor ($Q = \lambda_r / \text{FWHM}$) and modulation depth (defined as the maximum amplitude of the Lorentzian peak) are plotted in Figure 3-10(b). Both Q-factors and modulation depths critically influence the stability and sensitivity of the fiber sensor. By optimizing these parameters, the PCSM with δl = 80 nm was selected for experimental validation.

3.2.3 Flat-band characterization

The flat-band characteristics of the designed PCSM with δl = 80 nm are analyzed under varying incident angles of XP illumination for both transverse electric (TE, *yz*-plane) and transverse magnetic (TM, *xz*-plane) modes, as shown in Figure 3-11.

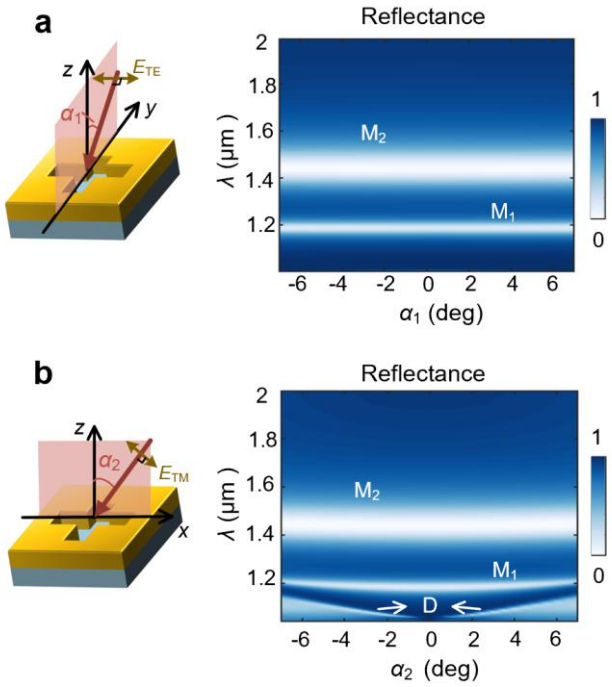

Figure 3-11 Theoretical flat-band characterization of the designed PCSM under XP incidence. **(a)** Reflection spectra along different incident angles α_1 at *yz* view. **(b)** Reflection spectra along different incident angles α_2 at *xz* view.

The angles between the incident XP light and the *z*-axis are defined as α_1 (TE mode) and α_2 (TM mode) for their respective configurations. Using Floquet periodic boundary

conditions along the *x*- and *y*-directions, we systematically varied α_1 and α_2 from −7° to +7° in 0.5° increments, covering most wave vectors within the divergent angle of 5.5°. Figures 3-11(a) and (b) illustrate the angular schematics and corresponding reflection spectra, while the extracted resonant wavelengths and *Q* factors of the quasi-BIC modes are shown in Figures 3-12(a) and (b), respectively.

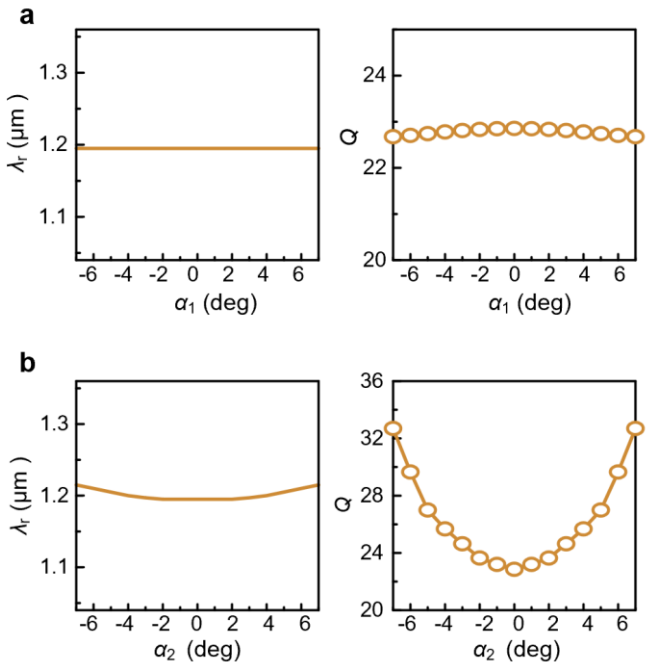

Figure 3-12 Dependence of quasi-BIC modes' resonant wavelength and *Q* factor on incidence (a) angles α1 and (b)angles α2.

The *Q* factor is calculated using the formula $Q = \lambda_{resonance} / \mathrm{FWHM}$, where FWHM is derived from Lorentzian curve fitting of the resonance peaks. Notably, variations in α_1 exhibit negligible influence on both the resonant wavelength and *Q* factor. In contrast, sweeping α_2 reveals emerging lattice diffraction modes (*D*) exhibiting significant angular dispersion, which arises from the increased polarization components in the *z*-direction at larger α_2. As α_2 deviates from 0°, the resonance wavelength of the lattice diffraction mode progressively approaches that of the quasi-BIC. This interaction induces minor wavelength fluctuations ($\Delta\lambda$ < 20 nm) in the quasi-BIC mode while

significantly enhancing its Q factor, which reaches values as high as ~33, thereby facilitating subsequent fiber integration.

To investigate the angular dispersion evolution during the local-to-nonlocal transition, reflectance versus incident angle was simulated for δl = -80 nm, -40 nm, 40 nm, and 80 nm. Figure 3-13 presents the results, systematically revealing the impact of δl on flat-band behavior. Both modes M_1 and M_2 exhibit ideal flat-band characteristics at δl = -80 nm, -40 nm, and 40 nm, evidenced by fixed resonant wavelength across angles from -7° to 7°.

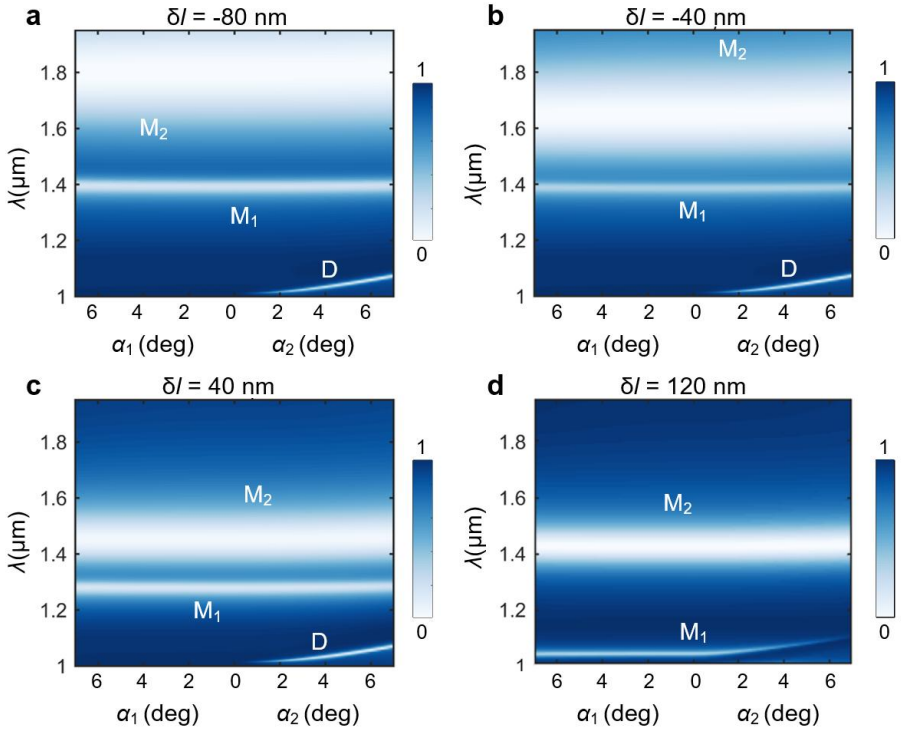

Figure 3-13 Reflectance spectra versus incident angle under varying asymmetric length (a) -80 nm, (b) -40 nm, (c) 40 nm, (d) 120 nm.

However, as δl increases beyond 40 nm, M_1 undergoes a distinct transition from a localized to a nonlocal resonance state. At the design point (δl = 80 nm), M_1 begins to interact with the diffraction order, resulting in a slight resonance wavelength shift ($\Delta\lambda$ < 20 nm) and an increase in Q-factor. Further increasing δl to 120 nm drives M_1 deeper into the nonlocal regime, causing pronounced angular dispersion: the resonance

wavelength shifts by $\Delta\lambda \approx 70$ nm across the evaluated angular range. This progressive emergence of dispersion with increasing δl directly demonstrates the transition from localized (flat-band) to nonlocal (dispersive) behavior.

3.3 Fabrication Flow and Details

3.3.1 Fabrication flow

Figure 3-14 illustrates the fabrication flow for fiber-integrated metasurface, comprising a multi-stage process optimized for structural precision and operational robustness. Initial protective preprocessing begins with stripping a 2-cm polymer coating segment from one terminus of the single-mode fiber, followed by encapsulation within a borosilicate glass capillary sleeve (dimensions: 6.5 ± 0.5 mm length, 1.8 ± 0.005 mm diameter). The assembly undergoes fixation using 353ND epoxy resin complemented by a protective gel coating to ensure mechanical stability. The detailed casing parameters are shown in Figure 3-15. Subsequent mechanical polishing employs an Aka-Piatto fine-grinding system to achieve surface planarization. Critical material deposition stages follow: a 25 ± 2 nm Al_2O_3 adhesion layer and a 100 ± 5 nm Au film are sequentially applied via magnetron sputtering under controlled vacuum conditions. Precise spatial registration is achieved at 350× SEM magnification through cladding edge alignment, enabling sub-10 nm accuracy in FIB milling (Thermo Scientific Heilos 5 CX Dual-Beam FIB-SEM, 30 kV acceleration voltage, 40 pA beam current) for metasurface patterning. This optimized fabrication workflow employs simple and robust steps to fabricate fiber-integrated metasurfaces. Furthermore, the proposed flow can be extended to create dielectric metasurfaces on a fiber tip.

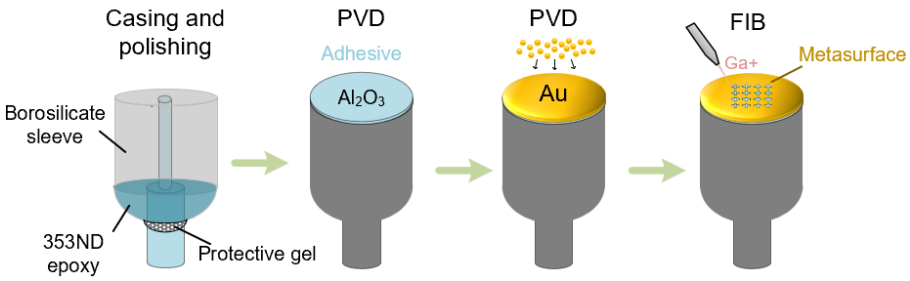

Figure 3-14 Fabrication flow of fiber-tip-integrated metasurface.

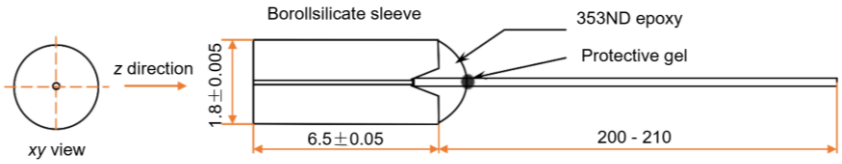

Figure 3-15 Detailed parameters of casing parameters of meta-fiber, in mm-unit.

3.3.2 Fabrication parameters

Unlike planar substrate nanofabrication, precise alignment to the fiber core constitutes a critical prerequisite in meta-fiber fabrication. To locate the fiber core, we align a 125-μm circle with the cladding edge using SEM imaging, thereby confirming the circle center. This center coincides with the 9-μm core center. Subsequently, the etching mask pattern is positioned over the fiber core. To validate this alignment methodology, Figure 3-16 presents microscopic characterization of an etched SMF with a 15.4 μm × 15.4 μm patterned region. Verification of spatial congruence between the etched area and the optical core was achieved by fusion-splicing the meta-fiber sample to a laser-coupled fiber patch cord ($\lambda = 650$ nm), enabling direct visualization of guided light confinement. Quantitative analysis confirmed complete overlap (<1 μm misalignment) between the etched microstructure and the core region. The subsequent fabrication steps rigorously adhered to this alignment protocol.

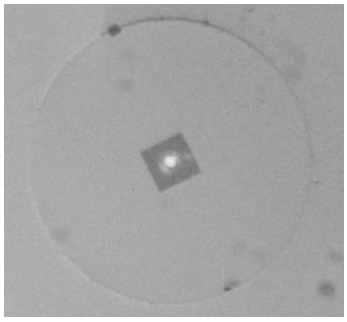

Figure 3-16 Deterministic alignment of the etching area (15.4 μm × 15.4 μm) and the fiber core under microscope view. The fiber is connected with a red laser for exhibiting the core position.

The fiber sample with a 20-cm tail segment was wrapped on a custom-designed sample holder (height: 16 mm) for FIB nanofabrication using a Thermo Scientific Helios 5 CX Dual-Beam FIB-SEM system. The system can achieve a resolution of 4.0 nm at 30 kV, as determined by standard statistical characterization methods. Prior to patterning, spatial alignment of the electron beam (E-beam) and ion beam (I-beam) imaging systems was performed using established calibration protocols. The fiber core was localized via E-beam imaging at 5 kV and 43 pA, followed by the application of a prepared pattern mask figure over the target region. Gold-specific sputtering parameters (preloaded in the system's material database) were implemented with the I-beam operating at 30 kV and 40 pA. The beam current remained fixed throughout the process, while the dwell time and etching depth were dynamically coupled based on the selected material parameters within the system. Both the dwell time and etching depth can be adjusted for better pattern etching precision, as illustrated in Figure 3-17. With increasing etching depth, the unpenetrated parts have decreased.

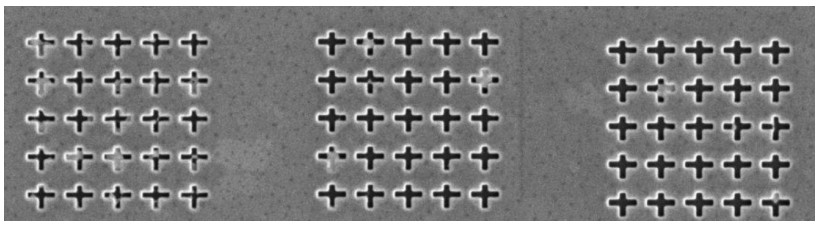

Figure 3-17 Etching performance of depths varying from 0.1 μm to 0.2 μm under SEM view.

3.3.3 Fabrication robustness

Fabrication errors for width w, length l, and asymmetric length δl parameters are below 5 nm (Figure 3-18). At the cross-slot intersection, measured corner widths reach 122 nm due to ion beam overlap artifacts. To evaluate spectral sensitivity to fabrication errors, we performed electromagnetic simulations using the model in Figure 3-3 (a) Simulation model in COMSOL **Multiphysics.** (b) Wavelength shift of quasi-BIC mode with varying analysis height. with 3 nm mesh resolution.

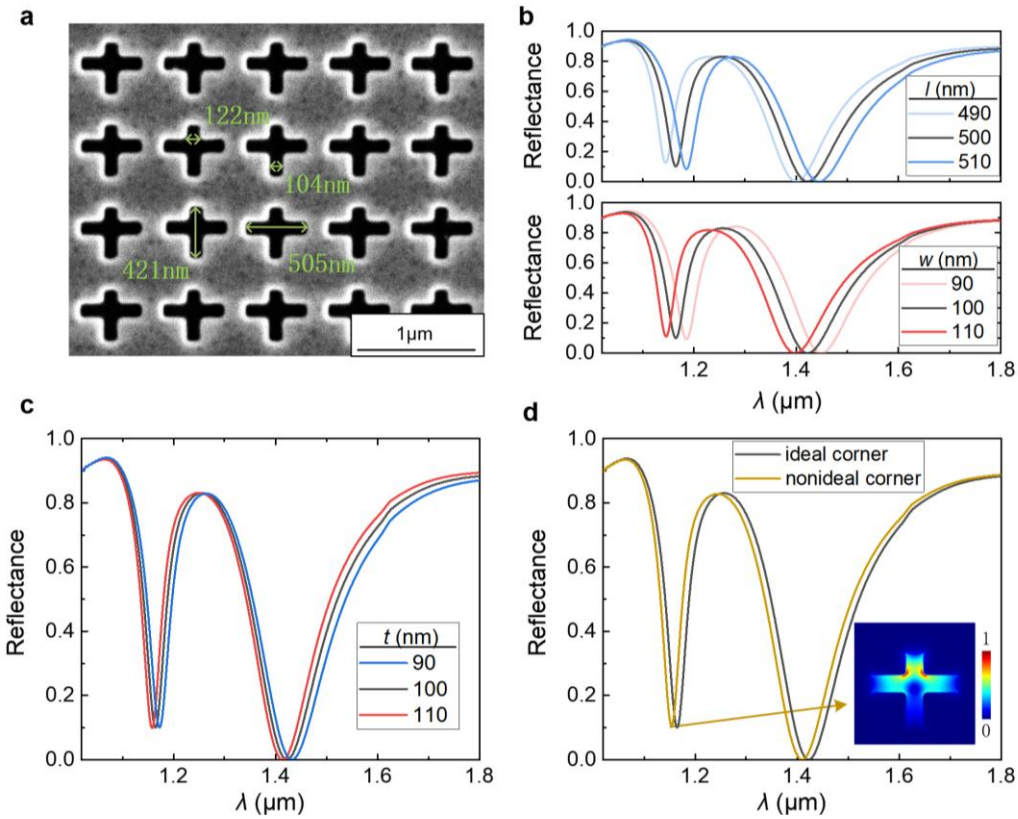

Figure 3-18 (a) Fabrication results with measured parameters. **(b,c)** Reflectance spectra showing 10 nm parametric variations in l, w, and t around design values. **(d)** Comparison of reflectance spectra: ideal vs. non-ideal corner model. Inset: Electric field distribution at λ = 1.155 μm for non-ideal case.

We parametrically varied unit parameter w, l, and t in 10 nm increments around ideal design values. Simulation results (Figure 3-18c) show thickness variations (±10 nm)

with ΔFWHM ≈ 0 nm, $\Delta\lambda \approx \pm 8$ nm and *l*/*w* variations (±10 nm): ΔFWHM ≈ ±5 nm, $\Delta\lambda \approx \pm 20$ nm. We modeled corner rounding effects by adding isosceles right triangles (leg length = 15 nm) at cross-junctions. Comparative simulations of ideal right-angle and non-ideal rounded corners (Figure 3-18d) reveal minimal impact: ΔFWHM ≈ 0 nm and $\Delta\lambda \approx 10$ nm. The inset shows the electric field distribution at the quasi-BIC mode for the non-ideal case. Given our experimental fabrication errors ≤ 5 nm, the device demonstrates high robustness with negligible *Q*-factor degradation and wavelength shifts ≤ 20 nm.

3.4 Experimental Results

The fabricated PCSM fiber device exhibits a compact structure with a diameter of approximately 1.8 mm. To accommodate the MFD of ~10.2 μm in the SMF (see Figure 2-5), the total etched area is designed as 24 μm × 15 μm. Detailed scanning electron microscopy (SEM) images in Figure 3-19b reveal the PCSM unit's periodic structure (700 nm periodicity) with critical dimensions: 500 nm leg length, 100 nm width, and 80 nm asymmetric feature length. The 80-nm asymmetry was selected to balance the trade-off between the quality factor (*Q*-factor) and modulation depth. Fabrication precision was maintained below 10 nm throughout the process.

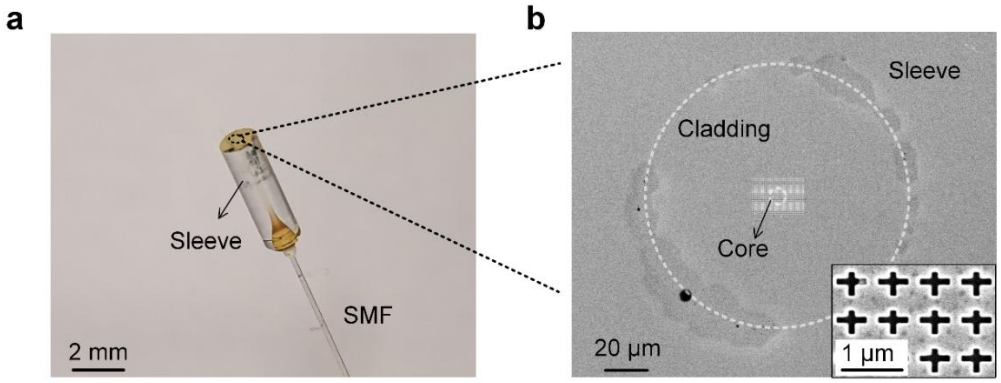

Figure 3-19 (a) The side view of the fiber-tip-integrated PCSM. **(b)** SEM image of the sample. The bottom of the image shows enlarged views of the etched PCSM.

A sensing experiment was conducted to detect the reflection spectrum of analytes. As depicted in Figure 3-20, the experimental configuration employed a supercontinuum laser (YSL Photonics SC-5) generating broadband output (0.45–2.4 μm). The emitted beam was first polarized using a FiberBench-mounted linear polarizer (LP, Thorlabs FBR-LPNIR) to selectively propagate either XP or YP states. The polarized light was then directed through a 50/50 fiber coupler (Thorlabs TD1315R5A1) to excite resonance in the fiber-integrated PCSM. This fiber-integrated PCSM features plug-in and plug-out functionality for convenient installation and removal. The reflectance spectra containing analyte-specific information were routed back through the same coupler and captured by an optical spectrum analyzer (OSA, Yokogawa AQ6370D).

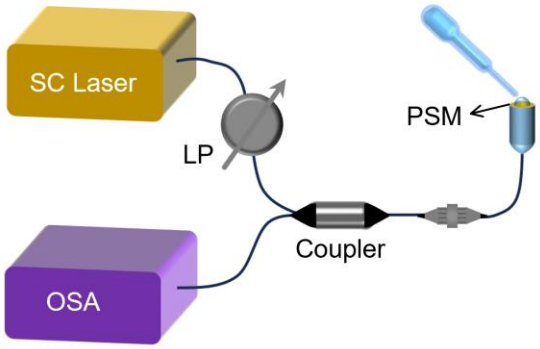

Figure 3-19 Sensing experiment set up, where LP stands for linear polarizer.

Initially, an optical fiber coated with an unetched gold layer was employed to acquire the background reflection spectrum, enabling normalization of the following measurements. Subsequently, the proposed quasi-BIC-based fiber sensor was installed in the optical path, and the corresponding reflection spectra in the air environment were recorded under XP and YP incidence, as shown in Figure 3-21. The reflection spectra were normalized and processed using a smoothing algorithm to mitigate interference noise originating from the optical pathway. Consistent with the simulation results, the

M_1 is exclusively observed under XP incidence, whereas M_2 appears in both polarization states. The reflectance spectra were fitted by Lorentz curves, and the relative FWHMs were extracted. The *Q*-factor of the M_1 was determined to be approximately 30, aligning well with the simulation under varying incident angles (Figure 3-12). Additionally, the quasi-BIC resonance exhibited a modulation depth of 0.44.

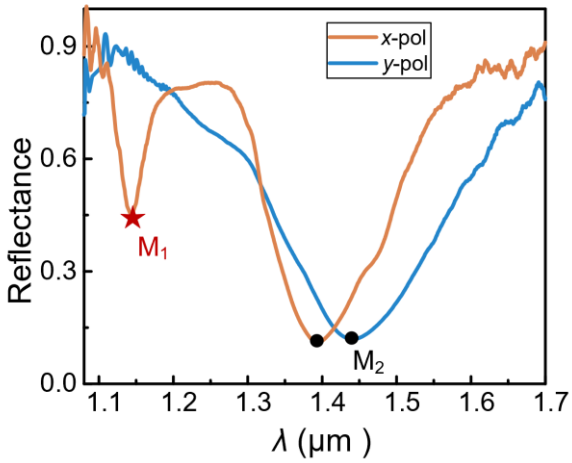

Figure 3-20 Reflectance under XP and YP incidence with the designed PCSM explored in the air.

In sequence, around 1-μL analytes with different RIs are placed on the end face of the optical fiber sensor utilizing a micropipette. The analyte consists of a mixture of deionized water (DI water) and glycerin (Gly) in varying proportions, resulting in distinct RIs measured using an Abbe refractometer. The refractometer has an accuracy of 2×10^{-4} RIU. Figures 3-22(a) and (b) show the reflection spectra of quasi-BIC M_1 and M_2, separately, with RIs ranging from 1 to 1.4752. By extracting the resonant wavelengths of M_1 and M_2, their linear relationships with different RIs are presented in Figures 3-22 (c) and (d). Among the same bandwidth of 300 nm, M_1 as a quasi-BIC mode shows sharp resonance with a sensitivity of 346.4 nm/RIU and a good linear fitting of resonant wavelength versus different RIs. M_2 as an LSPR shows a detection sensitivity of 529.1 nm/RIU. These two modes can be utilized in conjunction to measure

the RI, thereby enhancing the combination performance as a sensor. Additionally, they are expected to support dual-parameter sensing applications, allowing for the concurrent measurement of temperature and refractive index.

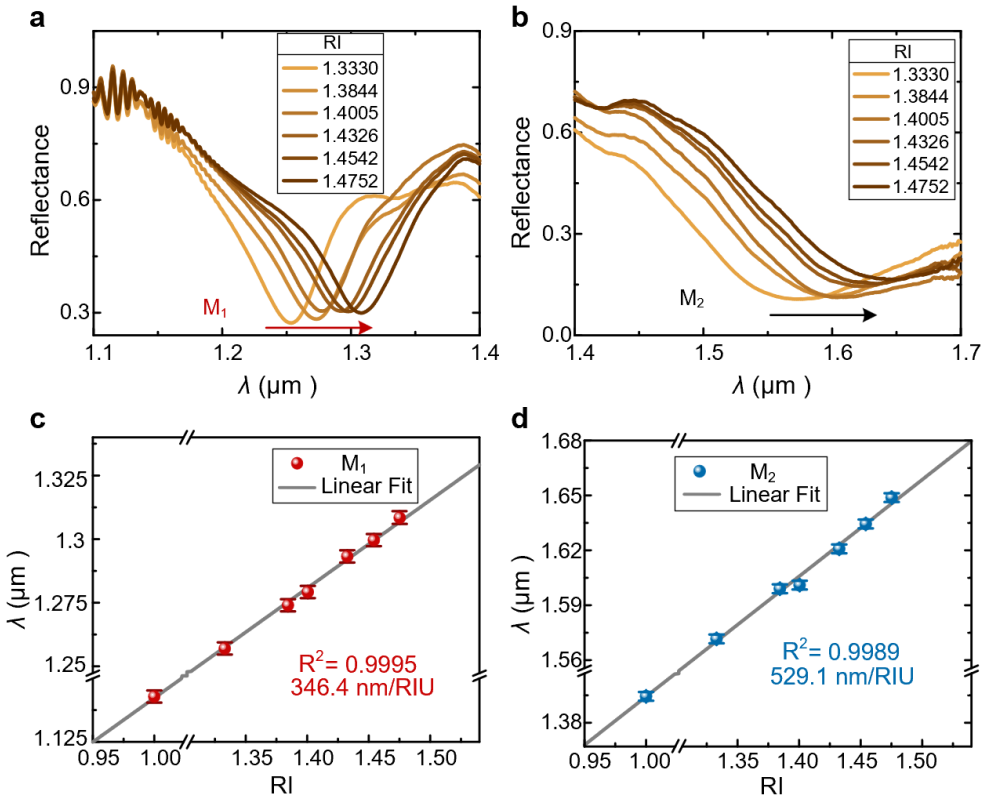

Figure 3-21 Experimental reflection spectra for different RIs corresponding to (a) M_1 and **(b)** M_2. Linear relationships between resonance wavelengths and RIs are shown for **(c)** M_1 and **(d)** M_2, with the coefficient of determination (R2) quantifying the fitting accuracy. Error bars reflect the spectrometer's 0.4 nm spectral resolution.

Real-time sensing experiments. The proposed BIC-based fiber sensor demonstrates a significant sensitivity to real-time fluctuations in RI. Considering that the narrow spectrum of M_1 can effectively reduce the detection bandwidth. In the conducted real-time experiments, the spectrometer's detection bandwidth is set to 250 nm, and the time resolution is approximately 0.5 seconds. Despite this relatively short duration, the sensor is capable of promptly detecting different RIs with wavelength shifts. The results of the real-time RI sensing are illustrated in Figure 3-23. During the assessment of the

resonant wavelength of the M_1, DI water and a Gly and DI water mixture with incrementally increasing concentrations are systematically dropped to the fiber sensor. The experimental results indicate that the wavelength shift occurs immediately upon the introduction of analytes with differing RIs. Considering the best resolution of the spectrometer of R=0.02 nm, the limit of detection (LOD) of the sensor can be estimated to be LOD = 3×R/sensitivity ≈ 1.7×10^{-4} RIU.

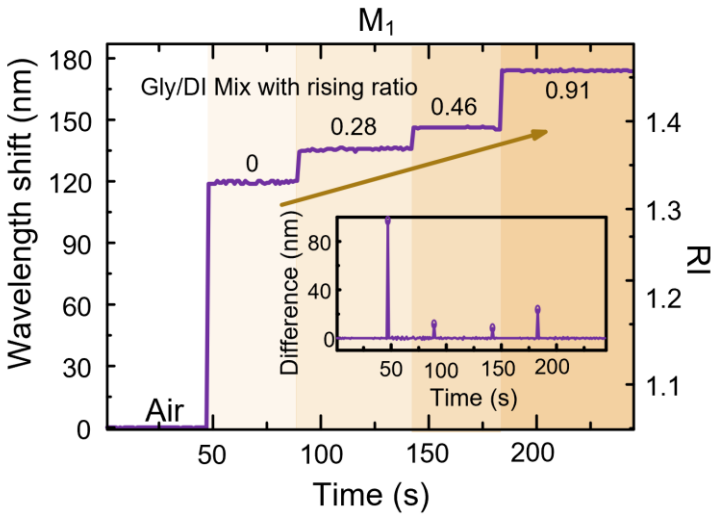

Figure 3-22 Real-time sensing responses for distinct RI media: air and glycol (Gly)/deionized (DI) water mixtures at rising ratios (the weight ratio of Gly in the mixed solution).

The proposed fiber-integrated quasi-BIC sensor demonstrates significant advantages over conventional free-space quasi-BIC configurations and existing fiber-based sensing platforms. Unlike free-space quasi-BIC systems (e.g., quasi-BIC [*72, 74, 77, 79*]), which require stringent angular alignment and complex free-space optics for excitation, our design leverages the intrinsic compatibility of flat-band quasi-BIC modes with the non-ideal planar wavefronts at the fiber endface, enabling robust fiber integration without sacrificing optical performance. This eliminates alignment challenges and paves the way for practical, alignment-free applications in practical sensing scenarios. Furthermore, compared to other fiber-integrated sensors[*27, 29, 126, 127*], our device

achieves a balanced combination of high sensitivity, high *Q*, and strong modulation depth, while maintaining an ultracompact footprint.

Table 3-1 Comparison of experimentally verified metasurface-based sensor

Mechanism	**Material**	**S (nm/RIU)**	***Q***	**ΔR/ΔT (%)**	**Size (μm²)**	**Configuration**
quasi-BIC[*72*]	dielectric	178	2000	20	/	5-deg alignment
quasi-BIC[*77*]	dielectric	112	415(sim)	80	189×189	free-space alignment
quasi-BIC[*74*]	dielectric	413	240	/	/	free-space alignment
quasi-BIC[*79*]	Metal-dielectric	331.9; 492.7	412	60	500×500	free-space alignment
Resonance[*126*]	Au	/	~20		14×14	Fiber integration
nanoring resonator[*27*]	Au	520	~22(on fiber tip)	>50	150×150	Fiber integration
SPR[*127*]	Polymer-Au	1439	~7	50	3D structure	Fiber integration
Photonic crystal[*29*]	Au	571	85	30	88×88	Fiber integration
LSPR[*128*]	Au	755	~5	>80	12×12	Fiber integration
This work	**Au**	**346.4, 529.1**	**30**	**55, 85**	**15×15**	**Fiber integration**

S denotes sensitivity. ΔR/ΔT are the modulation depth of reflectance/transmittance. (sim) represents the simulation result.

3.5 Summary

In this work, we have successfully realized a high-Q flat-band plasmonic quasi-BIC metasurface integrated directly on a standard single-mode fiber tip. By leveraging a local-to-nonlocal mode transition mechanism, the inherent dissipative losses of plasmonic quasi-BIC modes are significantly mitigated, enabling sharp resonance excitation in a fiber-integrated platform. Crucially, through systematic analysis of the angular spectrum characteristics of the fiber facet output, we have elucidated the critical relationship between angular dispersion and resonant robustness, both theoretically and experimentally validating that flat-band engineering is essential for maintaining high-Q fiber-tip resonances. Due to the high electric field enhancement and small mode volume of the designed PCSM, with only 1-μL analytes, the sensor is proven sensitive to the real-time RI variation. The designed fiber sensor facilitates integrated measurements with a maximum sensitivity of 592.1 nm/RIU, making it ideal for small-volume detection in medical and biosensing applications.

Our work bridges the gap between fundamental BIC physics and practical fiber-optic applications, paving the way for miniaturized, high-performance optical sensors. Looking forward, the Q factor of our platform could be further improved by replacing metallic metasurfaces with all-dielectric or hybrid dielectric-metallic configurations, which may support higher-Q quasi-BIC resonances.

Chapter 4 Fiber-Integrated Metalens for High-Speed Optical Switch System

Fiber-integrated metalenses have emerged as powerful solutions to overcome conventional lens systems' multifunctional modulation and compactness challenges. In this work, we demonstrate a polarization-decoupled fiber-integrated metalens through planar chiral gold meta-atoms (PCGMs) that circumvent these limitations. Key innovations include: (1) spin-decoupled phase modulation enabled by engineered chirality of meta-atoms, allowing independent LCP/RCP control; (2) Direct fiber-tip fabrication via FIB milling on large-mode-area PCF, achieving 35 μm focal length with 0.357 NA at 1550 nm; (3) Polarization-selective optical switching in high-speed coherent communication systems with 20.7 dB extinction ratio and μs-scale response time. The device's high LCP-to-RCP extinction ratio and seamless integration with commercial fiber infrastructure establish a new paradigm for high-speed optical interconnects in next-generation communication systems.

4.1 Introduction

The increasing requirement for miniaturized and multifunctional optical components has driven the development of metasurfaces as alternatives to conventional refractive optics [*129, 130*]. Their subwavelength thickness not only enables unprecedented design flexibility but also facilitates direct integration with optical fibers, a critical advantage for developing fiber-pigtailed optical systems [*131*]. While these ultrathin platforms can implement arbitrary phase profiles through meta-atom engineering, their intrinsic polarization-dependent operation fundamentally limits applications requiring independent control of circularly polarized states [*132*]. This limitation is particularly evident in metalenses employing PB phase elements, where spin-coupled phase modulation arises from the inherent polarization dependence of symmetric meta-atoms. Such constraint becomes prohibitive for polarization-multiplexed optical communication systems that mandate decoupled LCP and RCP light management [*133*].

Chiral metasurfaces emerge as a compelling solution for spin-decoupling by leveraging engineered mirror symmetry breaking at the subwavelength scale [*134*]. These artificial nanostructures, typically comprising twisted helices, gammadions, or C2-symmetric dielectric resonators, exhibit enhanced chiroptical effects including circular dichroism (CD) amplification and spin-selective phase modulation. Recent breakthroughs leverage such chirality-enabled phase control to achieve spin-decoupled holography with high efficiency in dielectric platforms [*135, 136*]. Plasmonic metasurfaces are engineered to enhance CD, the key property for chiral sensing and optical absorbers [*137, 138*]. While plasmonic metasurfaces generally require complex 3D meta-atoms for significant CD enhancement, systematic investigations of phase modulation via chiral unit engineering remain surprisingly scarce.

In this section, we demonstrate a plasmonic fiber metalens employing planar chiral gold meta-atoms (PCGMs) that achieves spin-decoupled phase control through optimized structural chirality. The schematic is shown in Figure 4-1. To address the spatial constraints of SMF tip configurations, a large-mode-area PCF with a 25 μm core diameter is implemented. This design advancement enables successful direct fabrication of the metalens on the fiber tip using the process detailed in Section 3.3. The integrated device exhibits a 35 μm focal length with FWHM around 2.65 μm for only LCP focusing across the entire C-band spectrum (1530–1565 nm). We deploy the fiber-integrated chiral metalens in a high-speed coherent optical communication system. The metalens demonstrates chirality-induced polarization-selective switching functionality, achieving a 20.7 dB extinction ratio at 2 Gbps data rates and ~600 μs switching time. These results not only validate the device's compatibility with existing optical communication infrastructure but also reveal its significant potential for next-generation optical systems.

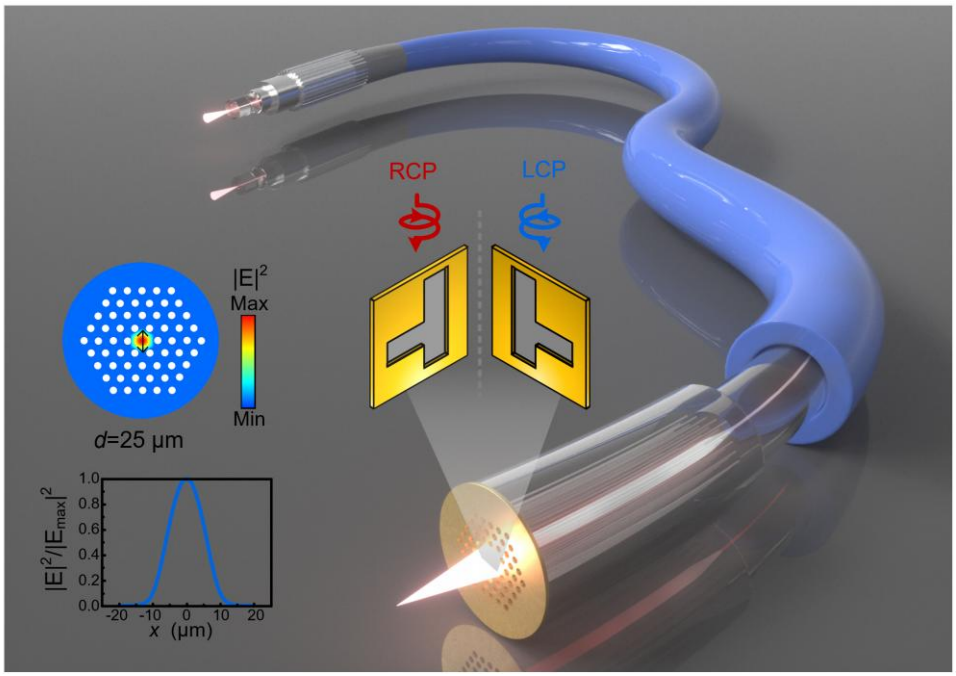

Figure 4-1 Schematic of photonic crystal fiber-integrated spin-decoupled metalens based on planar chiral units.

4.2 Theory and Numerical Simulation

Figure 4-2(a) schematically depicts the proposed PCGM. The chiral meta-atom comprises a C1-symmetric gold structure featuring a deformed L-shape with period p = 700 nm, fixed leg length l_1 = 500 nm, and thickness t = 100 nm. Tunable parameters, including short leg length l_2, widths w_1 and w_2, and bottom offset k, enable systematic control of chiroptical responses. Unlike conventional mirror-symmetric meta-atoms like nanorods, the introduced mirror symmetry breaking induces distinct electric field distributions under LCP and RCP illumination, as evidenced in Figure 4-2(b). Field localization analysis reveals position-dependent resonant behaviors across the meta-atom, establishing structural parameter engineering as an effective pathway for chiral phase difference manipulation.

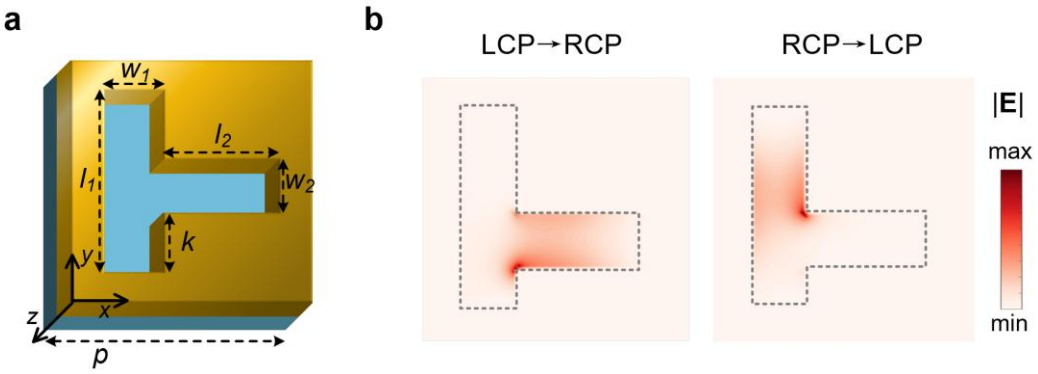

Figure 4-2 Schematic of chiral unit modulation. (a) Geometric details of PCGM. **(b)** The electric field of *xy*-view at *z*=50 nm for the PCGM showing LCP→RCP and RCP→LCP transitions.

Through precise parameter optimization, full 2π phase coverage is achieved for both LCP and RCP excitations. Figures 4-3(a) and (b) present the transmittance amplitude and phase difference profiles for LCP-to-RCP conversion as functions of l_2 and k. Notably, the results of the transition of RCP-LCP can be easily obtained by flipping at

the white dotted line at k=200 nm. Thus, it is possible to obtain a similar amplitude of LCP and RCP but different phase delays by just modulating the geometry of unit cells.

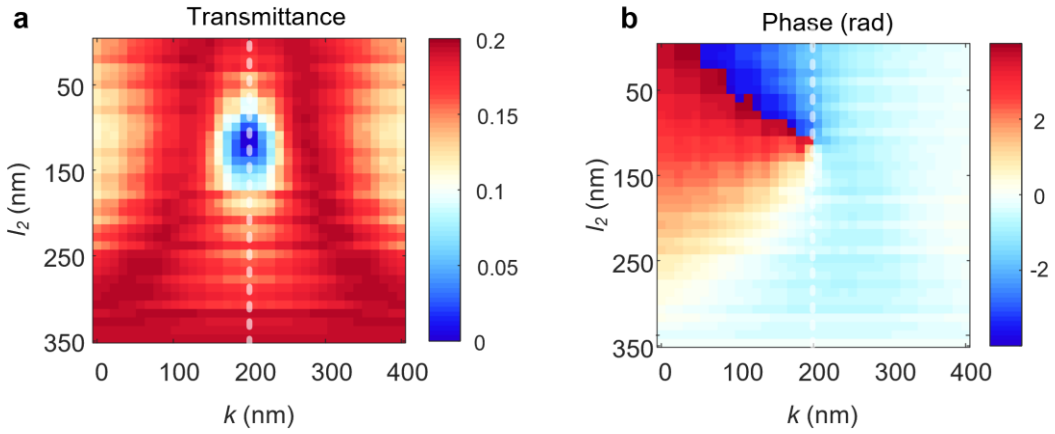

Figure 4-3 (a) Transmittance and **(b)** phase delay at sweeping k and l_2 for the transition of LCP→ RCP. The results of the transition of RCP→LCP can be easily obtained by flipping at the white dotted line at k=200 nm.

4.2.1 Chiral phase modulation mechanism.

To investigate the chiral light-matter interaction, under the condition of plasmonic meta-atom and the subwavelength anisotropic nano-antennas, the excited magnetic field of the meta-atom can be neglected, and the electric field of the PCGM can be approximately represented as an electric dipole $\vec{p}$ in the xy-plane. The expression of the electric dipole $\vec{p}$ is [*139*],

$$\begin{pmatrix} p_x \\ p_y \end{pmatrix} = \varepsilon_0 \begin{pmatrix} \chi_{xx} & \chi_{xy} \\ \chi_{yx} & \chi_{yy} \end{pmatrix} \begin{pmatrix} E_{ix} \\ E_{iy} \end{pmatrix} \tag{4-1}$$

Where χ_{xx}, χ_{xy}, χ_{yx}, and χ_{yy} are the components of the second-rank polarizability tensor. E_{ix} and E_{iy} represent the incident electric field's projection along the x and y directions. The mirror-symmetric meta-atom prohibits cross-coupling. Thus,

the cross components of electric polarizability tensor are zero, $\chi_{xy} = \chi_{yx} = 0$, $\chi_{xx} \neq \chi_{yy} \neq 0$. However, for C1 symmetry meta-atoms, structures without any symmetry, all tensor components can be non-zero, $\chi_{xy} = \chi_{yx} \neq 0$, $\chi_{xx} \neq \chi_{yy} \neq 0$. The non-zero cross-polarization response $\chi_{xy} = \chi_{yx} \neq 0$ is the key to achieving spin decoupling. To evaluate the chiral response to the cross-polarization components, we made the base transition by,

$$\begin{bmatrix} i_+ \\ i_- \end{bmatrix} = \frac{1}{\sqrt{2}} \begin{bmatrix} 1 & j \\ 1 & -j \end{bmatrix} \begin{bmatrix} i_x \\ i_y \end{bmatrix} \tag{4-2}$$

Where i_+ denotes LCP incidence component, and i_- denotes RCP incidence component. The electric dipole moment $\vec{p}$ in the circular basis can be expressed as,

$$\begin{aligned} \begin{pmatrix} p_+ \\ p_- \end{pmatrix} &= \frac{1}{2}\varepsilon_0 \begin{pmatrix} \chi_{++} & \chi_{+-} \\ \chi_{-+} & \chi_{--} \end{pmatrix} \begin{pmatrix} E_{i+} \\ E_{i-} \end{pmatrix} \\ &= \frac{1}{2}\varepsilon_0 \begin{pmatrix} \chi_{xx} + \chi_{yy} + j(\chi_{xy} - \chi_{yx}) & \chi_{xx} - \chi_{yy} - j(\chi_{xy} + \chi_{yx}) \\ \chi_{xx} - \chi_{yy} + j(\chi_{xy} + \chi_{yx}) & \chi_{xx} + \chi_{yy} - j(\chi_{xy} - \chi_{yx}) \end{pmatrix} \begin{pmatrix} E_{i+} \\ E_{i-} \end{pmatrix} \end{aligned} \tag{4-3}$$

Where, p_+ and p_- are the electric dipole components of the LCP and RCP, χ_{xx}, χ_{xy}, χ_{yx}, and χ_{yy} correspond to the respective components of the electric polarizability tensor under circular base.

$$\vec{p} = \begin{pmatrix} A_1 e^{j\varphi_1} & A_2 e^{j\varphi_2} \\ A_2 e^{-j\varphi_2} & A_1 e^{-j\varphi_1} \end{pmatrix} \begin{pmatrix} E_{i+} \\ E_{i-} \end{pmatrix}$$

$$\text{where, } \begin{cases} A_1 = \dfrac{1}{2}\varepsilon_0 \sqrt{(\chi_{xx} + \chi_{yy})^2 + (\chi_{xy} - \chi_{yx})^2} \\ A_2 = \dfrac{1}{2}\varepsilon_0 \sqrt{(\chi_{xx} - \chi_{yy})^2 + (\chi_{xy} + \chi_{yx})^2} \\ \varphi_1 = \arctan \dfrac{\chi_{xy} - \chi_{yx}}{\chi_{xx} + \chi_{yy}} \\ \varphi_2 = -\arctan \dfrac{\chi_{xy} + \chi_{yx}}{\chi_{xx} - \chi_{yy}} \end{cases} \tag{4-4}$$

To evaluate the amplitude and phase modulation induced by the electric polarizability tensor components, the electric dipole components indicated by electric polarizability

tensors can be further simplified as shown in equation 4-4, where the simplified amplitudes A_1 and A_2, and phase delays φ_1 and φ_2 are calculated by the electric polarizability tensor components. As a subwavelength metasurface, the transition electric field can be calculated by the electric dipole moment as $\vec{E}_t = A_0\vec{p}, \text{where}, A_0 = \frac{\omega^2}{4\pi\varepsilon_0 c^2 r}$. Thus, the phase delays φ_1 and φ_2 induced by cross-components of the electric polarizability tensors can finally add to the transmission electric field. Considering the PB phase with Jones matrix indicated in Section 2.1.1, the transmission electric field after passing through the designed symmetry-breaking chiral units can be expressed as,

$$\begin{pmatrix} E_{t+} \\ E_{t-} \end{pmatrix} = \begin{pmatrix} t_{++}e^{j\phi_{++}^{\chi}} & t_{+-}e^{j(\phi_{+-}^{\chi}+\phi_{PB})} \\ t_{-+}e^{j(\phi_{-+}^{\chi}+\phi_{PB})} & t_{--}e^{j\phi_{--}^{\chi}} \end{pmatrix} \begin{pmatrix} E_{i+} \\ E_{i-} \end{pmatrix}$$
$$\begin{aligned} \phi_{++}^{t} &= \phi_{++}^{\chi} = \phi_P - \varphi_1 \\ \phi_{+-}^{t} &= \phi_{+-}^{\chi} + \phi_{PB} = \phi_P - \varphi_2 - 2\theta \\ \phi_{-+}^{t} &= \phi_{-+}^{\chi} + \phi_{PB} = \phi_P + \varphi_2 + 2\theta \\ \phi_{--}^{t} &= \phi_{--}^{\chi} = \phi_P + \varphi_1 \end{aligned} \tag{4-5}$$

For mirror-symmetric meta-atoms, the polarizability tensor exhibits diagonal components ($\chi_{xy} = \chi_{yx} = 0$) so that chiral phase $\varphi_1 = \varphi_2 = 0$, restricting chiral phase modulation to conventional PB phase methods. Superior to that, the C1-symmetric PCGMs break mirror symmetry ($\chi_{xy} = \chi_{yx} \neq 0$), enabling an intrinsic chiral phase term φ_2 that arises from asymmetric near-field interactions between LCP/RCP light and plasmonic modes. This fundamentally decouples spin-dependent phase modulation, providing additional freedom beyond PB phase limitations.

To systematically address the spin-decoupling challenge in fiber-integrated metalenses, we developed a parametric meta-atom library spanning four geometric variables (w_1, w_2, l_2, k) that collectively control chiral near-field interactions and propagation phase characteristics. Through electromagnetic simulations and Jones calculus optimization, we identified eight distinct C1-symmetric gold units (Figure 4-4c) that simultaneously satisfy two performance criteria. The first criterion is complete 2π phase modulation for LCP→RCP conversion while maintaining $<0.1\pi$ phase variation in RCP→LCP channel, which is shown in Figure 4-4(a). While the second criterion is high and equal transmittance for both transitions. As illustrated in Figure. 4-4(b), the selected units exhibit ~20% polarization transmittance. The geometries of the 8 selected units are illustrated in Figure 4- 3(c). The detailed geometry of the selected units is shown in Table 4-1.

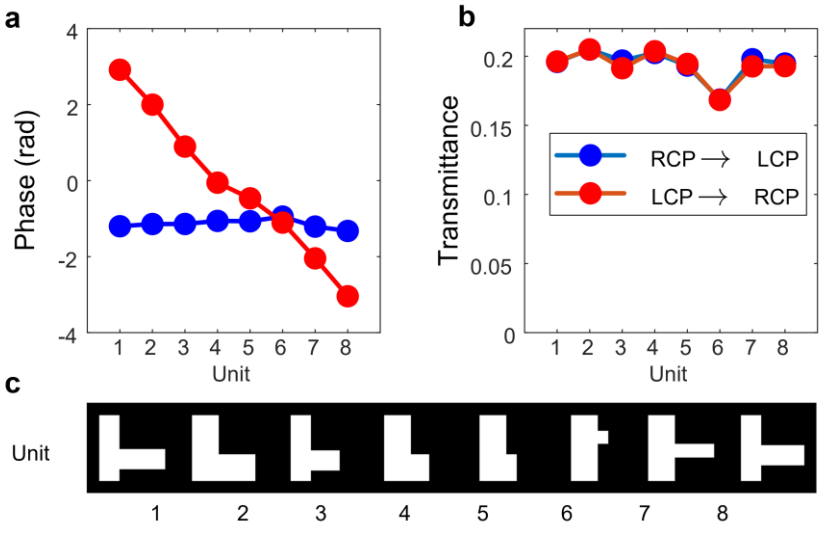

Figure 4-4 Selected eight PCGMs. The relative transmittance **(a)** and chiral phase delay **(b)** of the transition of RCP→LCP and LCP→RCP, respectively. **(c)** shows the geometry of the selected PCGMs.

Table 4-1 Geometry of selected chiral units, in nm unit.

Unit	w_1	w_2	l_2	k	φ_{LR}(rad)	φ_{RL}(rad)
1	150	150	500	90	3.033	-1.13049
2	200	200	500	0	2.000	-1.14
3	150	150	370	80	0.896516	-0.8
4	200	200	320	0	-0.05334	-1.05968
5	200	200	280	0	-0.46509	-0.807343
6	200	100	280	280	-1.10404	-0.845977
7	200	100	500	180	-2.04485	-1.27455
8	150	150	480	120	-3.04178	-0.90918

4.2.2 Metalens design

To demonstrate the phase modulation capability of the designed PCGMs. We first used the selected eight meta-atoms to design a plasmonic metalens tailored for LCP incident light focusing. The LCP phase profile with a focusing performance is,

$$\varphi_{LCP} = -2\pi / \lambda \cdot (\sqrt{x^2 + y^2 + f^2} - f) \tag{4-6}$$

where, wavelength λ=1550 nm, designed focal length f = 35 μm, and (x, y) denotes the meta-atom position. The designed phase profiles are illustrated in Figure 4-5. Using the selected PCGMs, the designed metalens has a focusing phase performance only for LCP (Figure 4-5 (a)), and almost no phase change for RCP incidence light (Figure 4-5 (b)). The designed phase delays align well with the ideal, as shown by the cut line at y=0.

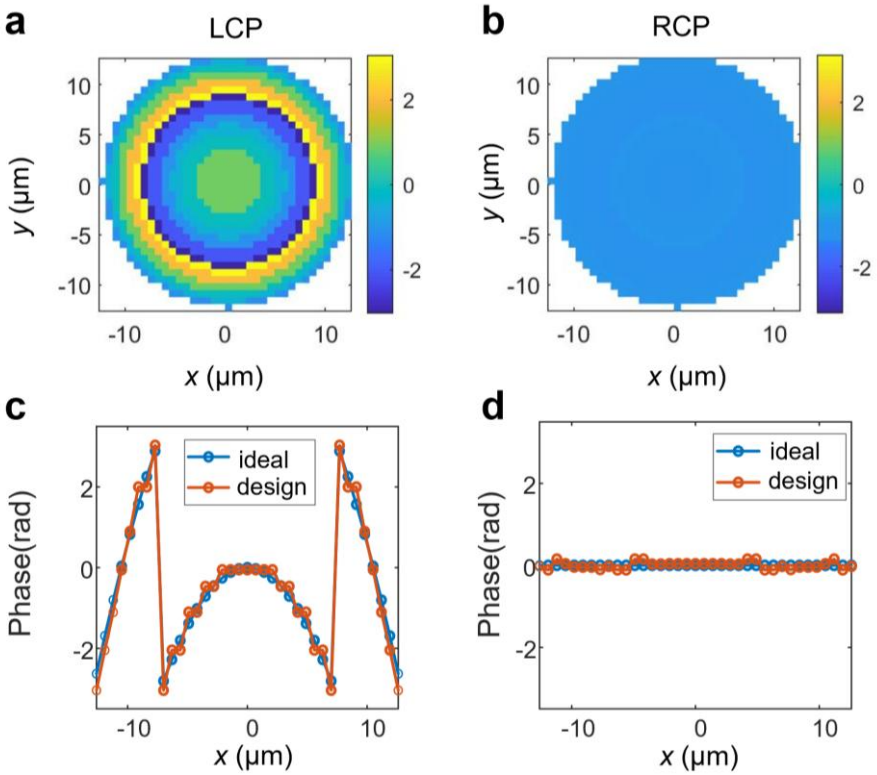

Figure 4-5 Phase profile for metalens by chiral units. (a) Designed phase distribution in the *xy*-plane for LCP wave focusing. **(b)** Phase distribution in the *xy*-plane under RCP wave illumination. Comparison between ideal and designed phase profiles for **(c)** LCP and **(d)** RCP cases at y=0 μm.

4.3 Fabrication and Experiment results

4.3.1 Fabrication results

The fundamental conflict between metasurface design requirements and the SMF fiber tips' limited area restricts functional complexity and light-matter interaction efficiency. To address the problem, we utilized the large-mode-area photonic crystal fiber (LMA-PCF) with a 25-μm core diameter, which is sufficient for a metalens with a focal length of 35 μm to satisfy complete phase coverage. The designed metalens is fabricated on the LMA-PCF with a 20-cm length, following the nanofabrication protocol detailed in Section 3.3. The other side of the PCF is fused with a standard SMF patch cord to ensure

compatibility with a high-speed optical communication system. The metalens design employs a 700-nm lattice period and a 25.9-μm aperture, precisely matching the LMA-PCF's fundamental mode profile. First, a 100-nm-thick gold (Au) layer is deposited, followed by FIB etching based on the designed patterns for approximately 20 minutes. The fabrication results are shown as Figure 4-6, where Figure 4-6(a) is the side view of a fiber metalens with a protective sleeve. Figure 4-6(b) and (c) demonstrate the etching area and etching details, where the units are aligned with the geometry in Table 4-1 with an error within ±20 nm.

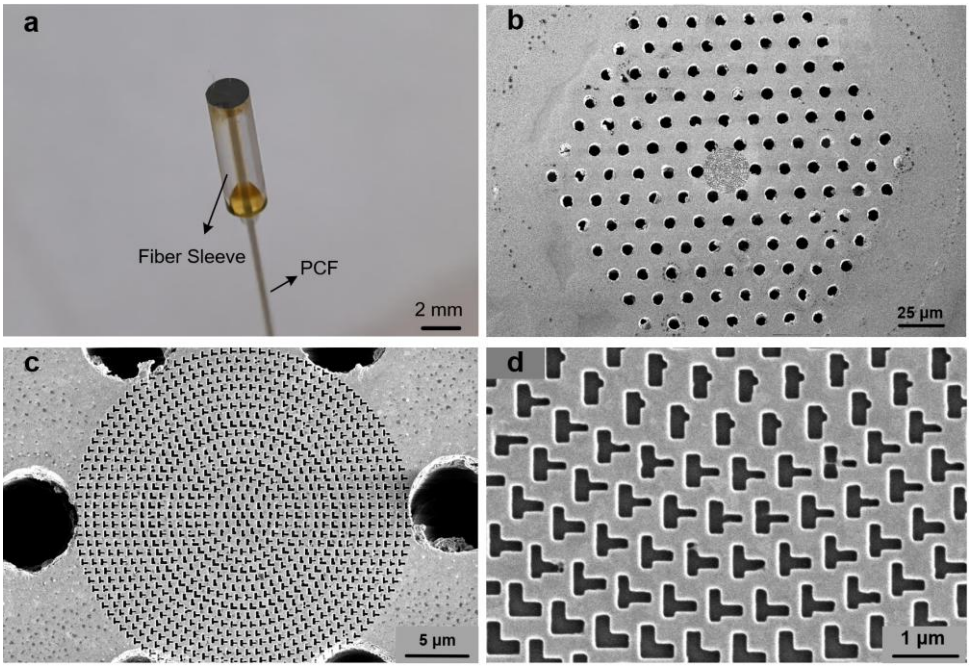

Figure 4-6 Fabricated PCF metalens. (a) Side-view of the fiber-integrated metalens. (**b**) The SEM view of the whole PCF tip with metalens fabricated on the core. **(c)** SEM image of the metalens structure on the fiber core. **(c)** High-magnification SEM image showing the etched nanostructures.

The fabricated PCF sample was fusion-spliced to a 50-cm SMF patch cord. The measured insertion loss of 1.6 dB (recorded by a free-space optical power meter) is primarily attributed to mode field mismatch between the fibers and partial core collapse of PCF during the splicing process.

4.3.2 Focusing characterization

The experimental setup for focusing characterization is schematically depicted in Figure 4-7. A tunable wavelength laser TSP-1000 emitting in the 1530-1560 nm range sequentially passes through a linear polarizer (LP) and quarter-wave plate (QWP) pair for precise polarization modulation of the incident light. Fiber collimators (FC) are used for free-space polarization control. The fabricated fiber metalens is mounted on a piezoelectric positioning stage (PZP stage) for measuring the focusing performance along the *z*-axis with a resolution of 2 nm. The focused beam is subsequently collected by a 50× objective lens (OL) and tube lens (TL) assembly. Following additional polarization modulation through a second LP-QWP combination, the optical signal is ultimately detected by a broadband digital short-wave infrared (SWIR) camera.

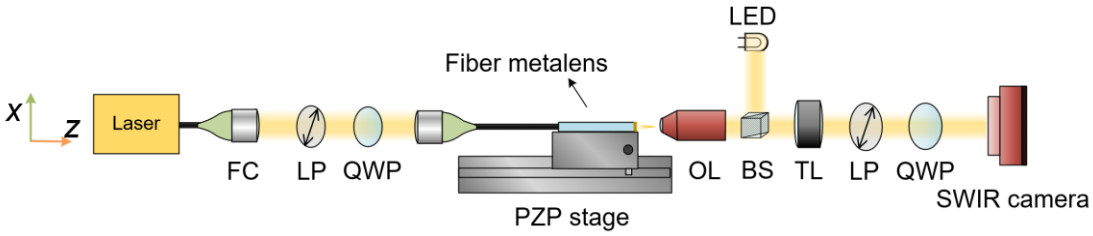

Figure 4-7 Experimental setup for characterizing the metalens focusing performance. Key components: BS- beam splitter.

To establish an absolute reference for focal length determination, a metalens imaging protocol was implemented through a calibrated procedure. The metalens mounted on the fiber tip was first aligned to the $z = 0$ position under 1550-nm LED illumination. As shown in Figure 4-8(b), the image was captured using the BS positioned between the OL and TL, enabling coaxial illumination of the fiber tip while preserving the detection optical path. Following confirmation of the $z = 0$ reference position, the PZP stage was

systematically translated along the *z*-axis to identify the focal plane with focal length *f*, which corresponded to the axial position exhibiting maximum signal intensity in the detection channel, as demonstrated in Figure 4-8(c).

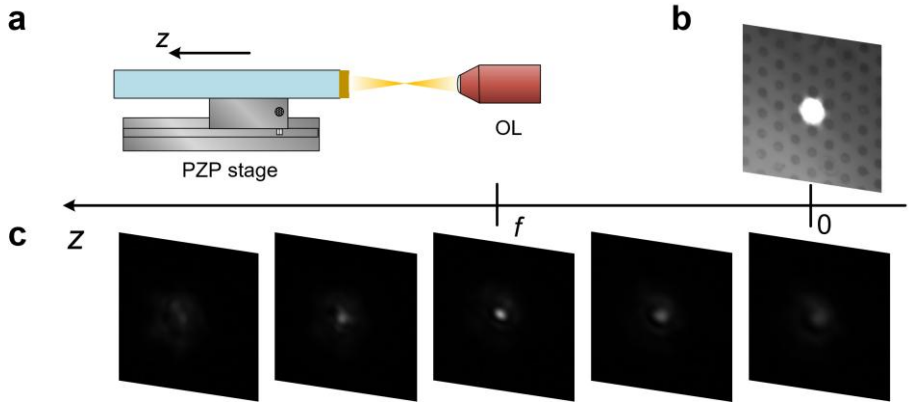

Figure 4-8 Experimental calibration of the metalens position. (a) Schematic of fiber-integrated metalens on PZP stage and objective lens. **(b)** Image of the PCF fiber tip and the metalens. **(c)** Focusing imaging in *xy*-view along the *z*-axis.

The polarization-selective focusing characteristics at λ = 1550 nm were systematically investigated through focal spot analysis, with representative results shown in Figure 4-9. The measured *xy*-plane intensity distribution at the focal plane (*z* = 35.5 μm) under circularly polarized illumination demonstrates pronounced chiral discrimination. Specifically, LCP light achieved diffraction-limited focusing with a normalized peak intensity, whereas RCP illumination exhibited focal intensities below 5% of the LCP peak. As detailed in Figure 4-10, cross-sectional intensity profiles processed via Savitzky-Golay filtering (11-point window, 3rd-order polynomial) reveal an LCP focal spot with a full-width at half-maximum (FWHM) of 2.70 μm, consistent with finite-difference time-domain (FDTD) simulations. This value approaches the theoretical Airy disk limit of 2.63 μm for a numerical aperture (NA) of 0.357. Polarization extinction ratio (PER) analysis based on Stokes parameter measurements further quantified the system performance, yielding a PER of 23.6:1.

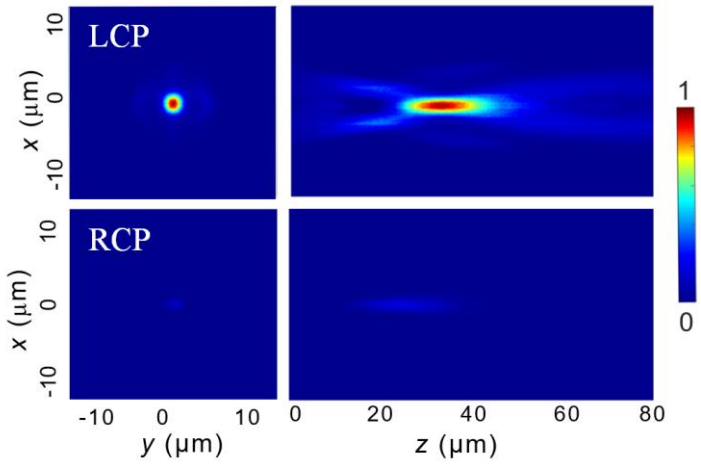

Figure 4-9 The Focusing experiment results of LCP and RCP incident light. Detected light amplitude at the focal point of *xy*-view and focusing performance along *yz*-view.

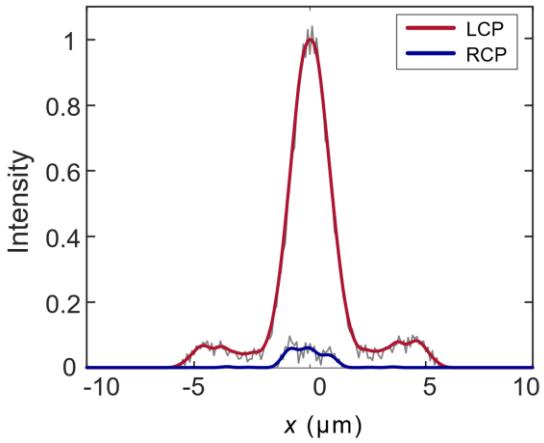

Figure 4-10 Comparison between the LCP and RCP focal amplitude at y=0, z=36.5 μm.

Broadband characterization across the 1530-1568 nm spectrum (Figure 4-11) confirms stable operation with a focal position shift $\Delta z < 2.9$ μm and a FWHM variation confined around 2.68 μm. Focusing efficiency was calculated following $\eta = (P_{\text{focal}} / P_{\text{incident}}) \times 100\%$, where P_{focal} was measured through a 3λ-diameter aperture at focal position, and P_{incident} was calibrated via an undeposited photonic crystal fiber (PCF) reference. The measured efficiency reached around 16%, with primary losses attributable to plasmonic absorption in the gold nanostructures.

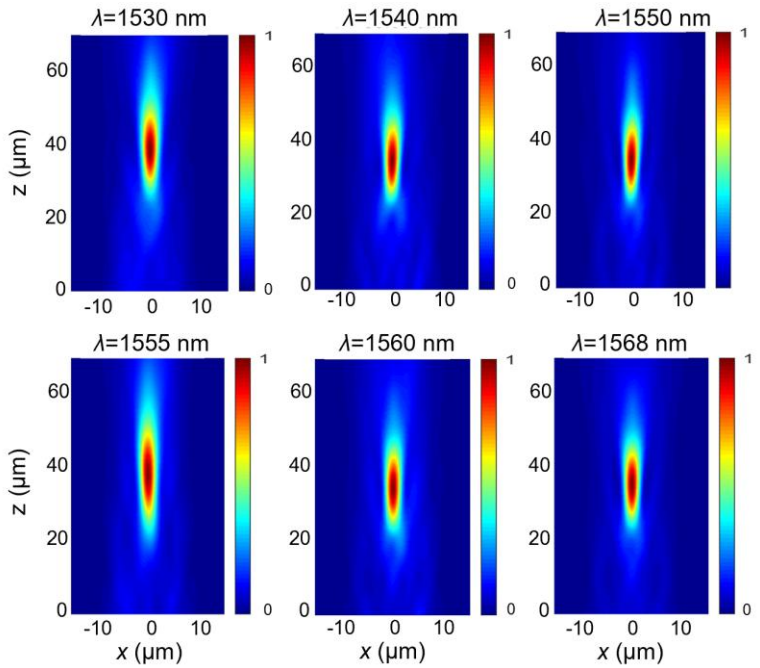

Figure 4-11 Focusing performance along *z* direction, for different wavelengths: λ=1530 nm, λ=1540 nm, λ=1550 nm, λ=1555 nm, λ=1560 nm, λ=1568 nm.

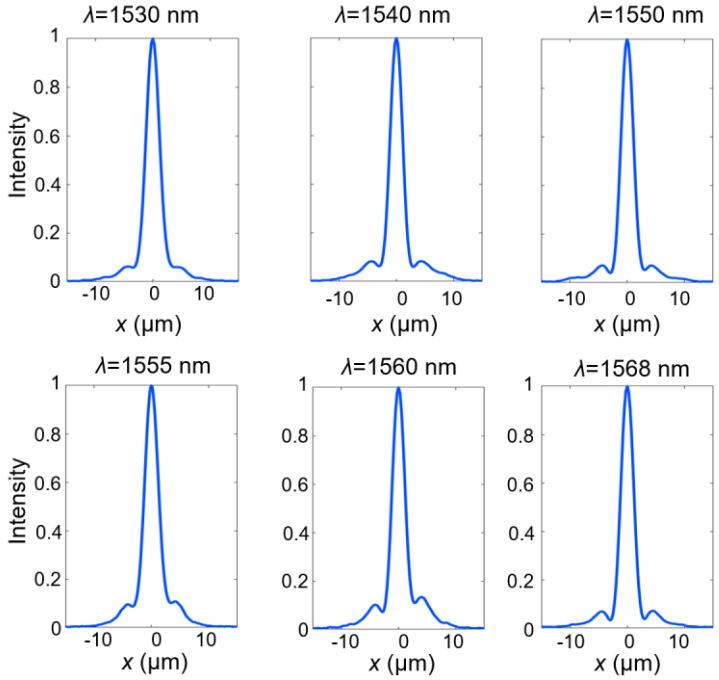

Figure 4-12 Amplitude profile at focal position, for different wavelengths: λ=1530 nm, λ=1540 nm, λ=1550 nm, λ=1555 nm, λ=1560 nm, λ=1568 nm.

4.4 Polarization-Modulated Optical Switch System

4.4.1 High-speed optical communication system setup

To expedite the application for optical interconnects, the proposed PCF metalens is utilized to serve as an optical switch whose on/off state is determined by the polarization state. The feasibility of an optical switch based on a metasurface is experimentally demonstrated by a 10 km standard SMF system with 2Gbit/s PAM4 transmission. The experiment setup is illustrated in Figure 4-13. At the transmitter, the laser source with a linewidth of 200 kHz operates at a wavelength of 1550 nm. Subsequently, the light from the laser source is modulated by a Mach-Zehnder modulator (MZM, Fujitsu FTM7938EZ). To generate the signal, PAM4 modulation is employed due to its dominance in commercial data center networks (DCNs) interconnects. The PAM4 symbols are shaped by a root raised cosine (RRC) filter with a 0.1 roll-off factor. After resampling, the signal is generated via a 5GSa/s arbitrary waveform generator (AWG, Keysight M8190A). The modulated signal is set to 1 GBaud due to the bandwidth limit of the 2D-photodetector (2D-PD). Following the optical modulation, a 10km SSMF is employed to transmit the PAM4 signal. At the receiver, the piezo polarization synthesizer (Luna, PSY201) is utilized to compensate for the polarization evolution in the fiber and align the target polarization state to either LCP or RCP. After that, the signal will propagate through the plasmonic meta-surface. The signal then propagates through the proposed PCF metalens, with assistance from the polarization synthesizer, and functions as an optical switch for DCN interconnects. After detection, the received analog signal is digitized by a digital storage oscilloscope (DSO, Keysight MSOS404A) with a sampling rate of a maximum of 20 GSa/s. Subsequently, the waveforms are

captured by a DSO operating with a sampling rate of 1GSa/s. Finally, the captured waveforms are processed offline in MATLAB.

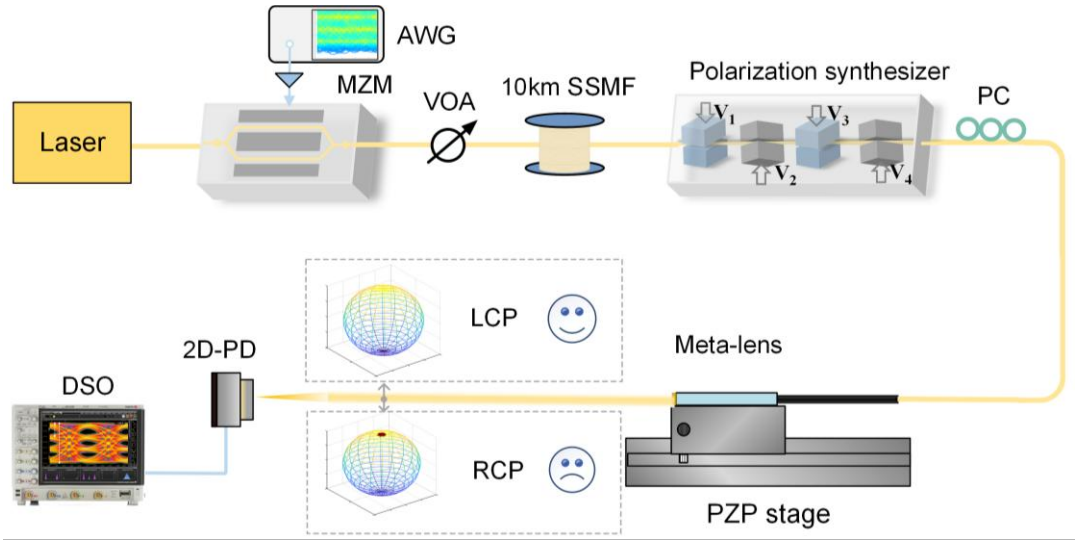

Figure 4-13 Polarization-modulated chiral metalens-enabled optical switching in 2 Gbps coherent communication systems. Metasurface (working wavelength 1550 nm) as polarization-dependent spatial light modulator. VOA: variable optical attenuator.

4.4.2 Optical switch performance

The performance of the optical switch in the "on" state is investigated in Figure 4-14(a). The received optical power (ROP) refers to the signal power received after propagation through the SSMF. It can be observed that the bit rate error (BER) increases as ROP decreases. Specifically, the BERs are 6.7×10^{-5} and 3.4×10^{-3} when the ROPs are -2 and -8 dBm, respectively. For ROP equivalent to -3 dBm, the real-time eye diagram of the PAM4 signal, as presented by DSO employing clock frequency recovery, is shown in Figure 4-14c. The electrical levels of the PAM4 signal, with the polarization state set to LCP by the polarization synthesizer, are clearly distinguishable, indicating that the PCF metalens allows LCP light to pass through. In contrast, the performance of BER severely degrades when the polarization state of PAM4 is RCP, as shown in

Figure 4-14(b). This degradation can be attributed to the metalens blocking the PAM4 signal in the RCP state.

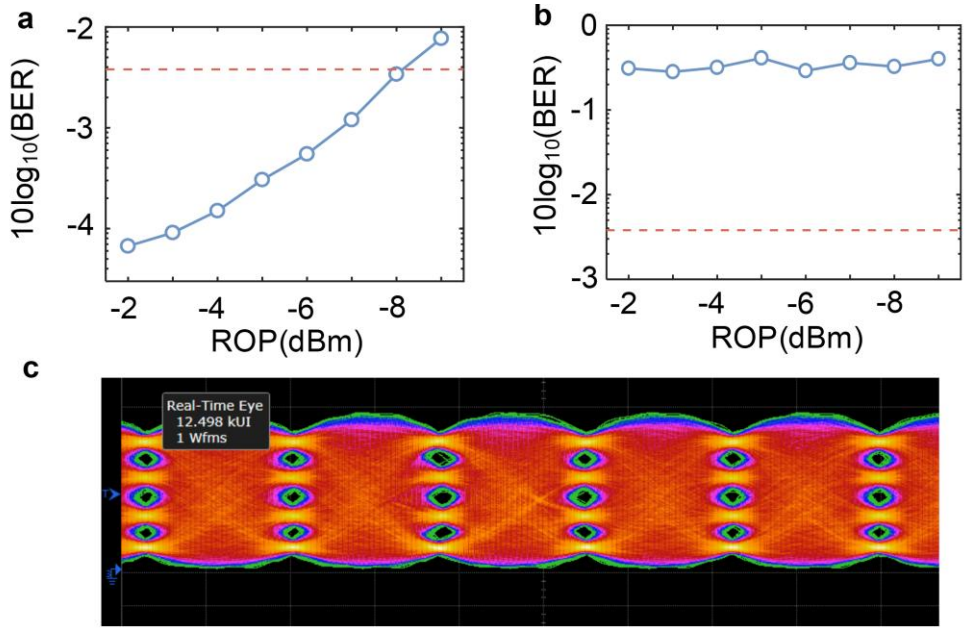

Figure 4-14 (a) BER as a function of ROP when the PAM4 signal is in LCP state. **(b)** BER as a function of ROP when the PAM4 signal is in RCP state. **(c)** The real-time eye diagram of PAM4 in LCP state captured by DSO.

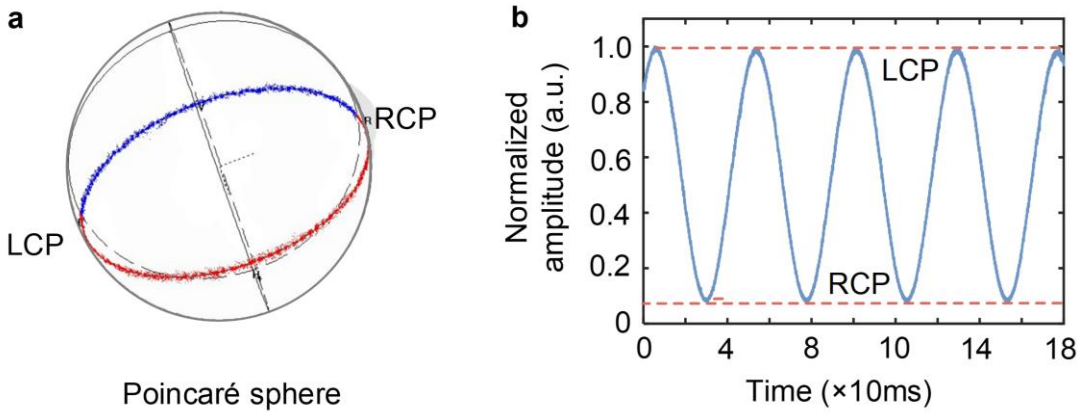

Figure 4-15 (a) The polarization trace of longitudinal circle on Poincaré sphere. **(b)** The detected amplitude by 2D-PD after the light passes through the metalens.

In order to further investigate the performance of the optical switch system, the polarization state of the input of PCF metalens is traced along a longitudinal circle of

the Poincaré sphere. As illustrated in Figure 4-15(a), the longitudinal circle passes through the LCP state, the *x*-axis polarization state, the RCP state, and the *y*-axis polarization state. The detected output of the metalens is shown in Figure 4-15b. Since the polarization state continuously changes between RCP and LCP, the output light intensity through the metalens also varies. It is observed that when the input polarization state is LCP, the light intensity detected by the 2D-PD is at its maximum, and vice versa. The response time and optical extinction ratio of the optical switch are also discussed, which is illustrated in Figure 4-16. The polarization state is configured to rapidly switch between RCP and LCP by adaptively searching along the shortest path.

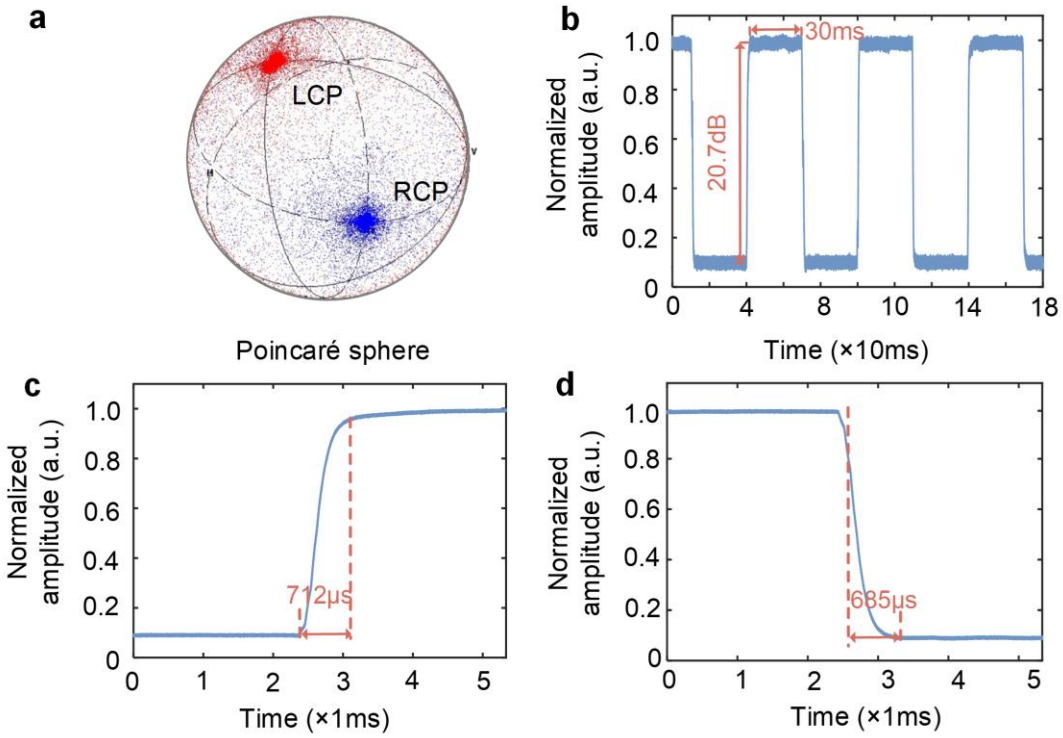

Figure 4-16 (a) The polarization states rapidly switching between RCP and LCP, **(b)** The detected amplitude by 2D-PD after the light passes through the metalens. **(c)** The zoomed-in view of the rising edge of the optical switch. **(d)** The zoomed view of the falling edge of the optical switch.

After reaching the LCP or RCP polarization state, the SOP is maintained for approximately 30 ms to evaluate the stability of the optical switch based on PCF

metalens. The input polarization state of PCF metalens is illustrated in Figure 4-15(a). As shown in Figure 4-16(b), the detected amplitude is at its maximum when the SOP is in the LCP state, while it is at its minimum when the SOP is in the RCP state. The achieved contrast was approximately 20.7 dB, corroborating that the data transmission based on the optical interconnect was sufficiently polarization selective, as intended. Since the polarization state is not perfectly tracked to either RCP or LCP, the output is affected by amplitude noise, which depends on the effectiveness of the polarization state tracking. The zoomed-in views of the response time of the optical switch are shown in Figures 4-16(c) and (d). It can be observed that the rising edge and falling edge are 712 and 685 μs, respectively, which are determined by a polarization synthesizer using four piezoelectric actuator-driven fiber squeezers. It is noteworthy that the response time can be further improved to the ns-level if the electro-optical modulator is employed.

4.5 Summary

This work presents a fiber-integrated metalens employing planar chiral gold meta-atoms and demonstrates its application in high-speed optical interconnects as a polarization-selective switch. Through the implementation of engineered chiral meta-atoms with spin-decoupled phase modulation capabilities, the device enables independent manipulation of LCP and RCP light. Direct integration on a large-mode-area PCF was achieved via FIB milling, yielding a compact 35-μm focal length with 0.357 NA across the C-band while preserving fiber compatibility. Experimental validation in 2 Gbit/s communication systems transmitting PAM4 signals revealed polarization-selective switching performance featuring a 20.7-dB extinction ratio and μs-scale response time, representing a significant advancement in dynamic polarization

control. The synergistic combination of exceptional polarization discrimination (LCP-to-RCP extinction ratio) with seamless fiber integration establishes a transformative platform for next-generation high-speed optical networks, effectively addressing critical requirements for integrated system miniaturization.

Chapter 5 Tunable D-Shaped Fiber Polarizer Based on Graphene

The electromagnetic responses of the meta-fiber devices discussed above remain fixed post-fabrication due to their static structural configurations, significantly limiting their adaptability in dynamic optical systems. Meanwhile, the fiber-tip integration method exhibits limited light–matter interaction regions, which are essential for enhancing sensitivity or efficiency in optical applications. To address these limitations, we present a proof-of-concept design of a D-shaped fiber-based polarization filter integrated with graphene and periodic gold gratings, achieving dynamically tunable polarization filtering through voltage-controlled modulation of graphene's carrier concentration. In this section, we will systematically present three key aspects: (1) the coupling mechanism between gold grating-excited surface plasmon polariton (SPP) modes and the fundamental mode in the D-shaped fiber microstructure, (2) the dynamic optical tunability enabled by precise chemical potential adjustment of graphene, and (3) broadband polarization performance spanning the entire C-band and O-band communication regions.

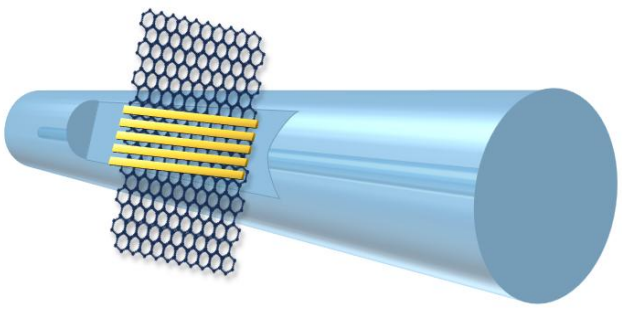

5.1 Introduction

Optical polarizers serve as fundamental components in modern photonic systems, enabling critical functionalities across optical communications, laser instrumentation, and ultra-precise sensing applications. Conventional polarization solutions, notably dichroic film polarizers and Glan-Taylor prisms, exhibit inherent limitations in system integration due to their centimeter-scale dimensions and free-space optical configurations. This has driven significant research efforts toward developing waveguide-integrated polarization filters compatible with optical fiber architectures [*140-142*]. Waveguide-based polarization filtering typically exploits polarization-selective attenuation through evanescent field interactions between guided modes and functionalized cladding materials. Surface plasmon polaritons (SPPs) have emerged due to their unique combination of subwavelength field confinement and intrinsic polarization sensitivity [*143*]. The underlying mechanism involves phase-matched coupling between waveguide modes and SPP excitations at dielectric-metal interfaces, generating polarization-dependent resonance losses. Recent advances in PCFs have further enhanced this paradigm through tailorable birefringence and air-hole microstructures, enabling precise SPR engineering [*144-146*]. Representative designs include dual D-shaped SPR-PCF filters achieving 45 dB polarization-dependent loss and Sierpinski-fractal geometries with 180 nm operational bandwidth [*147-152*]. Nevertheless, the complex structure of PCFs increases the manufacturing cost of relative devices, which limits the application of SPR-PCF polarization filters. Additionally, the parameters of these devices remain fixed after fabrication, thereby failing to satisfy the growing demand for dynamically tunable optical systems.

Graphene's exceptional electro-optic tunability and broadband optical response present transformative opportunities for dynamic photonic devices. As demonstrated in our prior discussion (Section 2.3.3), the synergy between graphene's field-effect tunability and optical fibers' extended interaction lengths enables unprecedented control over light-matter interactions. While the broader family of 2D materials (e.g., TMDCs, BP) offers diverse optoelectronic properties, graphene stands out as the optimal choice for tunable D-shaped fiber polarizers due to its unique combination of ultra-broadband absorption ($\approx$2.3% per layer, Figure 2-16), exceptional and readily implementable electro-optical tunability, and superior compatibility for robust integration onto the complex fiber geometry. However, the loss difference between the two orthogonal polarization states is not large enough to achieve a miniaturized and efficient tunable polarization filter.

In this work, we present a tunable D-shaped fiber polarizer incorporating graphene and gold grating structures. Through dynamic modulation of graphene's chemical potential, we demonstrate adjustable mode coupling between the fiber's fundamental mode evanescent field and the SPP mode induced by the gold grating. This tunable coupling mechanism enables effective operation across both O- and C-band telecommunication windows. The proposed 1-mm-long device achieves a stable extinction ratio of approximately 30 dB while maintaining compatibility with fiber-optic miniaturization requirements. Our analysis reveals significant polarization-dependent characteristics: The XP core mode experiences strong coupling with the SPP mode, resulting in substantial transmission losses reaching 38 dB/mm. In contrast, the YP core mode maintains low propagation loss (0.58 dB/mm) due to minimal SPP interaction. Spectral tunability is achieved through dual control mechanisms, grating period optimization sets the operational band (O-band: 1272-1353 nm or C-band: 1540-

1612 nm), while graphene's chemical potential adjustment enables continuous wavelength tuning within the selected band. This combined approach ensures comprehensive coverage of standard telecommunication wavelengths while providing precise polarization control through electrical tuning.

5.2 Principle and Design

Figure 5-1 illustrates the structural configuration of the proposed D-shaped fiber polarizer. A single-mode fiber was polished on one side, maintaining a distance of 1 μm between the polished plane and the fiber core.

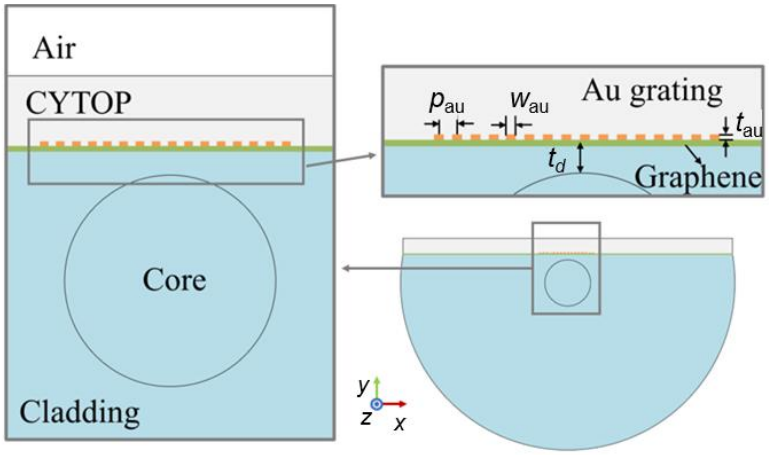

Figure 5-1 Cross-sectional schematic of the D-shaped SMF polarizer. The SMF undergoes side-polishing followed by sequential deposition of a graphene monolayer, gold grating structures, and a 3-μm-thick CYTOP layer. t_d is the distance between the polished plane and the core, and p_{au}, w_{au}, and t_{au} are the period, width, and thickness of the gold grating, respectively.

Subsequently, a monolayer graphene film was deposited onto the polished surface, followed by an array of gold gratings. The grating parameters were optimized with a period p_{au} of 500 nm, a width w_{au} of 225 nm, a thickness t_{au} of 100 nm, and a period number of 20. To satisfy the phase-matching conditions for SPR, a 3-μm-thick CYTOP (Cyclic transparent optical polymer) layer (RIs are 1.3348 and 1.3335 at the

wavelengths of 1.3 μm and 1.55 μm) was coated over the structure. The high RI of CYTOP enhances SPR excitation efficiency while simultaneously serving as an environmental isolation layer. This protective function is critical given SPR's inherent sensitivity to external RI variations [*100*], with the polymer effectively mitigating ambient interference.

The proposed filter was numerically analyzed using a finite element method-based eigenmode solver implemented in COMSOL Multiphysics. A PML surrounds the D-shaped fiber structure to absorb radiant energy and eliminate boundary reflections effectively. The SMF configuration with 8.2 μm core radius, and the RI of fused silica was modeled using the Sellmeier equation 2-1. A physics-controlled mesh with an extremely fine resolution was utilized, incorporating free tetrahedral meshes for the physical domain and swept meshes for the PML regions.

5.2.1 Coupling mechanism: SPR on D-shaped fiber

The filter exhibits remarkable polarization selectivity, demonstrating 32.5 dB/mm attenuation for XP core modes while preserving ultralow loss characteristics (0.58 dB/mm) for YP counterparts. As quantified through the relationship between mode attenuation α and the imaginary component of the effective RI (n_{eff}),

$$\alpha = 8.686 \times \frac{2\pi}{\lambda} \text{Im}(n_{\text{eff}}) \times 10^3 \text{ dB/mm} \tag{5-1}$$

where λ denotes the operating wavelength in micrometers, the distinct behavior manifests prominently at graphene chemical potential μ_c = 0.6 eV (Figure 5-2). The XP mode reveals a sharp resonance peak at λ = 1.326 μm, contrasting with the spectrally flat YP mode response. The wavelength-dependent coupling mechanism is elucidated through normalized electric field distributions in Figures 5-3(a)-(d). At the phase-

mismatched condition (λ = 1.22 μm), the SPP mode (Figure 5-3(a)) is localized at the gold grating at the graphene interface, a weakly perturbed XP core mode (Figure 5-3(b)) with minimal mode coupling. As the wavelength approaches the phase-matching condition λ = 1.326 μm, progressive mode hybridization occurs, strongly hybridized XP core mode coupled to the SPP excitation and reaching maximum coupling strength (Figure 5-3(c)). This strong XP-SPP interaction correlates with the peak attenuation in Figure 5-2, while the YP core mode maintains its fundamental profile without observable coupling (Figure 5-3(d)).

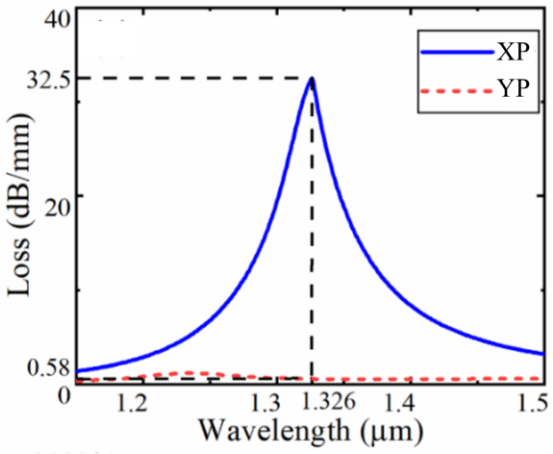

Figure 5-2 Polarization-dependent filtering characteristics. Wavelength-dependent attenuation spectra for XP and YP core modes at graphene chemical potential μ_c = 0.6 eV.

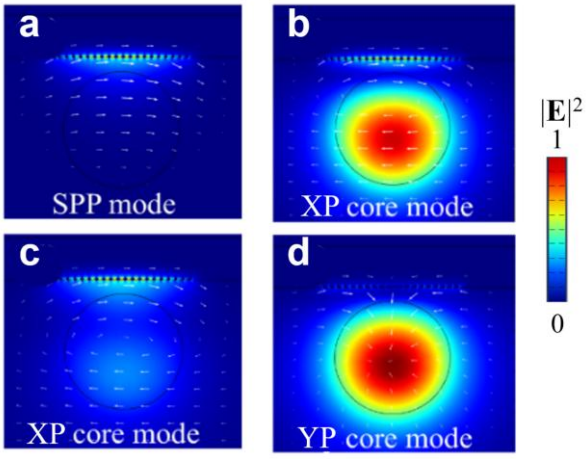

Figure 5-3 (a, b) Cross-sectional electric field distributions at wavelength λ = 1.22 μm for SPP mode and XP core mode, separately. **(c, d)** Phase-matched resonance behavior at λ = 1.326 μm for

strongly coupled XP core mode and unaffected YP core mode. All field plots normalized to maximum intensity ($|\mathbf{E}|^2$), with arrows indicating dominant polarization directions.

These results demonstrate that SPP excitation occurs exclusively in the *x*-polarization direction, enabling strong coupling with the XP core mode. Maximum mode coupling coincides with the resonance wavelength λ = 1.326 μm, explaining the observed XP mode attenuation of up to 32.5 dB/mm. The YP mode remains unaffected due to polarization orthogonality with the SPP field, contributing the YP mode attenuation low to 0.6 dB/mm.

5.2.2 Phase-matching condition

Phase matching between the SPP mode and XP fiber core mode is essential for achieving peak attenuation in the coupled system. Figure 5-4 systematically analyzes this interaction by the loss spectra and dispersion relations of the SPP mode and XP core mode at a chemical potential of 0.6 eV. The pink and blue curves correspond to the SPP mode and XP core mode, respectively, with insets illustrating their electric field distributions. Solid curves represent loss spectra, while dotted curves denote the real part of the effective RI. The loss of the XP core mode arises from its coupling with the SPP mode, which facilitates energy transfer from the core mode to the SPP mode, ultimately inducing core mode attenuation [*153*]. Complete coupling, characterized by maximum core mode loss, occurs at a wavelength of 1.326 μm (Figure 5-4). This phenomenon requires phase-matching conditions, where the propagation constants of the SPP and XP core modes are equal [*143*]. As shown in Figure 5-4, complete coupling is achieved at 1.326 μm when both the Re_n_{eff} and loss values of the two modes coincide. Deviations from this wavelength result in incomplete coupling due to mismatched phase conditions. The electric field distribution insets in Figure 5-4

contrast the fully coupled SPP mode with the partially coupled XP core mode under non-phase-matched conditions.

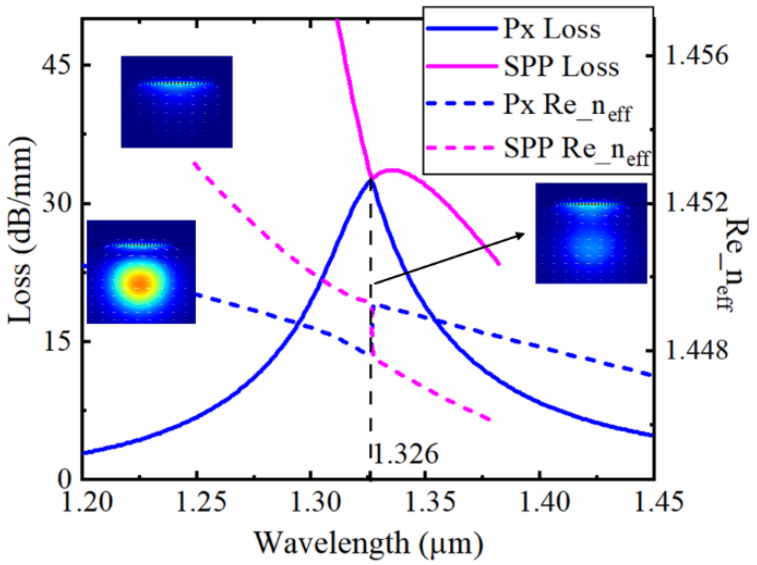

Figure 5-4 Loss spectra, dispersion relations, and electric field distributions of the SPP mode and XP core mode at a chemical potential of 0.6 eV. Solid curves: loss spectra; dotted curves: real part of the effective refractive index Re_n_{eff}. Insets illustrate the electric field profiles of the SPP mode (pink) and XP core mode (blue).

5.3 Simulation and Discussion

5.3.1 Tunability performance

Figure 2-18 in Section 2.3.2 presents the surface conductivity characteristics of graphene at an operational wavelength of 1.33 μm. When the chemical potential increases from 0.5 eV to 1 eV, the real component of surface conductivity maintains stability while the imaginary component exhibits a significant reduction. This conductivity modification induces a blue shift in the resonant wavelength, as will be comprehensively demonstrated through spectral and dispersion analyses in Figures 5-5 and 5-6. The proposed filter design achieves superior XP core mode attenuation (> 30

dB) with minimal YP core mode transmission loss (<0.6 dB/cm), a performance advantage attributable to selective SPP coupling exclusively with the XP mode.

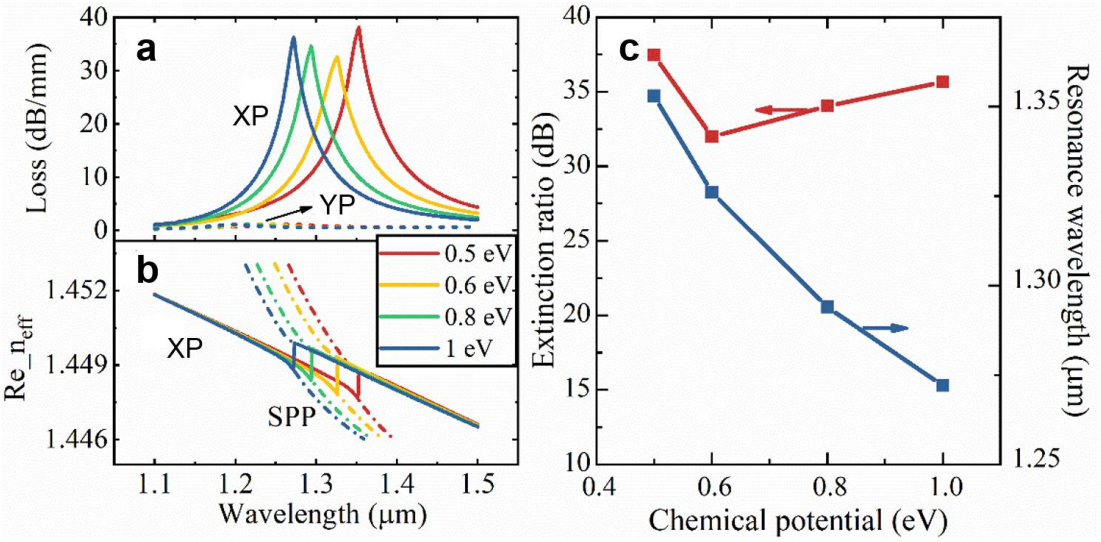

Figure 5-5 Tunable optical responses for O-band operation. Results with the period of gold grating p_{au} = 500 nm under chemical potential μ_c tuning in the range of 0.5–1 eV. **(a)** Attenuation spectra for XP and YP core modes. **(b)** The real part of the effective RI of XP core mode and SPP mode under phase-match conditions. **(c)** Tunability performance: Extinction ratio (solid line, left axis) and resonant wavelength (dashed line, right axis) versus chemical potential.

Numerical simulations confirm that the SPP-induced propagation loss remains effectively constant across the tested chemical potential range (0.5-1 eV). Figure 5-5(a) illustrates the polarization-dependent loss spectra, while Figure 5-5(b) displays the corresponding dispersion relations at different chemical potentials. The spectral tunability is quantified in Figure 5-5(c), showing a linear correlation between chemical potential and resonant wavelength that spans from 1.272 μm to 1.353 μm. This tuning range fully encompasses the O-band telecommunications window (1.26-1.36 μm). The extinction ratio (ER), defined as the logarithmic power ratio between transmitted YP and XP modes [*152, 154*], can be expressed as:

$$ER = 10\log_{10}\frac{P_y}{P_x} = (\alpha_x - \alpha_y)L_f \tag{5-2}$$

where α_x and α_y represent the attenuation coefficients (dB/mm) for respective polarization modes, and L_f denotes the 1-mm filter length. As evidenced in Figure 5-5(c), the ER maintains peak values exceeding 30 dB throughout the chemical potential adjustment range across the entire O-band. This performance consistency confirms the design's robustness for tunable polarization filtering applications.

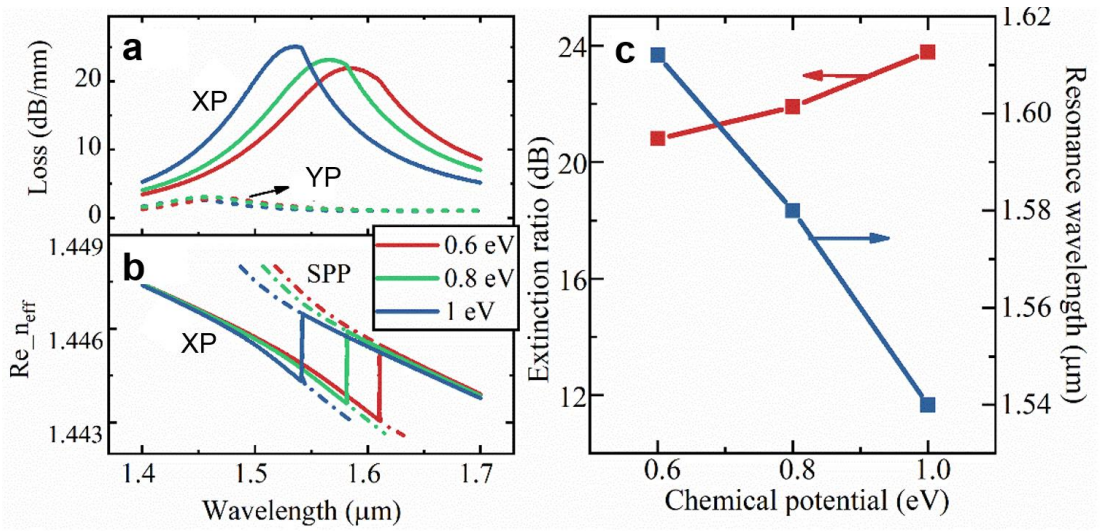

Figure 5-6 Tunable optical responses for C-band operation. Results with the period of gold grating p_{au} = 440 nm, under chemical potential changes from 0.6 eV to 1 eV. **(a)** Attenuation spectra of XP and YP core modes. **(b)** The real part of the effective RI of XP core mode and SPP mode under phase-match conditions. **(c)** Extinction ratio and resonant wavelength versus chemical potential.

The fiber polarizer can be tuned by both the graphene chemical potential and the gold grating parameter. When the period of the gold grating p_{au} is changed to 440 nm, the SPP mode resonance shifts to the vicinity of 1550 nm, enabling operation within the C-band (1530–1565 nm), as demonstrated in Figure 5-6. Specifically, Figure 5-6(a) shows the attenuation spectra of the XP and YP core modes, revealing polarization-selective mode loss. Figure 5-6(b) illustrates the phase-matching condition between the XP core

mode and SPP mode through their effective refractive indices (Re_n_{eff}). Notably, dynamic tuning of μ_c from 0.6 eV to 1 eV allows the resonant wavelength to span the entire C-band while maintaining an ER exceeding 20 dB (Figure 5-6(c)).

Compact fiber polarizer size. The dependence of extinction ratio on fiber polarizer length under varying chemical potentials is shown in Figure 5-7. A threshold of 20 dB is applied to define the operational bandwidth. As the fiber length increases from 1 mm to 3 mm, the extinction ratio improves significantly to 37.4 dB, 74.9 dB, and 112.3 dB, with corresponding bandwidths of 125 nm, 192 nm, and 236 nm, respectively. To balance performance and compactness, a 1-mm-long polarizer is selected for our design. This configuration achieves sufficient bandwidth (125 nm) to fully cover the O-band (1260–1360 nm) while maintaining a low insertion loss of approximately 0.6 dB for *y*-polarized light.

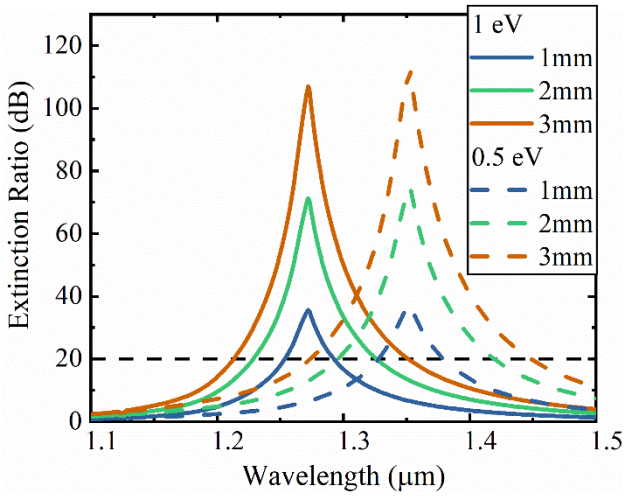

Figure 5-7 Extinction ratio versus wavelength at different fiber polarizer lengths (from 1mm to 3 mm), under 0.5 eV and 1 eV chemical potentials.

5.3.2 Fabrication flow and robustness.

The potential fabrication process of the proposed polarization filter comprises three stages, integrating precision fiber processing with advanced nanomaterial integration.

Initially, a standard SMF is secured in a groove with a controlled depth of approximately 68 μm, where the protruding fiber segment is mechanically polished to form a D-shaped cross-section. This critical surface processing achieves exceptional smoothness with surface roughness below 1 nm [*94*]. Subsequently, high-quality single-layer graphene is synthesized on copper foil through chemical vapor deposition (CVD), followed by the fabrication of gold grating patterns via electron beam lithography (EBL) and electron beam deposition systems. A protective CYTOP coating is then applied over the graphene-gold grating structure before transferring the composite film onto the D-shaped fiber surface using an established transfer methodology [*94*]. The final stage involves the integration of metallic electrodes on the fiber platform to enable electrical modulation of graphene's chemical potential, essential for achieving tunable filtering characteristics [*155*]. Future experimental work will focus on the practical implementation and performance characterization of this device.

To evaluate the device's tolerance to fabrication variations, Table 5-1 presents performance metrics at core-graphene distances of 0.5, 1.0, and 1.5 μm. The XP core mode consistently exhibits high propagation losses exceeding 20 dB/mm, with peak attenuation observed at 1.0 μm separation. In contrast, YP core mode losses remain below 1 dB/mm and demonstrate a gradual reduction with increasing separation distance. Notably, the resonant wavelength maintains remarkable stability, showing minimal spectral shift ($\Delta\lambda < 0.5$ nm) across the tested parameter range. These results confirm that the filter's polarization selectivity and spectral characteristics exhibit strong insensitivity to core-graphene distance variations, significantly relaxing the precision requirements for device assembly. This inherent tolerance substantially reduces manufacturing complexity while preserving optimal performance characteristics.

Table 5-1 Results of different core-graphene distances at μ_c=1 eV.

Core-graphene distance	0.5 μm	1 μm	1.5 μm
YP attenuation (dB/mm)	0.71	0.54	0.36
XP attenuation (dB/mm)	29.06	36.21	22.22
Extinction ratio (dB)	28.35	35.67	21.86
Resonant wavelength (μm)	1.299	1.272	1.264

Table 5-2 Performance comparison with other existing works

Description	Wavelength (nm)	Extinction ratio (dB)	Insertion loss (dB)	Device length (mm)
Two-core PCF single-polarization wavelength splitter (simulation) [*156*]	1296 - 1304 1548 - 1552	> 20	< 0.05	10.7
Single-core PCF single-polarization wavelength splitter (simulation) [*157*]	1304 - 1316 1536 - 1564	> 20	~0.48 ~2.73	20
SPR induced polarization filter based on D-shaped PCF (simulation)[*149*]	1550	~37.61	~0.02	1
Broadband graphene polarizer (experiment) [*19*]	820 - 955 1530 - 1630	~15 ~19	-- ~5	3 2.1
Bimetal-coated PCF polarization filter (simulation) [*158*]	1310 1560	~53.2 ~12.33	~1.23 ~2.4	1
PCF-based SPR induced polarization filter (simulation) [*159*]	1550	~44.52	~0.08	1
This work (simulation)	1272 - 1353 1540 - 1612	32 - 37 21 - 24	~0.6 ~1.2	1

5.3.4 Discussion

As summarized in Table 5-2, the device achieves extinction ratios of 32–37 dB in the O-band and 21–24 dB in the C-band, with insertion losses limited to ~0.6 dB and ~1.2 dB, respectively, within a compact 1 mm footprint. This performance advances designs through three critical innovations: broadband operation across full communication bands, unlike conventional wavelength-specific fiber-based counterparts [*158, 159*]; balanced loss-ratio performance, where subwavelength gold gratings reduce insertion losses to <1.2 dB while retaining extinction ratios >20 dB, addressing the high-loss limitations (~5 dB) of earlier graphene-based polarizers [*19*]; and compact electrotunability, achieving plasmon-enhanced extinction ratios comparable to centimeter-scale devices [*156, 157*] while enabling electrical wavelength tuning via graphene integration, a capability absent in static SPR systems [*149, 159*]. The D-shaped SMF substrate provides inherent compatibility with standard telecom infrastructure, while the graphene-grating heterostructure introduces a scalable pathway for dynamic polarization management in wavelength-division multiplexing networks and integrated photonic circuits. Future experimental validation will focus on optimizing grating dimensions and graphene doping levels to further enhance extinction ratios while minimizing insertion losses.

5.4 Summary

In conclusion, we demonstrate a graphene-integrated D-shaped single-mode fiber polarizer with electrically tunable broadband operation. The synergistic combination of monolayer graphene and subwavelength gold gratings enables wavelength-selective SPR, achieving polarization extinction ratios exceeding 20 dB over 125 nm (O-band)

and 72 nm (C-band) spectral ranges. By modulating the graphene chemical potential, dynamic switching between O-band (1.272–1.353 μm) and C-band (1.54–1.612 μm) operation is realized, accompanied by ultralow insertion losses of 0.6 dB and 1.2 dB, respectively. The 1 mm compact design leverages localized plasmonic enhancement while maintaining fabrication simplicity, critical advantages enabled by the robust performance independence from core-graphene spacing and standard fiber compatibility. These features position the device as a promising candidate for reconfigurable polarization management in wavelength-division multiplexing systems and integrated photonic circuits.

Chapter 6 Conclusions and Outlook

This thesis establishes fiber-integrated metasurfaces and graphene hybrids as a transformative paradigm for next-generation optical system, addressing fabrication complexity, mode mismatch, and dynamic control. Chapter 2 lays the theoretical groundwork for metasurface-fiber synergy, while Chapters 3–5 experimentally validate ultra-sensitive quasi-BIC sensing (1 μL detection), chiral polarization switching (2 Gbps PAM4 signal), and gate-tunable polarizers (C/O-band adaptability). Collectively, these advances demonstrate scalable fabrication, resonant engineering, and active reconfiguration strategies. Emerging opportunities in dielectric metalenses, advanced nanofabrication, and multifunctional active devices are poised to expand applications in quantum optics, hyperspectral sensing, and adaptive networks. The following sections outline three frontiers currently under investigation to guide future research toward intelligent, multifunctional "lab-on-fiber" systems.

Combining metasurfaces and graphene with optical fiber technology establishes a transformative platform for next-generation photonic devices. This synergy combines compact structures and nanoscale light manipulation capabilities with the inherent advantages of fiber optics, including low-loss transmission, mechanical flexibility, and seamless compatibility with communication networks. This thesis systematically addresses three fundamental challenges in hybrid fiber-optic system development: (1) overcoming fabrication complexity through a precision-engineered fiber-tip metasurface integration process; (2) resolving spatial mode limitations via large-mode-area PCF; and (3) mitigating modal mismatch through flat-band resonant metasurface design. In Section 3.3, a universal fabrication framework is developed to enable direct metasurface fabrication on fiber tips, significantly enhancing efficiency. This approach facilitates the realization of an ultra-sensitive BIC metasurface fiber-tip sensor and a chiral metalens for high-speed optical switching. Additionally, a proof-of-concept tunable D-shaped fiber polarizer is proposed, addressing the demand for dynamic fiber devices.

Chapter 2 establishes the theoretical foundation by examining metasurface physics, optical fiber modes, and the dynamic tunability mechanisms of graphene. It highlights key applications such as achromatic metalenses, full-Stokes polarization imaging, and BIC sensing, while introducing graphene-based broadband polarization control as a pivotal advancement for dynamic fiber devices. These insights bridge fundamental principles with practical implementations, guiding the design of subsequent experimental platforms.

Chapter 3 demonstrates a plasmonic quasi-BIC metasurface integrated onto SMF demonstrates ultra-sensitive real-time sensing with 1 μL analyte volumes. Angular spectrum analysis reveals that the flat-band characteristics of quasi-BIC modes enable

efficient coupling to fiber fundamental modes, overcoming spectral broadening caused by Gaussian beam divergence. This work pioneers a fiber-based platform for high-Q factor BIC metasurface applications and resolves critical mode-matching challenges through resonant engineering.

Chapter 4 introduces a chiral plasmonic metalens integrated at the fiber tip, achieving 95% circular polarization conversion efficiency. Validated in a 1 Gb/s coherent communication system, this device enables polarization-modulated optical switching with 20 dB extinction ratio and 600 μs response speed. The planar chiral unit design further demonstrates arbitrary polarization focusing capabilities, underscoring the viability of fiber-integrated metasurfaces for high-speed optical signal processing and adaptive polarization control in telecommunications.

Chapter 5 presents a gate-tunable D-shaped fiber polarizer combining graphene with gold grating-induced SPPs. By exploiting phase-matching conditions and graphene's chemically adjustable Fermi level, this device achieves broadband operation across C- and O-bands with high extinction ratios and low insertion loss. This platform exemplifies the synergistic potential of graphene and fiber optics for dynamically reconfigurable photonic systems, advancing the frontier of active integrated photonic devices.

Collectively, this research advances fiber-integrated metasurface technology through novel fabrication methods, mode-coupling strategies, and tunable device architectures. The demonstrated sensors, switches, and polarizers not only address current limitations in photonic systems but also open new avenues for miniaturized, intelligent optical networks in sensing, communication, and quantum technologies.

The following outlook presents three promising research directions currently under investigation, along with potential avenues for future exploration: (1) high-efficiency

fiber-tip dielectric metalenses, (2) advanced nanofabrication techniques for multilayer metasurfaces on optical fiber substrates, and (3) active fiber-integrated metasurfaces devices.

(1). Fiber-tip dielectric metasurface. Following the established fabrication flow for fiber-tip metasurfaces, we extended the methodology to fabricate dielectric metalenses on large-mode-area PCFs. The metalens design utilizes birefringent rectangular meta-atoms functioning as half-wave plates, providing a π phase shift between orthogonal polarization states. As illustrated in Figure 6-1, these meta-atoms exhibit geometrically controlled phase modulation. Through systematic optimization, we selected four meta-atoms demonstrating both high optical transmittance (T > 80%) and phase coverage spanning 0 to π. Significantly, due to their half-wave plate characteristics, an additional π to 2π phase coverage was achieved by rotating the selected meta-atoms by 90 degrees. This combined approach yielded eight distinct meta-atom configurations, whose geometric parameters are shown in Table 6-1.

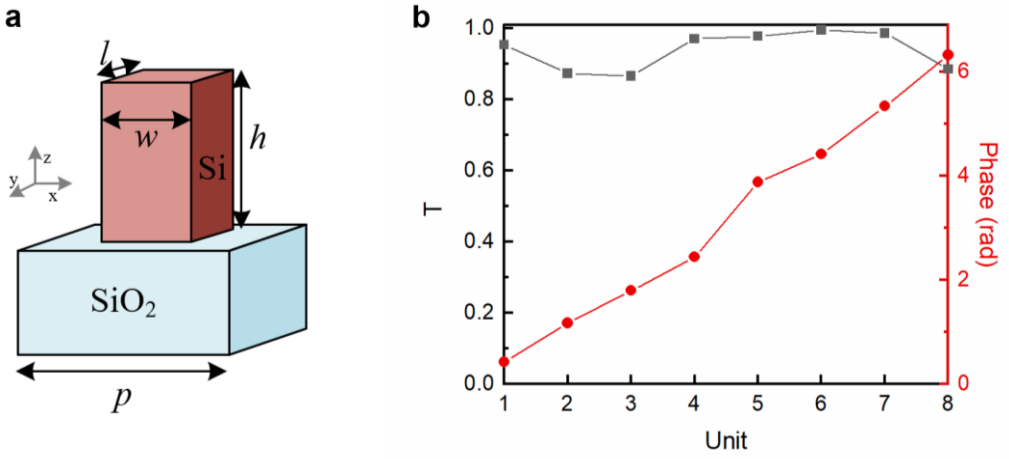

Figure 6-1 (a) Geometry of dielectric meta-atom. **(b)** Transmittance and phase delay of the selected 8 meta-atoms along the XP incidence.

Table 6-1 Geometry details of 4 meta-atoms.

Meta-atom No.	*l* (nm)	*h* (nm)
1	520	150
2	480	200
3	480	240
4	520	260

The meta-atom exhibits a period of 600 nm and a height of 800 nm. Following the fabrication protocol detailed in Section 3.3 and adapted to Figure 6-2(a), an 800-nm-thick α-silicon layer was deposited by Low-pressure chemical vapor deposition (LPCVD). Preliminary fabrication of the designed metalens on LMA-PCF was conducted using consistent FIB parameters: 40 kV acceleration voltage and 40 pA beam current.

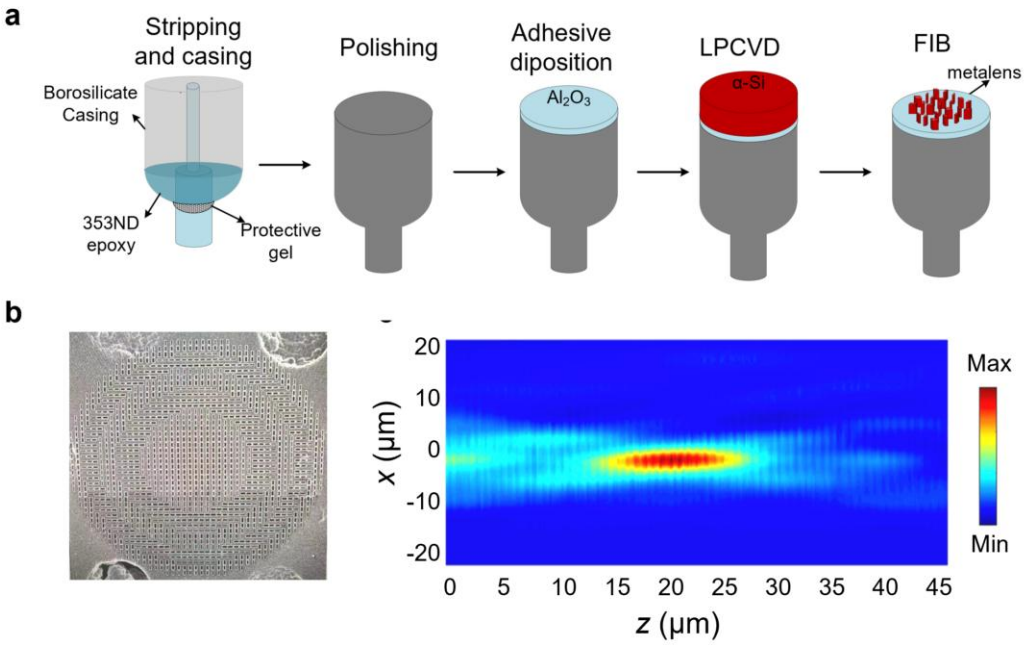

Figure 6-2 (a) Fabrication flow for dielectric metalens on fiber. **(b)** The dielectric metalens on LMA-PCF under SEM view. **(b)** The focusing performance along z direction.

However, challenges emerged during the etching process due to the dielectric material properties and the meta-atoms' elevated height, requiring extended etching duration compared to plasmonic metalens fabrication. Additional complications arose from FIB-induced material sputtering effects, resulting in non-ideal tapered nanostructures characterized by progressive top-width reduction and base-width expansion. Figure 6-2 shows the preliminary preparation results and focusing phenomena along *z* direction. Further optimization of the fabrication methodology will be conducted to address these structural imperfections and enhance manufacturing accuracy for achieving high focusing efficiency.

(2) Other potential fiber-tip metasurface fabrication methods. Since the diameter of SMF core is 8 μm, there needs to be a transmission distance between the end facet of the single-mode fiber and the metasurface to expand the field area. One possible solution is to use a length of high-index SiO2 or a length of large mode area multi-mode fiber to hold the metasurface. The connection between the metasurface and MMF/SiO2 can be made using UV-curable epoxy. The length of the beam expanding part needs to be calculated to hold the metasurface while minimizing efficiency loss.

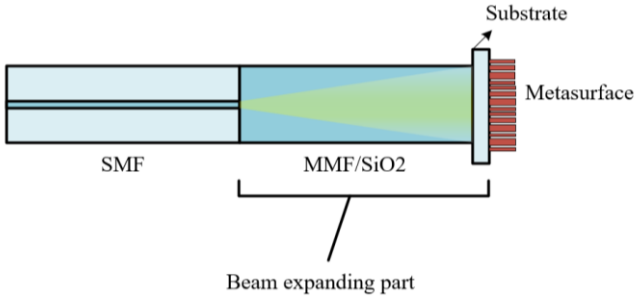

Figure 6-3 Method of fusing a beam expanding part for integrating large area metasurface on fiber tip.

Apart from direct fabricating metasurface on fiber tip, there has another potential fabrication method through wafer-to-fiber [*160*] and PMMA-to-fiber [*161*] by electron-beam lithography (EBL) method. These techniques maintain compatibility with

conventional semiconductor manufacturing protocols while offering enhanced scalability. Integration with our previously demonstrated technique of fusing 800 μm MMF as beam-expanding elements enables large-area metasurface implementation on fiber tips.

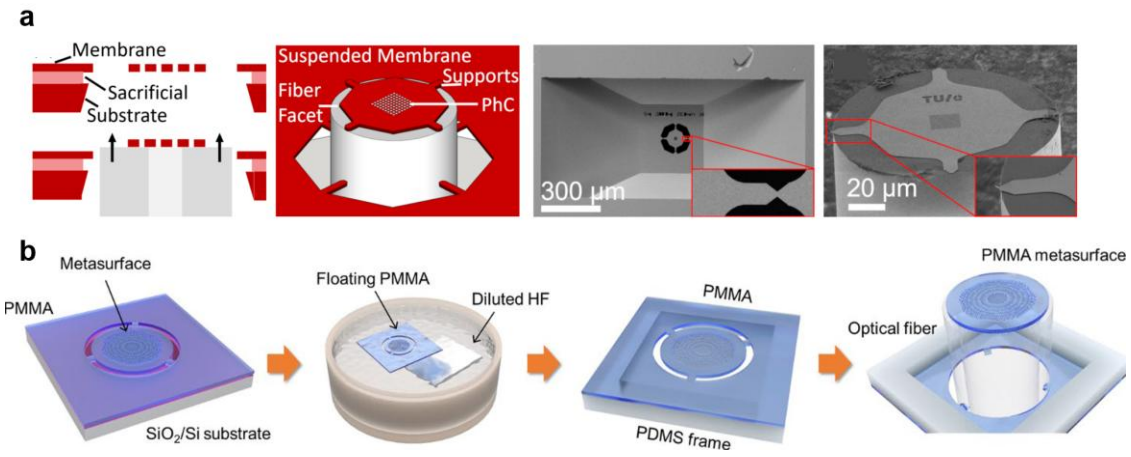

Figure 6-4 Transfer method for fiber-tip metasurface. (a) The wafer-to-fiber transfer method for integrating photonic crystal structures on an SMF.[*160*] (b) The fabrication flow for the method utilizing PMMA as substrate to transfer metasurface on fiber tip.[*161*]

Both transfer methods employ EBL to create high-precision metasurfaces on substrate-supported sacrificial layers. Critical to the transfer process is the creation of peripheral etching rings surrounding the metasurface patterns while retaining 10-μm-wide mechanical tethers. Subsequent immersion in diluted HF solution dissolves the sacrificial layer, followed by UV irradiation-assisted alignment and pressure bonding to achieve precise metasurface transfer onto the fiber tip. This methodology not only facilitates single-layer implementations but also shows potential for multilayer metasurface on optical fibers, thereby enabling multifunctional optical devices through vertical integration of disparate optical functionalities.

(3) Active meta-fiber devices. Chapter 5 demonstrates a tunable fiber polarizer leveraging gate-tunable graphene. The proposed architecture employs gold gratings

deposited on graphene to excite SPP modes that enhance coupling efficiency with fundamental fiber modes. Beyond grating-based approaches, recent years have witnessed significant efforts in developing active optical metasurfaces for advanced light manipulation, including phase-change material metasurfaces modulated by femtosecond laser pulse irradiation and electrically reconfigurable conducting oxide metasurfaces. While these innovations enable multifunctional reconfigurability, critical challenges persist in practical implementation. Most reported active metasurfaces remain proof-of-concept demonstrations at simulation scale. Future advancements are anticipated through integration of emerging materials such as 2D transition metal dichalcogenides, perovskite heterostructures, and lithium niobate thin films into fiber-integrated platforms. This materials-driven approach promises to enable multifunctional photonic devices combining polarization control, wavelength selectivity, and dynamic modulation within compact optical fiber architectures.

The integration of metasurfaces and 2D materials with optical fiber systems presents multiple promising avenues for developing novel active optical devices. This interdisciplinary approach aims to systematically investigate fundamental physical mechanisms, develop novel functionalities, and expand practical applications in fiber-integrated platform. Anticipated advancements in nanofabrication methodologies are expected to facilitate the realization of increasingly sophisticated fiber-integrated devices with enhanced performance characteristics and expanded operational capabilities.

References

[1] R. Elnathan and N. H. Voelcker, "Recent Fundamental and Technological Progress in Micro-nanotechnologies," Adv. Funct. Mater. **32**, 2112100 (2022).

[2] L. Rebecchi, I. Martin, I. M. Albo, P. Ranjan, T. Gatti, F. Scotognella, A. Rubino, and I. Kriegel, "Scalable Production of Metal Oxide Nanoparticles for Optoelectronics Applications," Chem. Eur. J. **31**, e202401711 (2025).

[3] F. Han, S. Y. Gu, A. Klimas, N. Zhao, Y. X. Zhao, and S. C. Chen, "Three-dimensional nanofabrication via ultrafast laser patterning and kinetically regulated material assembly," Science **378**, 1325-1331 (2022).

[4] W. Zhou, Z. Y. Zhang, H. Chen, H. K. Tsang, and Y. Y. Tong, "Ultra-Compact and Efficient Integrated Multichannel Mode Multiplexer in Silicon for Few-Mode Fibers," Laser Photon. Rev. **18**, 2300460 (2024).

[5] S. M. Nokandeh, R. Eivazzadeh-Keihan, M. S. Bani, I. Zare, H. M. Kang, M. T. Yaraki, M. Mahdavi, A. Maleki, and R. S. Varma, "Nanoporous structures-based biosensors for environmental and biomedical diagnostics: Advancements, opportunities, and challenges," Coordin. Chem. Rev. **522**, 216245 (2025).

[6] S. M. Wang, P. C. Wu, V. C. Su, Y. C. Lai, C. H. Chu, J. W. Chen, S. H. Lu, J. Chen, B. B. Xu, C. H. Kuan, T. Li, S. N. Zhu, and D. P. Tsai, "Broadband achromatic optical metasurface devices," Nat. Commun. **8**, 1-4 (2017).

[7] M. L. Brongersma, R. A. Pala, H. Altug, F. Capasso, W. T. Chen, A. Majumdar, and H. A. Atwater, "The second optical metasurface revolution: moving from science to technology," Nat. Rev. Electr. Eng. **2**, 125-143 (2025).

[8] D. Fattal, J. J. Li, Z. Peng, M. Fiorentino, and R. G. Beausoleil, "Flat dielectric grating reflectors with focusing abilities," Nat. Photonics **4**, 466-470 (2010).

[9] S. Colburn, A. Zhan, and A. Majumdar, "Metasurface optics for full-color computational imaging," Sci. Adv. **4**, eaar2114 (2018).

[10] T. J. Cui, M. Q. Qi, X. Wan, J. Zhao, and Q. Cheng, "Coding metamaterials, digital metamaterials and programmable metamaterials," Light Sci. Appl. **3**, e218 (2014).

[11] M. Z. Liu, P. C. Huo, W. Q. Zhu, C. Zhang, S. Zhang, M. W. Song, S. Zhang, Q. W. Zhou, L. Chen, H. J. Lezec, A. Agrawal, Y. Q. Lu, and T. Xu, "Broadband generation of perfect Poincare beams via dielectric spin-multiplexed metasurface," Nat. Commun. **12**, 1-9 (2021).

[12] P. K. Jha, N. Shitrit, J. Kim, X. X. Ren, Y. Wang, and X. Zhang, "Metasurface-Mediated Quantum Entanglement," Acs Photonics **5**, 971-976 (2018).

[13] A. S. Solntsev, G. S. Agarwal, and Y. Y. Kivshar, "Metasurfaces for quantum photonics," Nat. Photonics **15**, 327-336 (2021).

[14] A. Cusano, M. Consales, A. Crescitelli, and A. Ricciardi, *Lab-on-Fiber Technology,* 1st ed. ed., Springer Series in Surface Sciences (Springer International Publishing, Cham), **56**, (2015).

[15] Q. C. Zhao, W. H. Yuan, J. Q. Qu, Z. Cheng, G. D. Peng, and C. Y. Yu, "Optical Fiber-Integrated Metasurfaces: An Emerging Platform for Multiple Optical Applications," Nanomaterials **12**, 793 (2022).

[16] M. Principe, M. Consales, A. Micco, A. Crescitelli, G. Castaldi, E. Esposito, V. La Ferrara, A. Cutolo, V. Galdi, and A. Cusano, "Optical fiber meta-tips," Light Sci. Appl. **6**, e16226 (2017).

[17] A. Xomalis, I. Demirtzioglou, E. Plum, Y. M. Jung, V. Nalla, C. Lacava, K. F. MacDonald, P. Petropoulos, D. J. Richardson, and N. I. Zheludev, "Fibre-optic metadevice for all-optical signal modulation based on coherent absorption," Nat. Commun. **9**, 1-7 (2018).

[18] H. Pahlevaninezhad, M. Khorasaninejad, Y. W. Huang, Z. Shi, L. P. Hariri, D. C. Adams, V. Ding, A. Zhu, C. W. Qiu, F. Capasso, and M. J. Suter, "Nano-optic endoscope for high-resolution optical coherence tomography in vivo," Nat Photonics **12**, 540-547 (2018).

[19] Q. L. Bao, H. Zhang, B. Wang, Z. H. Ni, C. H. Y. X. Lim, Y. Wang, D. Y. Tang, and K. P. Loh, "Broadband graphene polarizer," Nat. Photonics **5**, 411-415 (2011).

[20] Y. F. Xiong and F. Xu, "Multifunctional integration on optical fiber tips: challenges and opportunities," Adv. Photonics **2**, 064001 (2020).

[21] H. Ren, J. Jang, C. Li, A. Aigner, M. Plidschun, J. Kim, J. Rho, M. A. Schmidt, and S. A. Maier, "An achromatic metafiber for focusing and imaging across the entire telecommunication range," Nat. Commun. **13**, 4183 (2022).

[22] C. H. Li, T. Wieduwilt, F. J. Wendisch, A. Márquez, L. D. Menezes, S. A. Maier, M. A. Schmidt, and H. R. Ren, "Metafiber transforming arbitrarily structured light," Nat. Commun. **15**, 7222 (2024).

[23] M. Plidschun, H. R. Ren, J. Kim, R. Förster, S. A. Maier, and M. A. Schmidt, "Ultrahigh numerical aperture meta-fibre for flexible optical trapping," Light Sci. Appl. **10**, 57 (2021).

[24] K. C. K. a. G. A. Hockham, "Dielectric-fibre surface waveguides for optical frequencies," Proceedings of the Institution of Electrical Engineers **113**(1966).

[25] I. H. MALITSON, "Interspecimen Comparison of the Refractive Index of Fused Silica," J. Opt. Soc. Am. B **55**, 1205-1209 (1965).

[26] J. Wilde, C. Schulze, R. Brüning, M. Duparré, and S. Schröter, "Selective higher order fiber mode excitation using a monolithic setup of a phase plate at a fiber facet," Proc. of SPIE **9343**, 93431 (2015).

[27] Y. Liang, H. Zhang, W. Zhu, A. Agrawal, H. Lezec, L. Li, W. Peng, Y. Zou, Y. Lu, and T. Xu, "Subradiant Dipolar Interactions in Plasmonic Nanoring Resonator Array for Integrated Label-Free Biosensing," ACS Sens. **2**, 1796-1804 (2017).

[28] M. D. Alonso-Murias, J. S. Velázquez-González, and D. Monzón-Hernández, "SPR Fiber Tip Sensor for the Simultaneous Measurement of Refractive Index, Temperature, and Level of a Liquid," J. Lightwave Technol. **37**, 4808-4814 (2019).

[29] X. He, H. Yi, J. Long, X. Zhou, J. Yang, and T. Yang, "Plasmonic crystal cavity on single-mode optical fiber end facet for label-free biosensing," Appl. Phys. Lett. **108**, 231105 (2016).

[30] J. Hu, S. Bandyopadhyay, Y. H. Liu, and L. Y. Shao, "A Review on Metasurface: From Principle to Smart Metadevices," Front. Phys. **8**, 586087 (2021).

[31] A. Alex-Amor, A. Palomares-Caballero, and C. Molero, "3-D Metamaterials: Trends on Applied Designs, Computational Methods and Fabrication Techniques," Electronics **11**, 410 (2022).

[32] F. Ding, A. Pors, and S. I. Bozhevolnyi, "Gradient metasurfaces: a review of fundamentals and applications," Rep. Prog. Phys. **81**, 026401 (2018).

[33] N. F. Yu, P. Genevet, M. A. Kats, F. Aieta, J. P. Tetienne, F. Capasso, and Z. Gaburro, "Light Propagation with Phase Discontinuities: Generalized Laws of Reflection and Refraction," Science **334**, 333-337 (2011).

[34] N. Yu and F. Capasso, "Flat optics with designer metasurfaces," Nat Mater **13**, 139-150 (2014).

[35] H. T. Chen, A. J. Taylor, and N. F. Yu, "A review of metasurfaces: physics and applications," Rep. Prog. Phys. **79**, 076401 (2016).

[36] L. L. Huang, S. Zhang, and T. Zentgraf, "Metasurface holography: from fundamentals to applications," Nanophotonics **7**, 1169-1190 (2018).

[37] S. L. Sun, K. Y. Yang, C. M. Wang, T. K. Juan, W. T. Chen, C. Y. Liao, Q. He, S. Y. Xiao, W. T. Kung, G. Y. Guo, L. Zhou, and D. P. Tsai, "High-Efficiency Broadband Anomalous Reflection by Gradient Meta-Surfaces," Nano Lett. **12**, 6223-6229 (2012).

[38] P. Genevet, F. Capasso, F. Aieta, M. Khorasaninejad, and R. Devlin, "Recent advances in planar optics: from plasmonic to dielectric metasurfaces," Optica **4**, 139-152 (2017).

[39] M. Decker, I. Staude, M. Falkner, J. Dominguez, D. N. Neshev, I. Brener, T. Pertsch, and Y. S. Kivshar, "High-Efficiency Dielectric Huygens' Surfaces," Adv. Opt. Mater. **3**, 813-820 (2015).

[40] A. Arbabi, Y. Horie, A. J. Ball, M. Bagheri, and A. Faraon, "Subwavelength-thick lenses with high numerical apertures and large efficiency based on high-contrast transmitarrays," Nat. Commun. **6**, 7069 (2015).

[41] J. Kühne, J. Wang, T. Weber, L. Kühner, S. A. Maier, and A. Tittl, "Fabrication robustness in BIC metasurfaces," Nanophotonics **10**, 4305-4312 (2021).

[42] C. W. Hsu, B. Zhen, J. Lee, S. L. Chua, S. G. Johnson, J. D. Joannopoulos, and M. Soljacic, "Observation of trapped light within the radiation continuum," Nature **499**, 188-191 (2013).

[43] A. S. Kupriianov, Y. Xu, A. Sayanskiy, V. Dmitriev, Y. S. Kivshar, and V. R. Tuz, "Metasurface Engineering through Bound States in the Continuum," Phys. Rev. Appl. **12**, 014024 (2019).

[44] F. H. Stillinger and D. R. Herrick, "Bound states in the continuum," Phys. Rev. A **11**, 446-454 (1975).

[45] S. P. Shipman and S. Venakides, "Resonant transmission near nonrobust periodic slab modes," Phys. Rev. E **71**, 026611 (2005).

[46] D. C. Marinica, A. G. Borisov, and S. V. Shabanov, "Bound states in the continuum in photonics," Phys. Rev. Lett. **100**, 183902 (2008).

[47] K. Koshelev, S. Lepeshov, M. Liu, A. Bogdanov, and Y. Kivshar, "Asymmetric Metasurfaces with High-Q Resonances Governed by Bound States in the Continuum," Phys. Rev. Lett. **121**, 193903 (2018).

[48] Y. H. Wei, L. M. Si, K. L. Han, H. Y. Xu, X. E. Bao, and W. R. Zhu, "Quasi-BIC-enhanced integrated sensing dielectric metasurfaces for molecular fingerprint retrieval and chiral detection," Nanoscale, 8005-8015 (2025).

[49] J. Peng, X. Lin, X. A. Yan, X. Yan, X. F. Hu, H. Y. Yao, L. J. Liang, and G. H. Ma, "Terahertz Biosensor Engineering Based on Quasi-BIC Metasurface with Ultrasensitive Detection," Nanomaterials **14**, 799 (2024).

[50] F. Dell'Olio, "Metasurface-Enabled Microphotonic Biosensors via BIC Modes," Photonics **12**, 48 (2025).

[51] G. W. Hu, X. M. Hong, K. Wang, J. Wu, H. X. Xu, W. C. Zhao, W. W. Liu, S. Zhang, F. Garcia-Vidal, B. Wang, P. X. Lu, and C. W. Qiu, "Coherent steering of nonlinear chiral valley photons with a synthetic Au-WS metasurface," Nat. Photonics **13**, 467-472 (2019).

[52] T. Wang, W. Z. Di, W. E. I. Sha, and R. P. Zaccaria, "Enabling low Threshold Laser Through an Asymmetric Tetramer Metasurface Harnessing Polarization-Independent Quasi-BICs," Adv. Opt. Mater., 2403345 (2025).

[53] Y. H. Ren, P. S. Li, Z. J. Liu, Z. H. Chen, Y. L. Chen, C. Peng, and J. Liu, "Low-threshold nanolasers based on miniaturized bound states in the continuum," Sci. Adv. **8**, eade8817 (2022).

[54] J. H. Yang, Z. T. Huang, D. N. Maksimov, P. S. Pankin, I. V. Timofeev, K. B. Hong, H. Li, J. W. Chen, C. Y. Hsu, Y. Y. Liu, T. C. Lu, T. R. Lin, C. S. Yang, and K. P. Chen, "Low-Threshold Bound State in the Continuum Lasers in Hybrid Lattice Resonance Metasurfaces," Laser Photon. Rev. **15**, 2100118 (2021).

[55] K. Koshelev, A. Bogdanov, and Y. Kivshar, "Meta-optics and bound states in the continuum," Sci. Bull. **64**, 836-842 (2019).

[56] C. W. Hsu, B. Zhen, A. D. Stone, J. D. Joannopoulos, and M. Soljacic, "Bound states in the continuum," Nat. Rev. Mater. **1**, 16048 (2016).

[57] K. Koshelev, S. Lepeshov, M. K. Liu, A. Bogdanov, and Y. Kivshar, "Asymmetric Metasurfaces with High-Q Resonances Governed by Bound States in the Continuum," Phys. Rev. Lett. **121**, 193903 (2018).

[58] M. Luo, Y. Zhou, X. Zhao, Y. Li, Z. Guo, X. Yang, M. Zhang, Y. Wang, and X. Wu, "Label-Free Bound-States-in-the-Continuum Biosensors," Biosensors **12**, 1120 (2022).

[59] A. Arbabi and A. Faraon, "Advances in optical metalenses," Nat. Photonics **17**, 16-25 (2023).

[60] S. M. Wang, P. C. Wu, V. C. Su, Y. C. Lai, M. K. Chen, H. Y. Kuo, B. H. Chen, Y. H. Chen, T. T. Huang, J. H. Wang, R. M. Lin, C. H. Kuan, T. Li, Z. L. Wang, S. N. Zhu, and D. P. Tsai, "A broadband achromatic metalens in the visible," Nat. Nanotechnol. **13**, 227-232 (2018).

[61] E. Arbabi, A. Arbabi, S. M. Kamali, Y. Horie, and A. Faraon, "Multiwavelength polarization-insensitive lenses based on dielectric metasurfaces with meta-molecules," Optica **3**, 628-633 (2016).

[62] A. Arbabi, E. Arbabi, S. M. Kamali, Y. Horie, S. Han, and A. Faraon, "Miniature optical planar camera based on a wide-angle metasurface doublet corrected for monochromatic aberrations," Nat. Commun. **7**, 13682 (2016).

[63] J. Engelberg and U. Levy, "Achromatic flat lens performance limits," Optica **8**, 834-845 (2021).

[64] J. Oh, K. M. Li, J. Yang, W. T. Chen, M. J. Li, P. Dainese, and F. Capasso, "Adjoint-optimized metasurfaces for compact mode-division multiplexing," Acs Photonics **9**, 929-937 (2022).

[65] E. Arbabi, J. Q. Li, R. J. Hutchins, S. M. Kamali, A. Arbabi, Y. Horie, P. Van Dorpe, V. Gradinaru, D. A. Wagenaar, and A. Faraon, "Two-Photon Microscopy with a Double-Wavelength Metasurface Objective Lens," Nano Lett. **18**, 4943-4948 (2018).

[66] H. Kwon, E. Arbabi, S. M. Kamali, M. Faraji-Dana, and A. Faraon, "Single-shot quantitative phase gradient microscopy using a system of multifunctional metasurfaces," Nat. Photonics **14**, 109-114 (2020).

[67] M. Khorasaninejad, W. T. Chen, A. Y. Zhu, J. Oh, R. C. Devlin, D. Rousso, and F. Capasso, "Multispectral Chiral Imaging with a Metalens," Nano Lett. **16**, 4595-4600 (2016).

[68] Y. Z. Ren, S. H. Guo, W. Q. Zhu, P. C. Huo, S. J. Liu, S. Zhang, P. Chen, L. Chen, H. J. Lezec, A. Agrawal, Y. Q. Lu, and T. Xu, "Full-Stokes Polarimetry for Visible Light Enabled by an All-Dielectric Metasurface," Adv. Photon. Res. **3**, 2100373 (2022).

[69] Z. Y. Yang, Z. K. Wang, Y. X. Wang, X. Feng, M. Zhao, Z. J. Wan, L. Q. Zhu, J. Liu, Y. Huang, J. S. Xia, and M. Wegener, "Generalized Hartmann-Shack array of dielectric metalens sub-arrays for polarimetric beam profiling," Nat. Commun. **9**, 4607 (2018).

[70] N. A. Rubin, G. D'Aversa, P. Chevalier, Z. Shi, W. T. Chen, and F. Capasso, "Matrix Fourier optics enables a compact full-Stokes polarization camera," Science **365**, eaax1839 (2019).

[71] G. Soma, Y. Nomoto, T. Umezawa, Y. Yoshida, Y. Nakano, and T. Tanemura, "Compact and scalable polarimetric self-coherent receiver using a dielectric metasurface," Optica **10**(2023).

[72] S. Romano, G. Zito, S. Torino, G. Calafiore, E. Penzo, G. Coppola, S. Cabrini, I. Rendina, and V. Mocella, "Label-free sensing of ultralow-weight molecules with all-dielectric metasurfaces supporting bound states in the continuum," Photonics Res. **6**, 726-733 (2018).

[73] S. Romano, M. Mangini, E. Penzo, S. Cabrini, A. C. De Luca, I. Rendina, V. Mocella, and G. L. G. Zito, "Ultrasensitive Surface Refractive Index Imaging Based on Quasi-Bound States in the Continuum," ACS Nano **14**, 15417-15427 (2020).

[74] N. Li, H. Chen, Y. Zhao, Y. Wang, Z. Su, Y. Liu, and L. Huang, "Ultrasensitive metasurface sensor based on quasi-bound states in the continuum," Nanophotonics **14**, 485-494 (2025).

[75] T. Wang, S. Liu, J. Zhang, L. Xu, M. Yang, D. Ma, S. Jiang, Q. Jiao, and X. Tan, "Dual high-Q Fano resonances metasurfaces excited by asymmetric dielectric rods for refractive index sensing," Nanophotonics **13**, 463-475 (2024).

[76] A. Aigner, A. Tittl, J. Wang, T. Weber, Y. Kivshar, S. A. Maier, and H. Ren, "Plasmonic bound states in the continuum to tailor light-matter coupling," Sci. Adv. **8**, eadd4816 (2022).

[77] W. J. Chen, M. Li, W. H. Zhang, and Y. H. Chen, "Dual-resonance sensing for environmental refractive index based on quasi-BIC states in all-dielectric metasurface," Nanophotonics **12**, 1147-1157 (2023).

[78] H. Y. Li, Z. H. Shi, H. J. Zhang, S. Qiu, and Z. K. Zhou, "Hybrid Metasurface Based on Si_3N_4 Nanopillar for Optical Sensing with Dual Channels," ACS Appl. Nano Mater. **8**, 2965-2973 (2025).

[79] M. Luo, Y. Zhou, X. Y. Zhao, Z. H. Guo, Y. X. Li, Q. Wang, J. J. Liu, W. Luo, Y. Z. Shi, A. Q. Liu, and X. Wu, "High-Sensitivity Optical Sensors Empowered by Quasi-Bound States in the Continuum in a Hybrid Metal-Dielectric Metasurface," ACS Nano **18**, 6477-6486 (2024).

[80] P. Avouris and F. N. Xia, "Graphene applications in electronics and photonics," Mrs Bull **37**, 1225-1234 (2012).

[81] S. L. Yu, X. Q. Wu, Y. P. Wang, X. Guo, and L. M. Tong, "2D Materials for Optical Modulation: Challenges and Opportunities," Adv. Mater. **29**(2017).

[82] X. Du, I. Skachko, F. Duerr, A. Luican, and E. Y. Andrei, "Fractional quantum Hall effect and insulating phase of Dirac electrons in graphene," Nature **462**, 192-195 (2009).

[83] L. M. Malard, K. F. Mak, A. H. C. Neto, N. M. R. Peres, and T. F. Heinz, "Observation of intra- and inter-band transitions in the transient optical response of graphene," New J Phys **15**(2013).

[84] F. H. L. Koppens, D. E. Chang, and F. J. G. de Abajo, "Graphene Plasmonics: A Platform for Strong Light-Matter Interactions," Nano Lett. **11**, 3370-3377 (2011).

[85] N. M. R. Peres, A. H. Castro Neto, and F. Guinea, "Dirac fermion confinement in graphene," Phys. Rev. B **73**(2006).

[86] M. Romagnoli, V. Sorianello, M. Midrio, F. H. L. Koppens, C. Huyghebaert, D. Neumaier, P. Galli, W. Templ, A. D'Errico, and A. C. Ferrari, "Graphene-based integrated photonics for next-generation datacom and telecom," Nat. Rev. Mater. **3**, 392-414 (2018).

[87] X. T. Wang, Y. Cui, T. Li, M. Lei, J. B. Li, and Z. M. Wei, "Recent Advances in the Functional 2D Photonic and Optoelectronic Devices," Adv. Opt. Mater. **7**(2019).

[88] G. W. Hanson, "Dyadic Green's functions and guided surface waves for a surface conductivity model of graphene," J. Appl. Phys. **103**, 064302 (2008).

[89] R. R. Nair, P. Blake, A. N. Grigorenko, K. S. Novoselov, T. J. Booth, T. Stauber, N. M. R. Peres, and A. K. Geim, "Fine structure constant defines visual transparency of graphene," Science **320**, 1308-1308 (2008).

[90] J.-h. C. Cheng Li, Wan-sheng Wang, Tian-xing Wang, Shao-cheng Yan, Dan-ran Li, Fei Xu, Cheng-bo Mou, Yan-qing Lu, "Manipulation of nonlinear optical properties of graphene bonded fiber devices by thermally engineering fermi–dirac distribution," Adv. Optical Mater. **5**, 1700630 (2017).

[91] S. Y. BC Zheng, JH Chen, GX Cui, Fei Xu, Yan-Qing Lu, "Miniature optical fiber current sensor based on a graphene membrane," Laser Photonics Rev. **9**, 517-522 (2015).

[92] J.-h. Chen, Y.-f. Xiong, F. Xu, and Y.-q. Lu, "Silica optical fiber integrated with two-dimensional materials: towards opto-electro-mechanical technology," Light Sci. Appl. **10**, 78 (2021).

[93] E. J. Lee, S. Y. Choi, H. Jeong, N. H. Park, W. Yim, M. H. Kim, J. K. Park, S. Son, S. Bae, S. J. Kim, K. Lee, Y. H. Ahn, K. J. Ahn, B. H. Hong, J. Y. Park, F. Rotermund, and D. I. Yeom, "Active control of all-fibre graphene devices with electrical gating," Nat Commun **6**, 6851 (2015).

[94] H. J. Zhang, N. Healy, L. Shen, C. C. Huang, D. W. Hewak, and A. C. Peacock, "Enhanced all-optical modulation in a graphene-coated fibre with low insertion loss," Sci. Rep. **6**, 23512 (2016).

[95] L. Zhang, Y. Tang, and L. Tong, "Micro-/Nanofiber Optics: Merging Photonics and Material Science on Nanoscale for Advanced Sensing Technology," iScience **23**, 100810 (2020).

[96] J.-h. C. Jun-long Kou, Ye Chen, Fei Xu, and Yan-qing Lu, "Platform for enhanced light-graphene interaction length and miniaturizing fiber stereo devices.," Optica **1**, 307–310 (2014).

[97] B. Z. S Yan, J Chen, F Xu, Y Lu, "Optical electrical current sensor utilizing a graphene-microfiber-integrated coil resonator," **107**, 053502 (2015).

[98] S. S. Chen, F. J. Tian, L. Li, H. K. Qu, Z. L. Su, and J. Z. Zhang, "Double D-shaped hole optical fiber coated with graphene as a polarizer," Appl. Opt. **57**, 7659-7666 (2018).

[99] J. D. Zapata, D. Steinberg, L. A. M. Saito, R. E. P. de Oliveira, A. M. Cardenas, and E. A. T. de Souza, "Efficient graphene saturable absorbers on D-shaped optical fiber for ultrashort pulse generation," Sci. Rep. **6**, 20644 (2016).

[100] H. Pakarzadeh, V. Sharif, D. Vigneswaran, and N. Ayyanar, "Graphene-assisted tunable D-shaped photonic crystal fiber sensor in the visible and IR regions," J. Opt. Soc. Am. B **39**, 1490-1496 (2022).

[101] Y. Li, W. Chen, X. B. He, J. J. Shi, X. M. Cui, J. W. Sun, and H. X. Xu, "Boosting Light-Matter Interactions in Plasmonic Nanogaps," Adv. Mater. **36**, 2405186 (2024).

[102] S. Kasani, K. Curtin, and N. Q. Wu, "A review of 2D and 3D plasmonic nanostructure array patterns: fabrication, light management and sensing applications," Nanophotonics **8**, 2065-2089 (2019).

[103] A. Amirjani, P. Shokrani, S. A. Sharif, H. Moheb, H. Ahmadi, Z. S. Ahmadiani, and M. S. Paroushi, "Plasmon-enhanced nano-photosensitizers: game-changers in photodynamic therapy of cancers," J. Mater. Chem. B **11**, 3537-3566 (2023).

[104] A. I. Kuznetsov, A. E. Miroshnichenko, M. L. Brongersma, Y. S. Kivshar, and B. Luk'yanchuk, "Optically resonant dielectric nanostructures," Science **354**, aag2472 (2016).

[105] S. Kruk and Y. Kivshar, "Functional Meta-Optics and Nanophotonics Govern by Mie Resonances," ACS Photonics **4**, 2638-2649 (2017).

[106] M. Mayer, M. J. Schnepf, T. A. F. König, and A. Fery, "Colloidal Self-Assembly Concepts for Plasmonic Metasurfaces," Adv. Opt. Mater. **7**, 1800564 (2019).

[107] J. X. Liu, H. L. He, D. Xiao, S. T. Yin, W. Ji, S. Z. Jiang, D. Luo, B. Wang, and Y. J. Liu, "Recent Advances of Plasmonic Nanoparticles and their Applications," Materials **11**, 1833 (2018).

[108] A. B. Taylor and P. Zijlstra, "Single-Molecule Plasmon Sensing: Current Status and Future Prospects," ACS Sens. **2**, 1103-1122 (2017).

[109] E. K. Herkert, D. R. B. Alvaro, M. Recchia, W. Langbein, P. Borri, and M. F. Garcia-Parajo, "Hybrid Plasmonic Nanostructures for Enhanced Single-Molecule Detection Sensitivity," ACS Nano **17**, 8453-8464 (2023).

[110] S. Jaitpal, K. W. Ng, A. M. San Juan, C. Martinez, C. Phillips, S. Tripathy, and S. Mabbott, "DNA-directed formation of plasmonic core-satellite nanostructures for quantification of hepatitis C viral RNA," Chem. Sci. **15**, 8112-8126 (2024).

[111] H. S. Su, H. S. Feng, X. Wu, J. J. Sun, and B. Ren, "Recent advances in plasmon-enhanced Raman spectroscopy for catalytic reactions on bifunctional metallic nanostructures," Nanoscale **13**, 13962-13975 (2021).

[112] Q. Wang and L. Wang, "Lab-on-fiber: plasmonic nano-arrays for sensing," Nanoscale **12**, 7485-7499 (2020).

[113] J. J. Wang, L. Y. Wang, J. Y. Feng, C. Q. Tang, X. M. Sun, and H. S. Peng, "Long-term In Vivo Monitoring of Chemicals with Fiber Sensors," Adv. Fiber Mater. **3**, 47-58 (2021).

[114] A. Kodigala, T. Lepetit, Q. Gu, B. Bahari, Y. Fainman, and B. Kanté, "Lasing action from photonic bound states in continuum," Nature **541**, 196-199 (2017).

[115] S. T. Ha, Y. H. Fu, N. K. Emani, Z. Y. Pan, R. M. Bakker, R. Paniagua-Domínguez, and A. I. Kuznetsov, "Directional lasing in resonant semiconductor nanoantenna arrays," Nat. Nanotechnol. **13**, 1042-1047 (2018).

[116] K. Koshelev, S. Kruk, E. Melik-Gaykazyan, J. H. Choi, A. Bogdanov, H. G. Park, and Y. Kivshar, "Subwavelength dielectric resonators for nonlinear nanophotonics," Science **367**, 288-292 (2020).

[117] Y. Liang, D. P. Tsai, and Y. Kivshar, "From Local to Nonlocal High-Q Plasmonic Metasurfaces," Phys. Rev. Lett. **133**, 053801 (2024).

[118] Y. Chen, H. C. Deng, X. B. Sha, W. J. Chen, R. Z. Wang, Y. H. Chen, D. Wu, J. R. Chu, Y. S. Kivshar, S. M. Xiao, and C. W. Qiu, "Observation of intrinsic chiral bound states in the continuum," Nature **613**, 474-478 (2023).

[119] B. Wang, W. Liu, M. Zhao, J. Wang, Y. Zhang, A. Chen, F. Guan, X. Liu, L. Shi, and J. Zi, "Generating optical vortex beams by momentum-space polarization vortices centred at bound states in the continuum," Nat. Photonics **14**, 623-628 (2020).

[120] T. Shi, Z. L. Deng, G. Z. Geng, X. Z. Zeng, Y. X. Zeng, G. W. Hu, A. Overvig, J. J. Li, C. W. Qiu, A. Alu, Y. S. Kivshar, and X. P. Li, "Planar chiral metasurfaces with maximal and tunable chiroptical response driven by bound states in the continuum," Nat. Commun. **13**, 4111 (2022).

[121] D. G. Voelz, *Computational Fourier Optics: A MATLAB Tutorial* (SPIE Press, Bellingham, WA), (2011).

[122] M. V. Rybin, K. L. Koshelev, Z. F. Sadrieva, K. B. Samusev, A. A. Bogdanov, M. F. Limonov, and Y. S. Kivshar, "High-Supercavity Modes in Subwavelength Dielectric Resonators," Phys. Rev. Lett. **119**, 243901 (2017).

[123] S. A. Maier, "Plasmonic field enhancement and SERS in the effective mode volume picture," Opt. Express **14**, 1957-1964 (2006).

[124] P. B. Johnson, Christy, R.W., "Optical constants of the noble metals.," Phys. Rev. B **6**, 4370–4379 (1972).

[125] Z. Wang, Y. Liang, J. Qu, M. K. Chen, M. Cui, Z. Cheng, J. Zhang, J. Yao, S. Chen, D. P. Tsai, and C. Yu, "Plasmonic bound states in the continuum for unpolarized weak spatially coherent light," Photonics Res. **11**, 260-268 (2023).

[126] M. Consales, G. Quero, S. Spaziani, M. Principe, A. Micco, V. Galdi, A. Cutolo, and A. Cusano, "Metasurface-Enhanced Lab-on-Fiber Biosensors," Laser Photon. Rev. **14**, 2000180 (2020).

[127] F. Wang, X. Li, S. Wang, Y. Cao, L. Zhang, Y. Zhao, X. Dong, M. Zheng, H. Liu, W. Lu, X. Lu, and C. Huang, "3D fiber-probe surface plasmon resonance microsensor towards small volume sensing," Sens. Actuators B Chem. **384**, 133647 (2023).

[128] H. Nguyen, F. Sidiroglou, S. F. Collins, T. J. Davis, A. Roberts, and G. W. Baxter, "A localized surface plasmon resonance-based optical fiber sensor with sub-wavelength apertures," Appl. Phys. Lett. **103**(2013).

[129] D. Neshev and I. Aharonovich, "Optical metasurfaces: new generation building blocks for multi-functional optics," Light Sci. Appl. **7**, 58 (2018).

[130] W. T. Chen, A. D. Y. Zhu, and F. Capasso, "Flat optics with dispersion-engineered metasurfaces," Nat. Rev. Mater. **5**, 604-620 (2020).

[131] N. Y. F. Capasso, "Optical Metasurfaces and Prospect of Their Applications Including Fiber Optics," J. Lightwave Technol. **33**, 2344-2358 (2015).

[132] J. P. Balthasar Mueller, N. A. Rubin, R. C. Devlin, B. Groever, and F. Capasso, "Metasurface Polarization Optics: Independent Phase Control of Arbitrary Orthogonal States of Polarization," Phys Rev Lett **118**, 113901 (2017).

[133] Y. Han and G. Li, "Coherent optical communication using polarization multiple-input-multiple-output," Opt. Express **13**, 7527-7534 (2005).

[134] X. Zhang, Y. Liu, J. Han, Y. Kivshar, and Q. Song, "Chiral emission from resonant metasurfaces," Science **377**, 1215-1218 (2022).

[135] J. L. Chenglong Zheng, Guo-cui Wang, Jitao Li, Silei Wang, Mengyao Li, Hongliang Zhao, Zhen Yue, Yating Zhang, Yan Zhang, Jianquan Yao, "All-dielectric chiral coding metasurface based on spin-decoupling in terahertz band," Nanophotonics **10**, 1347 - 1355 (2021).

[136] C. Chen, S. Gao, W. Song, H. Li, S. N. Zhu, and T. Li, "Metasurfaces with Planar Chiral Meta-Atoms for Spin Light Manipulation," Nano Lett. **21**, 1815-1821 (2021).

[137] Z. L. Bin Tang, E. Palacios, Zizhuo Liu, S. Butun, Koray Aydin, "Chiral-Selective Plasmonic Metasurface Absorbers Operating at Visible Frequencies," IEEE Photon. Technol. Lett. **29**, 295-298 (2017).

[138] M. S. Mahmud, D. Rosenmann, D. A. Czaplewski, J. Gao, and X. Yang, "Plasmon-phonon coupling between mid-infrared chiral metasurfaces and molecular vibrations," Opt. Express **28**, 21192-21201 (2020).

[139] J. W. Haohan Chen, Minglei He, Hao Wang, Xinen Wu, Kezhou Fan, Haiying Liu, Qiang Li, KamSing Wong, and Lijun Wu, " High-efficiency spin-decoupled modulation using chiral C2-symmetric meta-atoms," Phys. Rev. A **109**, 013517 (2024).

[140] P. Davids, B. Block, and K. Cadien, "Surface plasmon polarization filtering in a single mode dielectric waveguide," Opt. Express **13**, 7063-7069 (2005).

[141] C. Prakash, M. Sen, H. Mondal, and K. Goswami, "Design and optimization o a TE-pass polarization filter based on a slotted photonic crystal waveguide," J. Opt. Soc. Am. B **35**, 1791-1798 (2018).

[142] C. Prakash and M. Sen, "Optimization of silicon-photonic crystal (PhC) waveguide for a compact and high extinction ratio TM-pass polarization filter," J. Appl. Phys. **127**, 023101 (2020).

[143] S. A. MAIER, *Plasmonics : Fundamentals and Applications* (Springer), (2007).

[144] D. J. J. Hu and H. P. Ho, "Recent advances in plasmonic photonic crystal fibers: design, fabrication and applications," Adv. Opt. Photon. **9**, 257-314 (2017).

[145] W. O. F. Carvalho and J. R. Mejia-Salazar, "Surface Plasmon Resonances in Sierpinski-Like Photonic Crystal Fibers: Polarization Filters and Sensing Applications," Molecules **25**, 4654 (2020).

[146] Y. Gamal, B. M. Younis, S. F. Hegazy, Y. Badr, M. F. O. Hameed, and S. S. A. Obayya, "Highly efficient modified dual D-shaped PCF polarization filter," Opt. Fiber. Technol. **62**, 102459 (2021).

[147] Y. J. Wang, S. G. Li, J. S. Li, and H. L. Chen, "High-Sensitivity Refractive Index Sensing and Broadband Tunable Polarization Filtering Characteristics of D-Shaped Micro-Structured Fiber With Single-Layer Air-Holes and Gold Film Based on SPR," J. Lightwave Technol. **40**, 863-871 (2022).

[148] J. J. Wu, C. Dou, and L. C. Hu, "The D-shape elliptical stoma photonic crystal fiber based on surface plasmon resonance with both filtering and sensing," Opt. Quant. Electron. **53**, 565 (2021).

[149] Y. Guo, J. S. Li, S. G. Li, S. H. Zhang, and Y. D. Liu, "Broadband single-polarization filter of D-shaped photonic crystal fiber with a micro-opening based on surface plasmon resonance," Appl. Opt. **57**, 8016-8022 (2018).

[150] X. J. Meng, J. S. Li, Y. Guo, H. J. Du, Y. D. Liu, S. G. Li, H. T. Guo, and W. H. Bi, "Analysis of a wavelength-tunable D-shaped photonic crystal fiber filter with broad bandwidth," J. Opt. Soc. Am. B **38**, 1525-1531 (2021).

[151] S. Selvendran, J. Divya, A. S. Raja, A. Sivasubramanian, and S. Itapu, "A Reconfigurable Surface-Plasmon-Based Filter/Sensor Using D-Shaped Photonic Crystal Fiber," Micromachines **13**, 917 (2022).

[152] H. L. Chen, S. G. Li, M. J. Ma, Z. K. Fan, and Y. D. Wu, "Ultrabroad Bandwidth Polarization Filter Based on D-shaped Photonic Crystal Fibers with Gold Film," Plasmonics **10**, 1239-1242 (2015).

[153] B. B. Shuai, L. Xia, Y. T. Zhang, and D. M. Liu, "A multi-core holey fiber based plasmonic sensor with large detection range and high linearity," Opt. Express **20**, 5974-5986 (2012).

[154] J. X. Cui, Z. K. Hong, S. N. Fu, B. Chen, M. Tang, and D. M. Liu, "All-fiber polarization manipulation for high-order LP modes with mode profile maintenance," Opt. Express **25**, 18197-18204 (2017).

[155] N. An, T. Tan, Z. Peng, C. Y. Qin, Z. Y. Yuan, L. Bi, C. R. Liao, Y. P. Wang, Y. J. Rao, G. Soavi, and B. C. Yao, "Electrically Tunable Four-Wave-Mixing in Graphene Heterogeneous Fiber for Individual Gas Molecule Detection," Nano Lett. **20**, 6473-6480 (2020).

[156] S. S. Zhang, W. G. Zhang, P. C. Geng, X. L. Li, and J. Ruan, "Design of single-polarization wavelength splitter based on photonic crystal fiber," Appl. Opt. **50**, 6576-6582 (2011).

[157] P. C. Geng, W. G. Zhang, S. C. Gao, S. S. Zhang, H. Zhang, and J. Ruan, "Orthogonal Single-Polarization Single-Core Photonic Crystal Fiber for Wavelength Splitting," IEEE Photon. Technol. Lett. **24**, 1304-1306 (2012).

[158] C. Liu, L. Y. Wang, F. M. Wang, C. H. Xu, Q. Liu, W. Liu, L. Yang, X. L. Li, T. Sun, and P. K. Chu, "Tunable single-polarization bimetal-coated and liquid-filled photonic crystal fiber filter based on surface plasmon resonance," Appl. Opt. **58**, 6308-6314 (2019).

[159] H. Chen, S. Li, M. Ma, J. Li, Z. Fan, and M. Shi, "Surface Plasmon Induced Polarization Filter Based on Au Wires and Liquid Crystal Infiltrated Photonic Crystal Fibers," Plasmonics **11**, 459-464 (2015).

[160] L. Picelli, A. van Klinken, G. Lindgren, K. D. Hakkel, F. Pagliano, N. Fiaschi, I. Sersic-Vollenbroek, P. J. van Veldhoven, R. W. van der Heijden, and A. Fiore, "Scalable wafer-to-fiber transfer method for lab-on-fiber sensing," Appl. Phys. Lett. **117**, 151101 (2020).

[161] M. Kim, N. R. Park, A. Yu, J. T. Kim, M. Jeon, S. W. Jeon, S. W. Han, and M. K. Kim, "Multilayer all-polymer metasurface stacked on optical fiber via sequential micro-punching process," Nanophotonics **12**, 2359-2369 (2023).